Using Micro-Scale Observations to Understand Large-Scale Geophysical Phenomena: Examples from Seismology and Mineral Physics

by

Jeffrey Lockridge

A Dissertation Presented in Partial Fulfillment
of the Requirements for the Degree
Doctor of Philosophy

Approved November 2015 by the
Graduate Supervisory Committee:

Thomas Sharp, Co-Chair
Ramón Arrowsmith, Co-Chair
Sang-Heon Shim
Edward Garnero
Kurt Leinenweber

ARIZONA STATE UNIVERSITY

December 2015

ABSTRACT

Earthquake faulting and the dynamics of subducting lithosphere are among the frontiers of geophysics. Exploring the nature, cause, and implications of geophysical phenomena requires multidisciplinary investigations focused at a range of spatial scales. Within this dissertation, I present studies of micro-scale processes using observational seismology and experimental mineral physics to provide important constraints on models for a range of large-scale geophysical phenomena within the crust and mantle.

The Great Basin (GB) in the western U.S. is part of the diffuse North American-Pacific plate boundary. The interior of the GB occasionally produces large earthquakes, yet the current distribution of regional seismic networks poorly samples it. The EarthScope USArray Transportable Array provides unprecedented station density and data quality for the central GB. I use this dataset to develop an earthquake catalog for the region that is complete to *M* 1.5. The catalog contains small-magnitude seismicity throughout the interior of the GB. The spatial distribution of earthquakes is consistent with recent regional geodetic studies, confirming that the interior of the GB is actively deforming everywhere and all the time. Additionally, improved event detection thresholds reveal that swarms of temporally-clustered repeating earthquakes occur throughout the GB. The swarms are not associated with active volcanism or other swarm triggering mechanisms, and therefore, may represent a common fault behavior.

Enstatite $(Mg,Fe)SiO_3$ is the second most abundant mineral within subducting lithosphere. Previous studies suggest that metastable enstatite within subducting slabs may persist to the base of the mantle transition zone (MTZ) before transforming to high-pressure polymorphs. The metastable persistence of enstatite has been proposed as a

potential cause for both deep-focus earthquakes and the stagnation of slabs at the base of the MTZ. I show that natural Al- and Fe-bearing enstatite reacts more readily than previous studies and by multiple transformation mechanisms at conditions as low as 1200°C and 18 GPa. Metastable enstatite is thus unlikely to survive to the base of the MTZ. Additionally, coherent growth of akimotoite and other high-pressure phases along polysynthetic twin boundaries provides a mechanism for the inheritance of crystallographic preferred orientation from previously deformed enstatite-bearing rocks within subducting slabs.

ACKNOWLEDGMENTS

I would like to express my deep appreciation and gratitude to my advisors and dissertation co-chairs, Dr. Ramón Arrowsmith and Dr. Thomas Sharp. Each has known me for over 10 years, and invested immeasurable amounts of time and resources in my personal, intellectual, and professional growth. Dr. Arrowsmith has accepted me as his student multiple times when he may not have had the time or resources set aside to do so. I have always appreciated his support for my professional development, and I would not be where I am today without his guidance. Dr. Sharp welcomed a seismology student into the mineral physics group and provided the support and advising to help me achieve my career goals. Over the years I have often doubted myself, but Dr. Sharp's encouragement and confidence in me has never faltered and I have needed that… many times!

I would also like to thank the countless others in SESE that have provided council, encouragement, and support. My sincerest thanks to Dr. Matt Fouch for his role in… everything. I would never have been in graduate school without him accepting me into the program, and I will always be indebted to him for that. Thank you to dissertation committee members Dr. Ed Garnero, Dr. Sang-Heon Dan Shim, and Kurt Leinenweber for helping shape this dissertation into its current form, for contributing to my intellectual growth, and for always being available for career advice or a quick chat. Also, thanks to Mark Stevens for dealing with those Antelope machines and keeping them running just for me. I swear, I'm almost done with them! Thanks to Becky Polley and Becca Dial in the SESE front office for their patience, guidance, and hard work as I have bothered them seemingly non-stop for last six years (and even during undergrad) about many

departmental and college issues. I would still be lost in a sea of paperwork and red tape without their help.

I would like to thank my fellow SESE graduate students who have been my council, support, and friends over the years. Thanks to Patty Lin, Chunpeng Zhao, and Kevin Eagar for always being willing to help out with programming questions and for being great friends and amazing human beings. My seismology projects would have been immensely more difficult without their contributions. Thank you to members of the geophysics group (especially Mingming Li, Divya Allu Peddiniti and John West) for their friendship and for countless conversations over the years that helped me retain my sanity during the transition from H-wing to ISTB4 and back again. I would also like to thank my fellow Sharpies, with whom it has truly been a pleasure to share an office. I enjoyed every minute of our commiserations and celebrations together (thanks again for the chips!). Thanks to Karen Rieck for putting up with my stupid comments, providing welcome distractions, and encouraging us all to find cool rocks. Thanks to Crystyl Fudge for making birthday celebrations mandatory and for encouraging me to be social. I am also grateful for Jinping Hu and his willingness to help out as a human textbook or extra advisor, and for the many hours he so generously spent preparing samples and working with me on the microscopes for these projects.

Finally, I'd be remiss if I didn't acknowledge the innumerable sacrifices made by my family. Without your patience and unconditional love none of this would have been possible. To my beautiful wife, Brittney, thank you for shouldering far more than your fair share of the parenting, breadwinning, and household burdens while I pursued this

final degree. You are truly amazing. Also to my dear daughter, Lily, thank you for lighting up my life with positivity, energy, and joy.

For the seismology component of this dissertation, I would like to thank the EarthScope USArray Transportable Array team for the installation and maintenance seismometer stations that recorded data used in this study, the Incorporated Research Institutions for Seismology (IRIS) Data Management Center for providing waveforms, and the USArray Array Network Facility (ANF) team for providing the initial Antelope database. I would also like to thank Brian Wernicke, Jim Davis, Ryan Porter, Lei Wang, Bill Holt, and Manoochehr Shirzaei for productive discussions at various points during the development of this project. This work was supported by the National Science Foundation via an EarthScope Science CAREER grant to M. J. Fouch (EAR-0548288).

For the mineral physics projects, I gratefully acknowledge the use of facilities with the LeRoy Eyring Center for Solid State Science at Arizona State University. Funding for experiments and analysis associated with these projects was provided by NSF Grant EAR 838159.

TABLE OF CONTENTS

Page

CHAPTER Page

APPENDIX Page

LIST OF TABLES

LIST OF FIGURES

Figure Page

CHAPTER 1

DISSERTATION INTRODUCTION

1.1 Introduction

Earthquake faulting and the dynamics of subducting lithosphere are among the frontiers of geophysics. Exploring the nature, cause, and implications of geophysical phenomena requires multidisciplinary investigations focused at a range of spatial and temporal scales. For example, studies of microscopic-scale mineral and rock physics can provide key constraints for models of continental-scale tectonophysics or global-scale mantle dynamics. Moreover, models describing large-scale geophysical phenomena may represent an oversimplification or inaccurate representation of the dynamic Earth system if they do not account for certain micro-scale geophysical processes. In this dissertation, I use observational seismology and experimental mineral physics to show that an understanding of small-scale geophysical processes (e.g., microseismicity within the crust, or metastable phase transformations within subducting lithosphere) is essential for refining models of larger-scale geophysical phenomena observed within the Earth.

In Chapter 2, I apply observational seismology to explore the nature of faulting and deformation within the Great Basin (GB) in the western United States (US). The USArray Transportable Array (TA) continuously recorded seismic data for two years across most of the continental US. Using TA data, I have developed a small-magnitude ($M < 2.0$) seismicity catalog that is consistent with recent geodetic data for the region, showing that the GB is deforming everywhere and all the time. I also use these data to identify repeating, temporally-related small-magnitude earthquake sequences (swarms) throughout the study region. These results suggest that earthquake swarms may be a

common fault behavior (i.e., Peng and Gomberg 2010) that occurs independent of tectonic environment. By using a range of geophysical data to examine potential causes for these earthquake swarms, I suggest that pore fluid pressure variation due to external geophysical phenomena (i.e., local transient deformation events or subsurface fluid migration) as the most likely cause of earthquake swarms within the study region.

Within Chapters 3 and 4, I apply experimental mineral physics to constrain models for the behavior of subducting lithosphere within the mantle transition zone (MTZ). Enstatite is the second most abundant mineral within subducting oceanic lithosphere; however, previous studies have shown that enstatite is slow to transform to high-pressure phases at lower temperatures such as those expected within the interior of subducting slabs. This has led to the interpretation that metastable enstatite can survive to the base of the MTZ and impact phenomena such as deep focus earthquakes (Hogrefe et al., 1994) and the stagnation of slabs at the base of the MTZ (van Mierlo et al., 2013; Agrusta et al., 2014; King et al., 2015). Using a multi-anvil apparatus, I performed a series of experiments at high pressure and temperature to better understand how single crystals of natural enstatite $(Mg,Fe)SiO_3$ behave at MTZ conditions.

Within Chapter 3, I report that single crystals of natural Al- and Fe-bearing enstatite are much more reactive than powdered end-member $MgSiO_3$, and intracrystalline transformation mechanisms within natural enstatite are likely to accelerate transformation of enstatite to high-pressure phases within the mantle. Thus, metastable enstatite may not survive to the base of the transitions zone, and it is unlikely to be a contributing factor for the both formation of deep-focus earthquakes and the stagnation of slabs at the base of the MTZ.

In Chapter 4, I examine growth of high-pressure phases along polysynthetic twin boundaries within partially transformed natural enstatite crystals. These results have implications for slab rheology, the causes of deep focus earthquakes, and interpretations of seismically observed crystallographic preferred orientation within slabs at the base of the MTZ.

More detailed summaries of the research presented in Chapters 2, 3 and 4 are provided below.

1.2 Earthquake Swarms and Small-Magnitude Seismicity as Constraints for Faulting and Deformation within the Great Basin

An accurate characterization of small-magnitude (< *M* 2.0) seismicity improves our understanding of tectonic processes and helps to constrain mechanisms of faulting within slowly deforming regions. The interior of the GB occasionally produces large earthquakes, yet the current distribution of regional seismic networks poorly samples the region. Within Chapter 2, I use data recorded by the EarthScope USArray Transportable Array and an improved event detection methodology to produce an earthquake catalog for the GB that is complete to *M* 1.5, has earthquakes as small as local magnitude (M_L) -0.1, and contains 2,158 events from January 2006 through April 2009. I utilize multiple techniques to remove anthropogenic seismicity from all catalogs within the study area from 2004 through 2012. The resulting improved earthquake catalog reveals diffuse small-magnitude seismicity across the region, and supports a model of continued Basin and Range deformation within the interior of the GB. I also identify 49 clusters of seismicity including 10 earthquake swarms scattered throughout the region and conclude

that swarms are a faulting behavior common in diffusely extending crust. I explore a range of possible triggering mechanisms and suggest that perturbations in pore fluid pressure from either (1) local transient deformation events or (2) subsurface fluid migration are the most likely mechanisms for the generation of earthquake swarms within the GB.

1.3 Metastable High-Pressure Reactions in Enstatite: Implications for Slab Dynamics and Deep Earthquakes

Pure $MgSiO_3$ enstatite is much slower to react than olivine in kinetic transformation experiments. This has led to the interpretation that metastable enstatite will persist to much greater mantle depths within a cold subducting slab than metastable olivine. Within Chapter 3, I use data from a series of multi-anvil experiments to examine high-pressure reactivity for natural Al- and Fe- bearing enstatite. Natural enstatite transforms to high-pressure polymorphs at lower pressures and temperatures than synthetic end member $MgSiO_3$, and recovered experimental samples contain abundant intracrystalline transformation. These results show that natural Al- and Fe-bearing enstatite is more reactive than previously thought, and polymorphic reactions are strongly favored over eutectioid-type decomposition reactions. Increased reactivity of enstatite in the mantle would decrease the depth to which metastable enstatite can survive within subducting lithosphere. Therefore, the deepest earthquakes must be caused by a mechanism other than transformational faulting of metastable enstatite, and metastable enstatite may not have a major impact on slab buoyancy and stagnation at the base of mantle transition zone.

1.4 Intracrystalline Transformation of High-Clinoenstatite at Mantle Transition Conditions: Implications for Rates, Crystallographic Preferred Orientations and Deep Focus Earthquakes

Within the mantle, orthoenstatite (OEN) with space group *Pbca* transforms to a monoclinic structure of either *C2/c* or *P2$_1$/c* (HCEN or HCEN2, respectively) depending on composition and pressure-temperature conditions. The transformation of orthoenstatite to the clinopyroxene structure produces polysynthetic twinning along $(100)_{cEn}$, which may have significant impact on transformation rates, rheology, and grain size within pyroxene-rich portions of the mantle such as subducting lithosphere. In a series of multi-anvil experiments performed on untwinned single crystals of natural San Carlos enstatite, abundant polysynthetic twins occur within the enstatite core of all samples recovered from high-pressures. These experiments show that $(100)_{cEn}$ twin boundaries serve as nucleation sites for intracrystalline transformation of high-pressure phases. If active within the mantle, these transformation mechanisms will significantly reduce the depth to which metastable enstatite can persist within cold subducting lithosphere. Growth of high-pressure phases along twin planes also produces aligned regions of reduced grain sizes parallel along $(100)_{cEn}$ that, when coupled with weakness from existing twin planes, may provide a shear instabilities sufficient to support deep focus earthquakes. Additionally, a sample transformed at 21 GPa and 1400°C contains topotaxial growth of akimotoite, wadsleyite, and stishovite along $(100)_{cEn}$, suggesting that transformation along the twin planes may provide a means for the inheritance of crystallographic preferred orientation from previously deformed enstatite-bearing rocks.

CHAPTER 2

EARTHQUAKE SWARMS AND SMALL-MAGNITUDE SEISMICITY AS CONSTRAINTS FOR FAULTING AND DEFORMATION WITHIN THE GREAT BASIN

2.1 Introduction

2.1.1 Earthquake Swarms

Clusters of earthquakes that are spatially and temporally related are an important product of earthquake catalogs. Earthquake clusters are typically classified as being either a mainshock-aftershock (MS/AS) sequences or earthquake swarms. MS/AS sequences are clusters in which the largest event is at the beginning and is followed by aftershocks whose magnitudes and occurrence rates are described by Omori's aftershock law (Utsu et al., 1995). These failure mechanisms are ubiquitous, as MS/AS sequences are common in all tectonic settings. Earthquake swarms are defined as localized bursts of small-magnitude earthquakes that last for a period of days to months and do not contain a larger mainshock (Vidale and Shearer, 2006). Earthquake swarms have been identified in a range of tectonic settings, including subduction zones (Holtkamp and Brudzinski, 2011), transform faults (Lohman and McGuire 2009), ocean ridges (McGuire et al., 2005), regions of ongoing or recent volcanic activity (Segall 2010; Shelly et al., 2013), and geothermal fields (Fischer et al., 2014). Within intraplate regions, swarms are commonly associated with volcanism or geothermal activity (Špičák 2000); however, improved seismic observation capabilities within many slowly deforming regions have led to the detection of intraplate swarms within Arizona (Lockridge et al., 2012), South America

(Holdtkamp et al., 2011), and Canada (Ma and Eaton 2009) that do not appear to be associated with volcanic or geothermal activity.

Earthquake swarms can be triggered by a range of transient geophysical processes within the crust, including fault creep (Lohman and McGuire 2007; Holtkamp and Brudzinski, 2011; Vidale and Shearer, 2006), magma injection (Hill 1977; Smith et al., 2004), and migration of subsurface fluids (Yamashita et al., 2009; Shelly et al., 2013; Fischer et al., 2014). External forces acting upon a fault surface near failure can also trigger swarm activity. For example, dynamic triggering from teleseismic surface waves (Boese et al., 2014), above-average rainfall (Hainzl et al., 2006), and seasonal snow loading (Braunmiller et al., 2014) have been suggested as sources of increased stress. Anthropogenic triggering of earthquake swarms has been summarized *Ellsworth* (2013) and is associated with reservoir impoundment (Simpson et al., 1986), geothermal power generation (Brodsky and Lajoie 2013), and oil and gas production (Frohlich et al., 2011; Rubinstein and Babaie Mahani 2015; Eaton and Rubinstein 2015).

The physical mechanism causing earthquakes during a swarm sequence has been attributed to either (1) transient aseismic slip along a fault that loads neighboring regions of the fault that are more strongly coupled (Segall et al., 2006; Ozawa et al., 2007; Lohman and McGuire 2007; Llenos et al., 2009; Lengliné et al., 2012), or (2) variations in pore pressure along the fault surface or in the containing volume due to migration or injection of fluids (Parotidis et al., 2003; Kurz et al., 2004). These mechanisms may be part of a continuum of fault behavior, which has been documented in both subduction zones (Peng and Gomberg 2010; Lay et al., 2012) and fluid injection experiments (Guglielmi et al., 2015). Tectonic triggering of seismic swarms from aseismic creep has

only been identified at plate boundaries. This may be because plate boundaries contain dense seismic and geodetic monitoring networks that allow for the contemporaneous detection of both small-magnitude earthquakes and transient aseismic slip. Therefore, an improved ability to detect small-magnitude earthquakes and aseismic events is important for the determination of mechanisms responsible for intraplate earthquake swarms that do not appear to be associated with volcanic or anthropogenic activity.

2.1.2 Seismotectonic Setting of the Great Basin

The northern Basin and Range province (hereafter, the Great Basin or GB) is an approximately 800 km wide region of active extension on the edge of the diffuse Pacific-North American plate boundary. Approximately 25% of transtensional deformation associated with the plate boundary is accommodated within the GB (Wernicke et al., 2008); including as much as 5% of the total deformation occurring along the eastern edge of the GB at the Wasatch Fault Zone (Kreemer et al., 2010). Recent crustal extension has been focused at the western and eastern edges of the GB, leading previous studies to conclude that the interior of the GB behaves as a rigid microplate (Bennett et al., 2003; Hammond and Thatcher, 2004; Kreemer et al., 2010; Porter et al., 2014). However, observations of transient deformation events across the study region (Davis et al., 2006; Wernicke and Davis 2010; Chamoli et al., 2014), active deformation across the central GB (Hammond et al., 2014), and the 2008 M_W 5.9 Wells, Nevada earthquake indicate that the interior of the GB continues to deform at low but measureable rates.

Seismicity within the GB is concentrated within two N-S bands (Figure 2.1). The Intermountain Seismic Belt (ISB) follows the Wasatch Fault Zone along the eastern

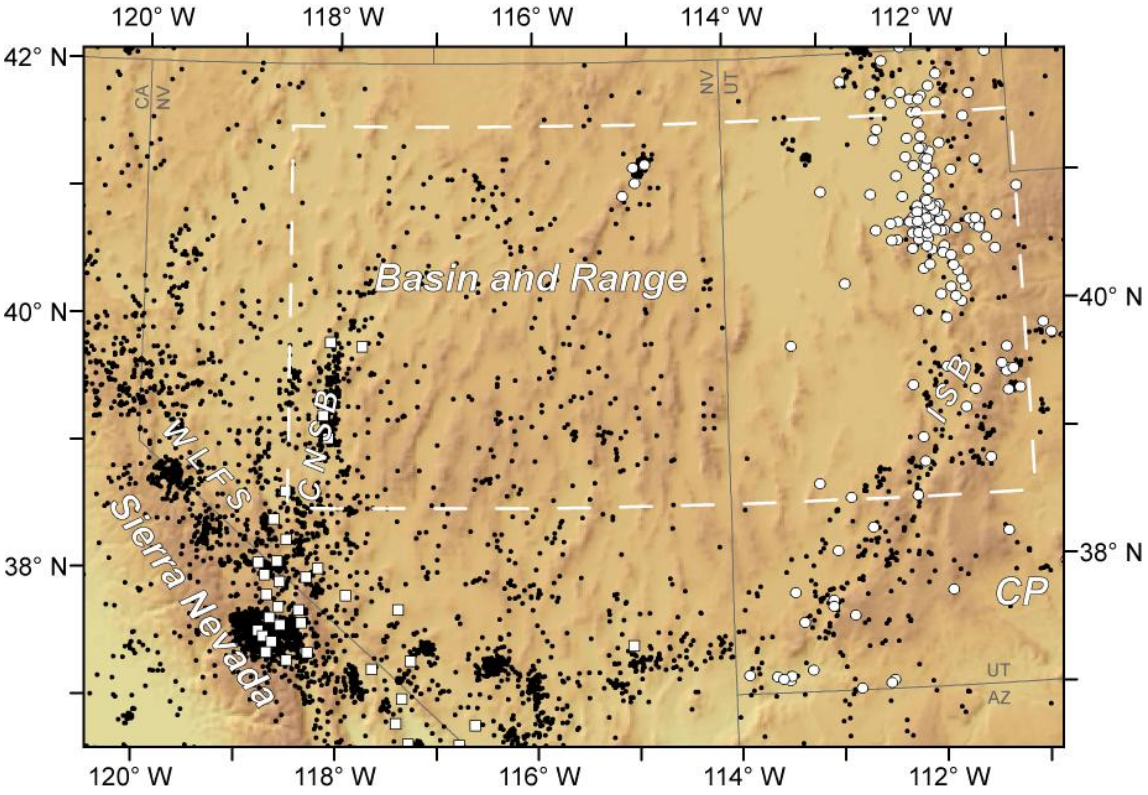

Figure 2.1. Historical seismicity and seismometers within the GB. Black dots are historical earthquakes from the ANSS catalog with $M > 3.0$ (1931-2013). White shapes are seismometers associated with the Nevada Seismic Network (squares), and Utah Seismograph Network (circles). Regional tectonic features include the Intermountain Seismic Belt (ISB), Central Nevada Seismic Belt (CNSB); Walker Lane Fault System (WLFS); and Colorado Plateau (CP). Dashed white box highlights the study area for this project.

margin of the GB. While no large historical earthquakes have been recorded within the ISB, large Holocene earthquakes have been identified in the region (e.g., Friedrich et al., 2003). The Central Nevada Seismic Belt (CNSB) includes several earthquakes M 6.5 or larger within the last 100 years, and may represent the latest in a series of longitudinal seismicity belts that migrate across the GB at ~100-year timescales (Bell et al., 2004). However, small-magnitude seismicity ($M < 2.0$) has not been studied within the interior of the region, and locations and focal mechanisms for most earthquakes ($M < 4.0$) within the GB are typically imprecise because the majority of the region is 100s of km from the

nearest seismometers (Figure 2.1). Earthquakes within the GB are recorded by stations associated with the Utah Seismograph Network (UU) along the eastern margin and stations in the Nevada Seismic Network (NN) along the southwest margin of the region. Each network independently identifies, locates, and determines magnitudes for these events and reports to the Advanced National Seismic System (ANSS) catalog, the authoritative catalog for historical earthquake data in the GB.

The EarthScope USArray Transportable Array (TA) is a network of high-quality broadband seismographs that were temporarily deployed within the GB from January 2006 to April 2009 (Astiz et al., 2014). Seismic data recorded by the TA provides the first opportunity to comprehensively characterize small-magnitude seismicity within the interior of the GB. The USArray Array Network Facility (ANF) performs real-time earthquake detection and location using data from TA stations across the US. Given the large and diverse areas covered by the TA, it is not feasible for the ANF to focus on the detection of small-magnitude earthquakes ($< M_L$ 2.0) and eliminate man-made seismic sources (mines, quarries, ordnance testing, etc.) from their event catalog (Astiz et al., 2014). Therefore, additional processing of TA data is necessary to detect the smallest events possible given the ~70 km spacing of TA stations (e.g., Lockridge et al., 2012; Holland 2012) and to remove any human-generated seismicity.

In this study, we use USArray TA data and apply improved earthquake detection methods to generate a small-magnitude seismicity catalog for the GB from January 2006 to April 2009. This high-quality dataset provides the first opportunity to examine spatial and temporal distributions of small-magnitude seismicity within the central GB which historically has not been well-sampled by seismometers. We use the improved earthquake

catalog to identify a diffuse distribution of seismicity throughout the central GB, which is additional evidence that the entire region continues to experience extension associated with the Pacific-North America plate boundary. We also identify and characterize 49 small-magnitude earthquake swarms and clusters which are scattered throughout the GB and do not appear to be associated with volcanic, geothermal, or anthropogenic sources, implying that they are a commonly occurring seismicity behavior. We examine potential causes of two areas of temporally associated earthquake clusters within the study region and explore potential triggering mechanisms that could produce contemporaneous increases in seismicity rates along multiple parallel range-bounding faults.

2.2 Data and Methods

The USArray ANF provided waveform and seismometer station data for this study that was formatted for analysis using the Antelope Environmental Data Collection Software suite (http://www.brtt.com). Historical earthquake data for this study was collected from the ANSS Composite Earthquake Catalog at http://www.ncedc.org/cnss/catalog-search.html (last accessed April 2013). Preliminary event data recorded by the EarthScope USArray Transportable Array (http://earthscope.org/usarray) were obtained from the EarthScope ANF website http://anf.ucsd.edu/tools/events/download.php (last accessed August 2012). Volcanic ages are from NAVDAT database (North American Volcanic Database, http://www.navdat.org/). Quaternary fault data were obtained from the USGS Quaternary Fault and Fold Database for the United States at http://earthquake.usgs.gov/hazards/qfaults (last accessed April 2013).

To generate an improved earthquake catalog for the GB, we used continuous, three-component data from 160 EarthScope USArray Transportable Array broadband seismometer stations that occupied the region from January 2006 through April 2009 (Figure 2.2). We processed waveform data using the Antelope Environmental Data Collection Software suite (hereafter referred to as *Antelope*) and applied methods described in *Lockridge et al.* (2012) to detect seismicity near the minimum level achievable given the approximate 70 km spacing of TA stations across the region. We merged our small-magnitude seismicity catalog with existing ANF and ANSS catalogs to generate a single comprehensive catalog for the study region from 2004 to 2013.

2.2.1 Development of Raw Event Catalog

We selected a study region bound by coordinates 111°W to 118.5°W and 38.5°N to 41.5°N to (1) include portions of the GB in which geodetic stations were concurrently recording surface displacements while USArray TA stations were installed, and (2) focus on regions within the interior GB that have historically been poorly sampled by seismometers (Figure 2.1). To generate a catalog of small-magnitude events, we used *Antelope's* algorithms for automatic body wave arrival detection (*dbdetect*), detection association (*dbgrassoc*), and hypocenter location (*dbgenloc*) (Pavlis et al., 2004; see Lockridge et al., 2012). The functions *dbdetect* and *dbgrassoc* utilize the same methodology as the real-time *orbdetect* and *orbassoc* functions that are used to generate the ANF earthquake catalog (Astiz et al., 2014).

Ddetect computes short-term average (STA) and long-term average (LTA) amplitudes for specified stations or channels over a series of time steps, and flags

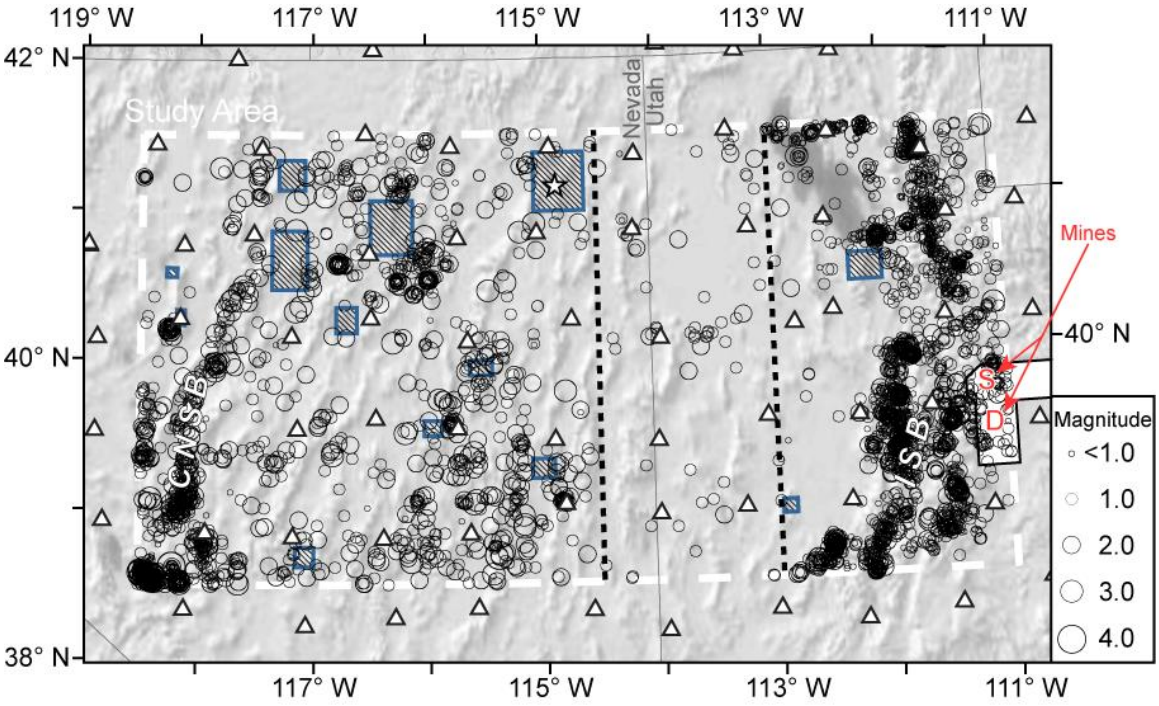

Figure 2.2. Seismicity within the central GB from 2004 to 2013 from the catalog produced in this study. Note the increased density of earthquakes (black circles, sized by magnitude) within eastern and northern Nevada compared to the historical catalog (Figure 2.1) White triangles are TA stations. Blue regions with black hatching areas are the 13 regions of events removed during pre-processing, including the region of the 2008 *M*5.9 Wells, Nevada earthquake sequence (white star). Locations of Skyline Mine (S) and Deer Creek/Crandall Canyon coal mines (D) within the Wasatch Plateau-Book Cliffs coal mining region (white polygon; Arabasz et al., 2005) are shown in the eastern portion of study area. Vertical black dashed lined mark a seismicity gap within the study region between -113°E and -114.5°E.

potential *P*- or *S*-wave arrivals as instances in which the STA/LTA ratio exceeds a threshold amount. *Dbgrassoc* then searches for associated detections that meet a required criteria, such as a minimum number of stations, maximum time interval between first and last arrival, and maximum station distance from the associated event origin, etc. Once the association criteria are met for a given set of arrivals, *dbgenloc* uses an iterative least squares inversion to search over a predefined spatial grid for origin times and hypocenter locations that best match the observed *P*- and *S*-wave arrivals at each station. Detections

that fail to meet the association criteria or are associated with hypocenters located outside of the study region are ignored by the *dbgrassoc* algorithm. Hypocenter locations and origin times for automatically detected events are computed assuming the 2-D *IASP91* velocity model (Kennett and Engdahl, 1991). *Dbgenloc* computes hypocentral errors by assigning weights to each arrival based on residual time and a default or manually provided uncertainty value.

When using an automatic event detection algorithm to generate an earthquake catalog, increasing sensitivity to detect smaller earthquakes also increases the number of false associations included in catalog. These false events are easily recognized while reviewing waveform data because the highest amplitude signal was not typically found on the stations nearest to the event origin. Spurious events greatly increase data processing time and may contaminate earthquake catalogs. Therefore, we altered *dbdetect* and *dbgrassoc* parameter values according to methods described in *Lockridge et al.,* (2012) to detect the smallest possible earthquakes while minimizing unwanted detections. Key *Antelope* parameters used in this study are shown in Table 2.1.

To test the effectiveness of our automatic detection parameters, we developed a series of test catalogs using varying *dbdetect* and *dbgrassoc* parameters. These catalogs were compared to the ANF earthquake catalog of events associated with a M_W 5.9 earthquake that occurred on February 21, 2008 near Wells, Nevada. The ANF catalog identifies 106 total events located within our study region from 00:00:00 to 23:59:59 UTC February 21, 2008, all of which are associated with the Wells, Nevada earthquake and aftershock sequence. By comparison, our final and most effective test run produces an earthquake catalog of 209 unique events for the same sample time and area. Of these

Table 2.1. *Antelope* Parameters Used for Automatic Detection of Earthquakes

Parameter File	
ttgrid	
Nodes/Degree East	25
Nodes/Degree West	25
Depth interval	5 km
dbdetect	
S:N Threshold	3.5
STA Time Window	1.0 sec
LTA Time Window	10.0 sec
dbgrassoc	
Association Window	20 sec
Time Step	10 sec
Minimum Stations	4
Max Station Distance	1.5°

*Additional information on *Antelope* parameter files can be found at www.brtt.com or within *Lockridge et al.* (2012).

209 unique events, 195 are earthquakes and aftershocks associated with the Wells, Nevada event, seven are mine/quarry blasts, six are false detections, and one is an earthquake occurring within the western portion of the study area that the ANF catalog did not previously identify. Our automatic detection algorithm is unable to detect 10 of the 106 earthquakes in the ANF catalog. Our review of waveform data for these events reveals that seven of the 10 were not detected because they were associated with multiple event clusters that had been manually located by ANF technicians. In these cases, event clustering either (1) precluded P-wave detection by elevating the LTA values from neighboring events, or (2) placed the omitted event within the same association time window as another event. The three remaining events identified by ANF but missed by our automatic detection algorithm have *P*-wave arrivals that were flagged by *dbdetect*, but not associated by *dbgrassoc*. Two of these events were detected within in previous tests using different association processing time windows, which suggests that the events

were excluded because their arrivals were split between two separate time-step windows. Based on these results, we conclude that our modified event detection and association parameters are successfully calibrated to detect more events and smaller magnitude seismicity than the parameters used to generate the ANF catalog.

We combine our raw, automatically generated event catalog with the ANF earthquake catalog by merging *Antelope* databases for the two catalogs. This step has two important benefits. First, it allows us to compare our raw event list against the ANF catalog while processing and confirm that our automatic detection algorithm is correctly detecting events across the entire study region for the duration of the study period. Second, it decreases catalog processing time by allowing us to avoid reprocessing events already reviewed by ANF technicians. Therefore, our event catalog primarily contains small-magnitude events that are below the detection threshold of ANF algorithms.

2.2.2 Preliminary Identification and Removal of Non-Tectonic Events

Non-tectonic events are an unavoidable and typically undesirable component of automatically generated seismicity catalogs. There are numerous active mine and quarry sites within the GB (Bon and Wakefield, 2008; Davis and Hess, 2009). To reduce catalog processing time, we use the earthquake catalog generated by ANF and Google Earth satellite imagery to identify mines that performed frequent seismically detectable blasting within the GB during the study period. We find 12 regions where surficial scarring from mining activity was spatially correlated with dense clusters of seismicity recorded by the TA. Additionally, a strong increase in events in their catalog during February 2008 shows that the February 21, 2008 M_W 5.9 earthquake near Wells, Nevada and its aftershocks are

well documented in the ANF catalog (see Astiz et al., 2014). Therefore, we consider the detection and location of the aftershock sequence associated with this event to be beyond the scope of this study.

To avoid detecting and processing seismic events within these areas, we select approximate latitude and longitude bounds for the 13 regions of unwanted seismicity (Figure 2.2; Table 2.2) and eliminate all events within these areas from our automatically generated catalog. This step results in a 65% decrease (24% from the M_W 5.9 Wells earthquake sequence, 41% from the 12 identified mine areas) in the number of automatically detected events within our raw catalog. While we expect that some tectonic events are lost by the addition of this step, the large reduction in time spent manually reviewing waveforms is considered to be a worthwhile tradeoff.

Potential mining, quarrying and ordnance testing blasts not associated as one of the 13 excluded regions may also be detected using waveform character. These events are characterized by emergent *P*-wave arrivals for all stations, an absence of clear S-wave arrivals, codas exceeding 25 seconds on stations within 1° of event hypocenter, and/or a large amount of low-frequency signal (Stump et al., 2002; Lockridge et al., 2012). If an event matches these criteria, we review Google Earth satellite imagery and remove any events with clear evidence of small mining operations, quarries, or ordnance testing activities in the vicinity of the epicenter (Table 2.3). Events with waveforms similar to other non-tectonic events but not located near any known mines, weapons testing ranges, or visibly scarred areas are retained as part of our catalog. Additional steps to further identify and remove human-generated seismic events from our catalog are described in the Results section.

Table 2.2. 13 Areas with events removed from raw catalog during pre-processing

Minimum Latitude (N)	Maximum Latitude (N)	Minimum Longitude (E)	Maximum Longitude (E)	# Events Removed	Designation*
38.62	38.75	-117.16	-117.00	215	Round Mountain Mine
38.92	39.01	-112.97	-112.85	60	Cricket Mountain Quarry
39.20	39.33	-115.11	-114.92	605	Robinson Mine
39.49	39.59	-116.04	-115.89	71	Ruby Hill Mine
39.89	39.99	-115.64	-115.45	80	Bald Mountain Mine
40.18	40.35	-116.80	-116.62	630	Cortez Pipeline Mine
40.23	40.33	-118.19	-118.12	44	Coeur Rochester Mine
40.45	40.63	-112.32	-112.03	3891	Bingham Mine
40.47	40.86	-117.36	-117.05	964	Phoenix/Trenton Canyon/ Marigold/Lone Tree Mines
40.55	40.61	-118.28	-118.19	40	Florida Canyon Mine
40.70	41.06	-116.50	-116.13	2204	Storm/Miekle/Carlin Mines
40.98	41.37	-115.06	-114.62	5450	M5.9 Wells, NV Sequence
41.13	41.33	-117.30	-117.07	523	Turquoise Ridge/Twin Creeks

*Designations listed according to *Bon and Wakefield* (2008) for Utah operations and *Davis and Hess* (2009) for Nevada.

Table 2.3. Localities of ignored seismicity related to observable mine/quarry activity

Latitude (N)	Longitude (E)	Designation*
38.70	-117.09	Elburz Pit
38.75	-117.97	Unknown
39.56	-112.19	Leamington Cement
40.01	-111.81	Keigley Quarry
40.46	-111.92	Unknown
40.51	-112.48	Roudabush #1
40.63	-112.28	Unknown
40.73	-111.77	Parleys Canyon Rock Quarry
40.81	-111.91	Beck Street 2
40.82	-117.21	Cinder Cone Pit
40.82	-114.25	Pilot Peak Quarry
40.90	-117.75	MIN-AD Mine
41.06	-111.54	Devils Slide Quarry
41.34	-112.03	Unknown
41.41	-115.99	CEMEX Paiute Pit
41.54	-114.95	Big Ledge Mine

*Designations listed according to *Bon and Wakefield* (2008) for Utah operations and *Davis and Hess* (2009) for Nevada.

2.2.3 Earthquake Hypocenter Relocation, Errors, and Magnitudes

After the removal of false detections and anthropogenic seismicity as described above, we process the remaining events in our catalog. Event catalogs generated using *Antelope*'s automatic detection algorithm contain approximate *P*-wave arrival times with a default uncertainty value set for each arrival. Therefore, it is necessary to manually review waveform data for each event, adjust *P*-wave arrivals on vertical components, add S-wave arrivals on horizontal components, and adjust arrival uncertainties before relocating each event. For each earthquake, we review waveform data using a 1 Hz high-pass filter and modify phase arrivals and uncertainties prior to hypocenter recalculation. We deviate from methods used by *Lockridge et al.* (2012) and use *Antelope's dblocsat2* (*LocSAT*) location program (Bratt and Bache, 1988; Bratt and Nagy, 1991) and the *IASP91* global 1-D velocity model (Kennett and Engdahl, 1991) for event relocation instead of a local, empirically determined 1-D velocity model. The ANF uses the *LocSAT* location program and the *IASP91* velocity model to locate earthquakes because they are more generally applicable to the wide range of recorded seismicity and crustal structures encountered by the TA as it moves across the United States (Astiz et al., 2014). We use *LocSAT* and *IASP91* to locate events in an effort to maintain consistency with the ANF catalog, for which our catalog of events is a supplement. Additionally, we consider the *IASP91* velocity model to be adequate for hypocenter locations because the 35 km Moho depth in the model (Kennett and Engdahl, 1991) is consistent with the Moho depths (30-35 km) determined from receiver function analyses (Gilbert and Sheehan, 2004; Lowry and Pérez-Gussinyé 2011; Gilbert 2012) and seismic imaging studies in the GB (Holbrook, 1990; Catchings and Mooney, 1991; Holbrook et al., 1991).

A number of different sources can contribute to errors in hypocentral locations of earthquakes. We consider station clock errors to be insignificant for our dataset because TA stations use timing data from attached GPS receivers, which limit clock errors to a few milliseconds or less. Phase picking errors are subjective and are assigned by the technician for each arrival based on the signal-to-noise ratio and amplitude of each phase arrival. Average phase picking errors for events located in this study are 0.22 s for *P* arrivals and 0.31 s for *S* arrivals. *Antelope* specifies maximum epicentral error by computing the major horizontal components of the confidence ellipse, and depth error is given as the maximum absolute value of the four principal axes of the confidence ellipse projected in the z direction. Our small-magnitude event catalog has a median epicentral error of 3.6 km and a median depth error of 5.9 km.

Relatively large hypocentral errors in this study may be attributed to (1) 3-D variations in crustal structure within the GB that are not well represented by the 1-D *IASP91* velocity model, or (2) conservative arrival time uncertainty picks during our relocation process for small-magnitude events. However, it is most likely that large hypocenter error values are systematic magnitude-dependent mislocation errors (Billings et al., 1994), which are a direct byproduct of our goal to capture the smallest seismic events possible while ignoring larger events in existing catalogs. The accuracy of hypocenter locations is greatly improved by the use of additional station or phase arrivals. The small-magnitude catalog generated as part of this study used an average of 10 arrivals to locate each event. By comparison, data obtained from the ANF's archived monthly databases (http://anf.ucsd.edu/tools/events/download.php) shows that the ANF catalog for the study region was generated using an average of 28 arrivals per event.

After relocating event hypocenters, we use *Antelope*'s *mlrichter* function to calculate Richter local magnitude (M_L) (Kanamori 1983). As the standard magnitude calculation method used for all events in the ANF catalog (Astiz et al., 2014), *mlrichter* finds the station with the largest three-component peak amplitude and applies an empirical scaling factor to assign magnitude based on assumed attenuation at the station's distance from the event epicenter (Richter 1958). Approximately 3% of events in our catalog return a null value for magnitude using this method. These events have few *P* and *S* arrival picks and low signal-to-noise ratios and are thus assumed to be among the smallest events within our catalog ($M < 0.0$).

To create a comprehensive catalog for the study region, we join the final reprocessed event catalog generated as part of this study with the ANF and ANSS earthquake catalogs. Many events were listed within multiple event catalogs. Therefore, we eliminate duplicate events based on a set criteria. First, ANSS origins are given authority over origins from the TA-based catalogs in cases where the ANSS event has an azimuthal station gap smaller than 180°. For duplicate events where the ANSS origin had an azimuthal gap greater than 180°, authority was determined on a case by case basis by comparing TA station coverage with ANSS network coverage at the time of the event. In total, we remove 387 duplicate ANSS events and 37 duplicate ANF events from the comprehensive catalogs. We also remove 790 duplicate events from the catalog generated as part of this study. These events are mostly within the footprint either the UU or NN seismometer networks and were too small to be detected using ANF methods.

We note that earthquake magnitudes provided to the ANSS by UU and NN networks are Richter local magnitude (M_L), body wave magnitude (m_b), or coda

magnitude (m_c). Therefore, in this study we use a generic magnitude (M) when referring to a range of magnitudes in this study.

We increase temporal coverage of our dataset to include all events in the ANSS catalog from 2004 to 2013 (Figure 2.2; Appendix A). This expanded temporal range was included to (1) facilitate a comparison of the current study with concurrently recorded geodetic data within the region and (2) to increase our ability to identify spatial and temporal trends of earthquake clusters within the study region. It should be noted that the completeness threshold of earthquake catalogs varies depending on the aperture and density of available seismic stations. Therefore, the ability of the expanded catalog to detect and accurately locate small-magnitude seismicity varies depending on the locations of regional seismometers prior to 2006 and again after the TA left the region in April of 2009.

2.2.4 Daytime/Nighttime Analysis of Event Clusters

The use of waveform character and satellite imagery to distinguish earthquakes from non-tectonic events may not effectively remove all human-generated seismicity from a regional earthquake catalog. Variations in seismic source type, locations relative to seismic network, station density, and local seismic structure may make it difficult to discern a mine explosion from an earthquake in some regions. Moreover, underground mining activity may be difficult to detect using satellite imagery. Therefore, we employ a statistical approach to further identify and remove unwanted human-generated seismic events from our earthquake catalog. Using an event density analysis to search for spatial event clusters within the study area, we find 70 clusters within the study region for which

10 or more earthquakes are located within a 4 km radius. Several of these clusters are located within areas of underground coal mining activity identified by *Arabasz et al.* (2005) or within areas where evidence of explosions are not clearly visible in satellite imagery.

Identifying event clusters with excessively high ratios of daytime/nighttime event occurrence has been successfully used to remove human-generated events from seismicity catalogs (e.g., Wiemer and Baer, 2000; Gulia 2010). We examine daytime/nighttime distribution of events for two clusters within the Wasatch Plateau-Book Cliffs coal-mining region (Figure 2.2), where nearly all events are inferred to be mining-related (Arabasz et al., 2005). For the largest cluster in our catalog, a clear bias toward daytime hours is visible in the data (Figure 2.3a) confirming that the majority of events related to operations at Deer Creek/Crandall Canyon mines. However, another cluster displays no temporal trends in event origin times despite being located within the mining region identified in *Arabasz et al.* (2005) in the area of Skyline Mine (Figure 2.3b). Further, in a typical MS/AS sequence that follows Omori's Law, the majority of events will occur within the first few hours after the mainshock. If the mainshock and most aftershocks occur during local daytime hours, a strict removal of clusters with high daytime/nighttime event ratios could possibly remove tectonic earthquake sequences from our catalog (Figure 2.3c). Therefore, in addition to a daytime/nighttime event analysis, we compare the location of each cluster to maps of active mines within Nevada and Utah (Davis and Hess, 2009; Bon and Wakefield, 2008).

Using these methods, we are able to confirm and remove 21 clusters of human-generated events (Table 2.4) from our catalog, thereby reducing the number of total

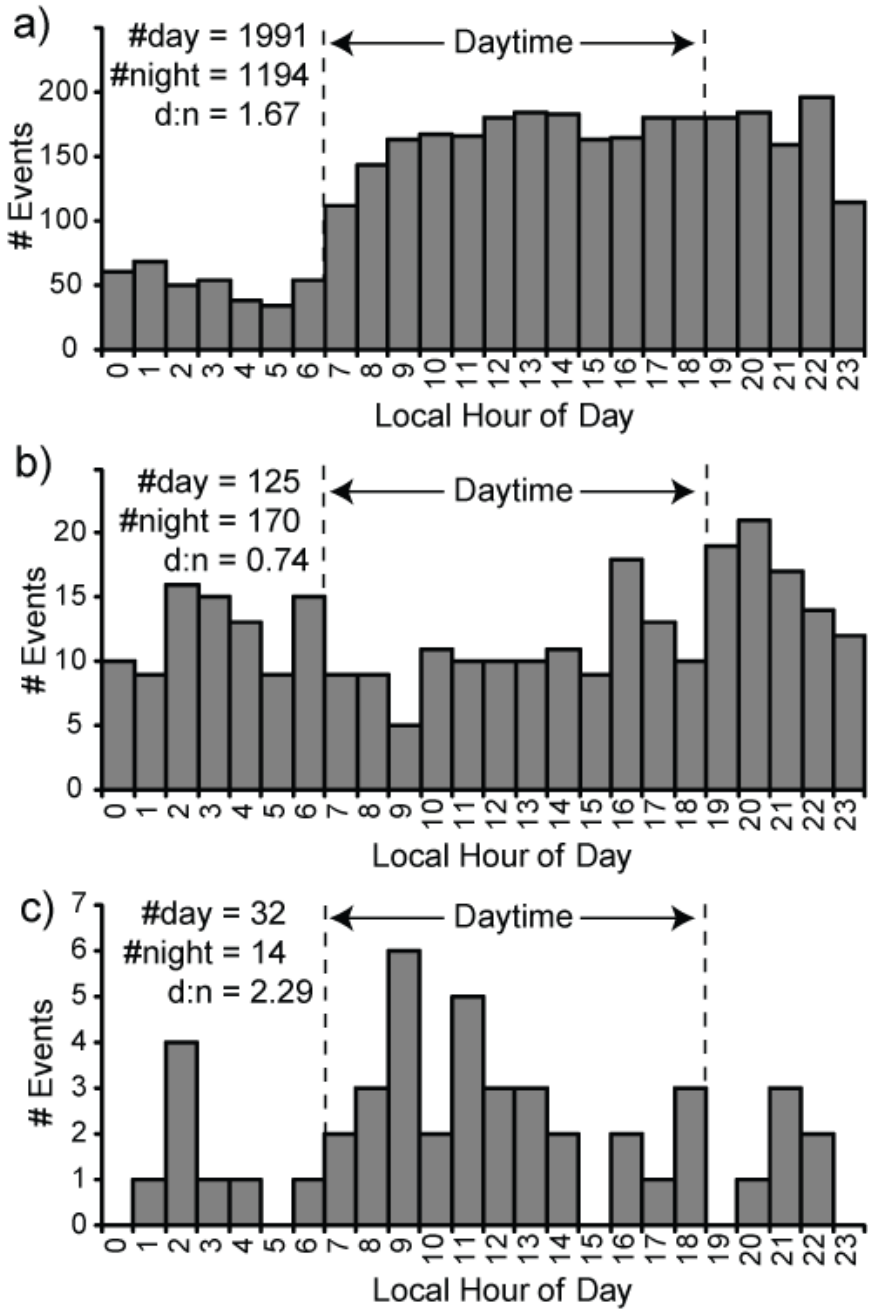

Figure 2.3. Histograms showing daytime/nighttime event distribution for three event clusters. (a) Largest cluster in catalog includes 3189 total events related to underground mining operations Deer Creek/Crandall Canyon coal mines in western Utah (Figure 2). Note the large number of local daytime events relative to events between midnight and 7 AM. (b) Cluster of events with a low daytime-nighttime ratio in the vicinity of underground coal mining operations at Skyline Mine in western Utah (Figure 2). (c) Earthquake cluster centered at 40.64° N and -111.59°E containing a MS/AS sequence with the majority of events occurring during daylight hours.

Table 2.4. Human-generated seismicity confirmed by daytime/nighttime analysis

Latitude (N)	Longitude (E)	Designation*
39.00	-111.37	SUFCO Coal Mine
39.32	-111.17	Deer Creek Coal Mine
39.42	-111.09	Bear Canyon Coal Mine
39.43	-111.21	Crandall Canyon/Deer Creek Mines
39.50	-111.10	Hiawatha Coal Mine
39.56	-112.19	Leamington Cement (limestone) Quarry
39.68	-111.20	Skyline Coal Mine
39.87	-118.39	Craters (Fallon Air Force Range?)
40.26	-111.87	Pelican Point Limestone Mine
40.39	-111.95	Clinton/Allred/Lehi Peck Quarries
40.45	-111.36	Daniels Canyon Pit
40.46	-113.31	Wendover Range/Dugway Proving Grounds
40.46	-111.96	South Farm Quarry
40.51	-118.24	Standard Mine
40.63	-111.35	Unknown Quarry Site
40.70	-111.41	Brown's Canyon Quarry
40.73	-111.77	Parleys Canyon Rock Quarry
40.83	-111.91	UDOT Beck Street Quarry
41.04	-111.66	Round Valley Rock (Limestone)
41.15	-112.88	Hill Airforce Range
41.34	-112.01	Unknown Quarry Site

*Designations listed according to *Bon and Wakefield* (2008) for Utah operations and D*avis and Hess* (2009) for Nevada.

events within our study area by 55%. We assume that the remaining 49 clusters within our final event catalog represent natural earthquake activity and have thus they are included in our final catalog. These 49 earthquake clusters comprise 62% of the 4614 total earthquakes within our final catalog (Figure 2.4).

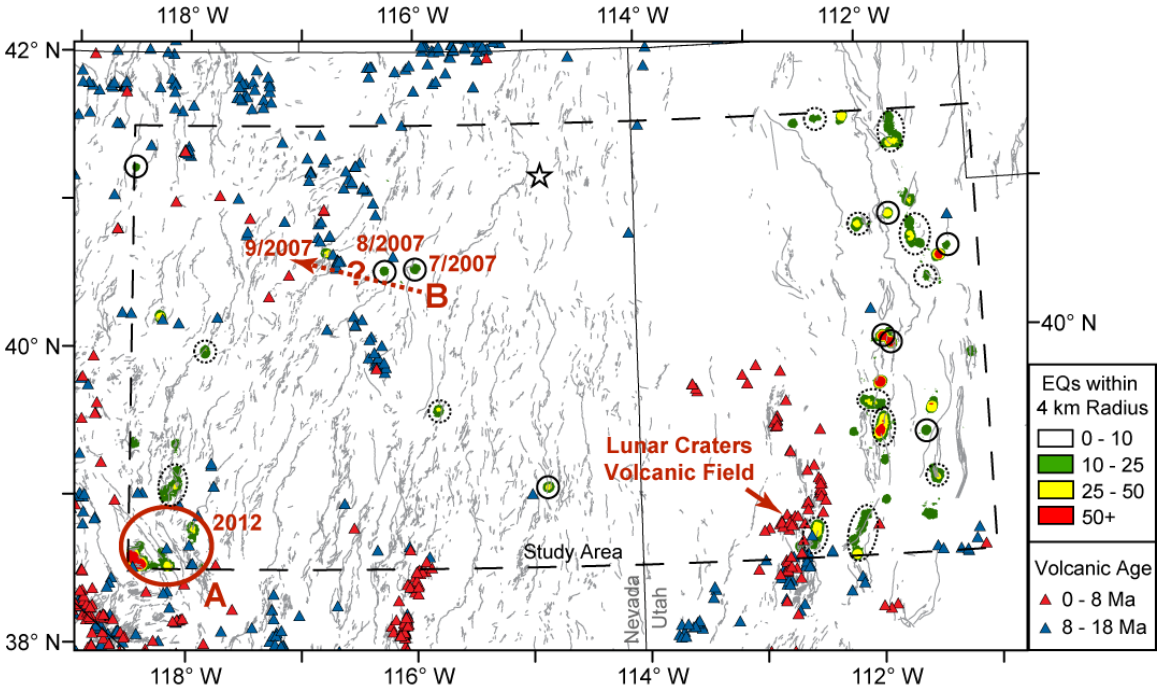

Figure 2.4. Earthquake clusters with 10 or more events within a 4 km radius from 2004 to 2013. Solid circles are earthquake swarms; dashed circles are clusters active during the entire study period; unlabeled clusters are MS/AS sequences. Red solid circle (A) in southwest corner of the study region is an area of increased earthquake and swarm activity in 2012. Red arrow (B) indicates area of temporally related seismicity clusters within the central GB during 2007, with peak periods of activity for each cluster given in month/year format. Quaternary faults (grey lines; see Data and Resources section), areas of recent volcanism (triangles; see Data and Resources section), and 2008 *M*5.9 Wells, Nevada MS/AS sequence (white star) also depicted.

2.3 Results

2.3.1 Statistical Analysis of Earthquake Catalog

The magnitude of completeness (M_c) is the lowest magnitude at which 100% of the earthquakes are apparently detected for a given sample time and region. There are both catalog and network-based methods for determining M_c, which are summarized by *Mignan and Woessner* (2012). Here, we determine M_c by applying the maximum curvature method (Weimer and Wyss, 2000) and a successive check of goodness of fit of

the Gutenberg-Richter relation (Gutenberg and Richter, 1944) to the cumulative frequency-magnitude distribution (FMD) of our earthquake catalog (Figure 2.5a).

$$\log_{10} N = a - bM \quad (1)$$

Here, N is the cumulative number of earthquake having a magnitude larger than M, and a and b are constants. We calculate and b-value for our dataset by applying a least squares fit to the FMD. To reduce the impact of heterogeneities in station spacing and density, we use only events that occurred while TA stations were located within the study region from January 2006 through April 2009. For this subset of our catalog, a M_c of 1.5 and a b-value of 0.90±0.02 represent the best statistical fit for the data with an R^2 value of 0.9987 (Table 2.3; Figure 2.5a). This statistical result is confirmed by a qualitative analysis of the data, as an M_c of 1.5 marks the location of a clear break in the linear trend at the lower end of the cumulative frequency-magnitude plot and is also the peak value of earthquake frequency on the incremental frequency-magnitude curve (Figure 2.5a).

Table 2.5. Earthquake Catalogs in the Great Basin (January 2006 through April 2009).

Entire Study Area					
Catalog	*# Events*	M_C	*b*	*Stations*	*Duplicate Events*
ANSS	1211	1.5†	0.90±0.02†	UU, NN	387
ANF	360			TA	37
ASU	587			TA	790
Central Great Basin (-113°E to -117°E)					
Catalog	*# Events*	M_C	*b*	*Stations*	
ANSS	280	2.1	0.68±0.03	UU, NN	
TA*	671	1.5	0.90±0.04	TA	

*TA catalog includes events from both the ANF catalog and the catalog produced as part of this study(ASU)
†Completeness magnitude (MC) and b-values determined for combined ANSS, ANF, and ASU catalogs.

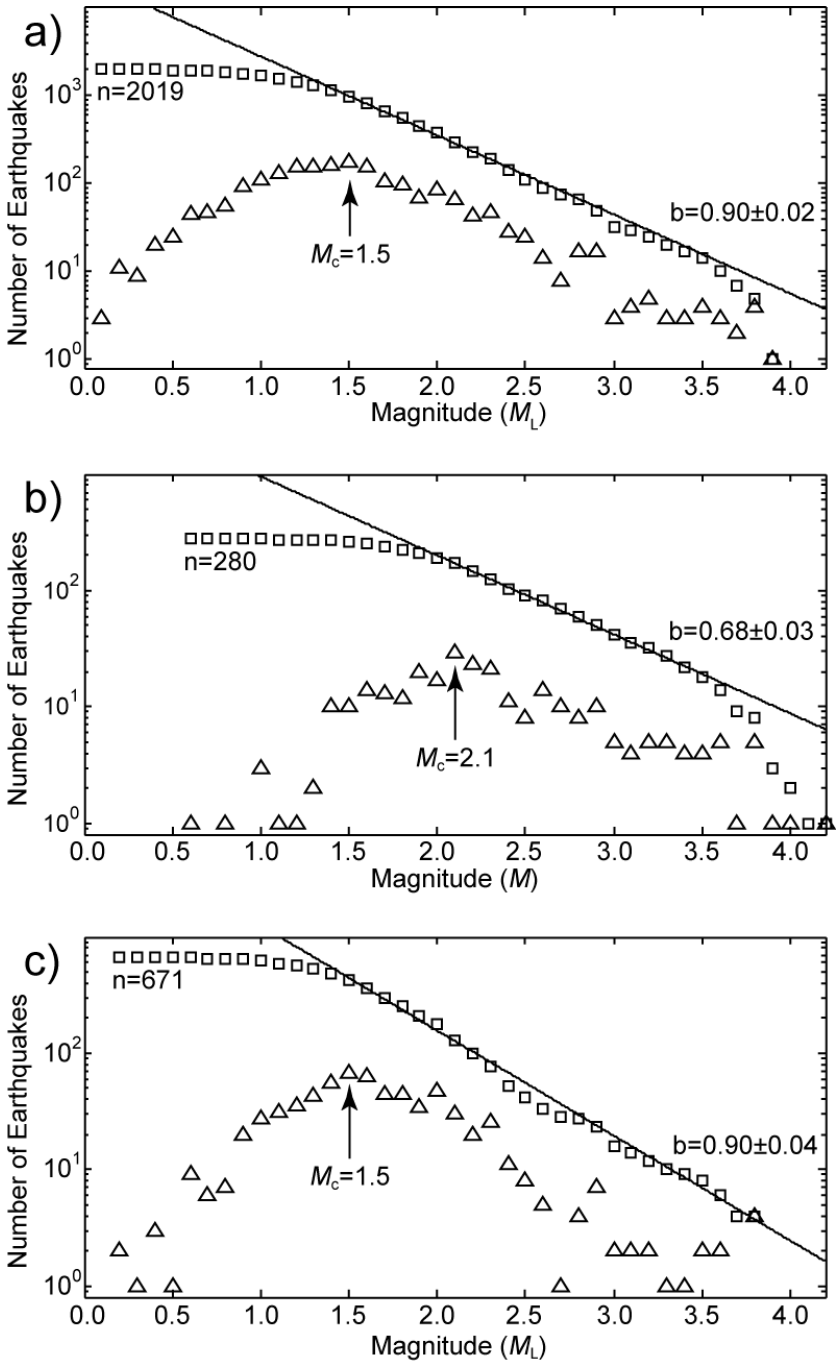

Figure 2.5. Frequency-magnitude distributions (FMD) for three separate subsets of our final seismicity catalog with all events occurring from January 2006 through April 2009. Triangles represent the total number of earthquakes for each magnitude; squares represent the cumulative number of earthquakes for a given magnitude and larger. (a) FMD of events within the ANSS, ANF, and current study catalogs across the entire study region. (b) FMD of events within the ANSS catalog between a longitude range of -113°E to -117°E. (c) FMD of events within the ANF and current study catalogs between a longitude range of -113°E to -117°E.

The M_c and *b*-values for any earthquake catalog change as a function of space and time due to variations in station density and distribution or the use of differing magnitude scales (Wiemer and Wyss, 2000; Zuniga and Wyss 1995). In this study, TA coverage was complete within the study region for only a short time between July 2007 and April 2008 with stations being regularly added and removed to the network over the duration of the deployment. Additionally, the 2006 to 2009 dataset used for FMD analysis above includes events located using the UU and NV stations at the margins of the study area. This results in increased detection capabilities for small events along the eastern and southwestern margins of the study area and decreased detection of small events in the central GB.

To determine whether regional networks along the boundaries of the study region impacted event detection, we create subsets of each earthquake catalog containing only events located outside of the footprints of both the UU and NV--between longitudes -113°E and -117.5°E within the central GB (Figure 2.1). The ANSS catalog of events from 2004 to 2013 for this area is complete to M_c 2.1 with a *b*-value of 0.68±0.06 (Figure 2.5b). For comparison, we create a subset of all combined catalogs from 2006 to 2009 that contained only events between -113°E and -117.5°E. This sub-catalog has a M_c of 1.5 and a *b*-value of 0.90±0.05 (Figure 2.5c).

2.3.2 Depth Distribution of Earthquakes within the Great Basin

The majority of seismicity within our catalog (~95%) occurs within the upper 15 km of the crust, which is consistent with focal depths reported previously by *Doser and Smith* (1989). We search for areas containing multiple events within the middle to lower

portion of the crust by performing an inverse distance weighting interpolation (Watson and Philip, 1985) of hypocentral depths across the study region. For this analysis, we use a variable search radius and sample the eight nearest earthquakes to determine the average depth of seismicity for a given point in the study area. In general, the deepest earthquakes within the catalog occur as isolated events that are likely to have poorly constrained depths due to poor station coverage or small event magnitude. However, we identify five localities in which six to eight events within a 10 km radius have hypocentral depths between 15 and 27 km (Figure 2.6).

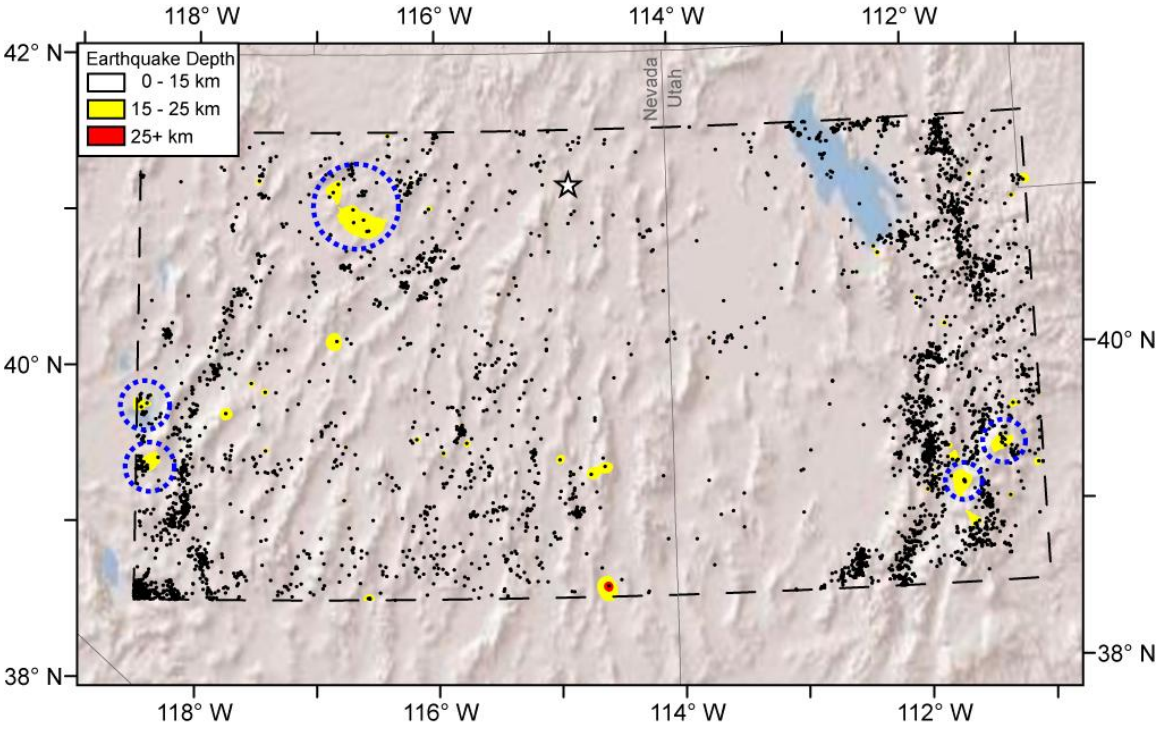

Figure 2.6. Depth distribution of seismicity (black dots) within the study area during the TA deployment from 2004 through 2012. Blue dashed circles highlight five areas in which six to eight events with hypocenters >15 km are observed. Star represents location of 2008 *M*5.9 Wells, Nevada earthquake sequence.

2.3.3 Earthquake Swarms, Mainshock/Aftershock Sequences, and Spatial Clusters

Our event catalog contains 49 earthquake clusters containing 10 or more events within a 4 km radius. These clusters account for 49% of all seismicity within our 2004 to 2013 catalog. We classify these clusters into one of three groups: MS/AS sequences, earthquake swarms, and spatially grouped events with no obvious temporal trends in seismic activity. For each cluster, we determine the period of peak seismic activity and plot event magnitude distribution and cumulative moment release (M_0) versus time since the beginning of cluster activity. To determine moment release, we first converted the M_L values determined during processing to moment magnitude (M_w), and then converted M_w to M_0 using the empirical relationships described by *Hanks and Kanamori* (1979) and *Lay and Wallace* (1995):

$$M_w = [(1.5M_L + 16.0) / 1.5] - 10.73 \quad (2)$$

$$\log M_0 = 1.5M_L + 16.0 \quad (3)$$

For a typical MS/AS sequence, the largest magnitude event occurs first (or near the beginning of the sequence if there are foreshocks) and is followed by aftershocks that decrease in magnitude and frequency with time; therefore, a plot of cumulative magnitude as a function of time will be discontinuous (Figure 2.7a). We define an earthquake swarm as a sequence of seismicity that is temporally focused within a period of weeks to months with no predominant large magnitude earthquake at the beginning of the sequence. Thus, a swarm is characterized by a scattered distribution of event magnitudes as a function of time and a roughly linear trend to the cumulative magnitude plot (Figure 2.7b). The remaining clusters are best classified as spatial clusters that were consistent activity throughout the 2004 to 2013 study period but had no clear temporal

changes in seismicity rate. Using these criteria, we identify 10 swarm-like sequences, 19 clusters of MS/AS activity, and 20 clusters that were continuously active but did not have any obvious temporal grouping of events between 2004 and 2013 (Table 2.6). The three types of clusters classified above are strongly correlated with Quaternary faults and spatially scattered among the seismotectonic regions within the study area and are within the study area (Figure 2.4).

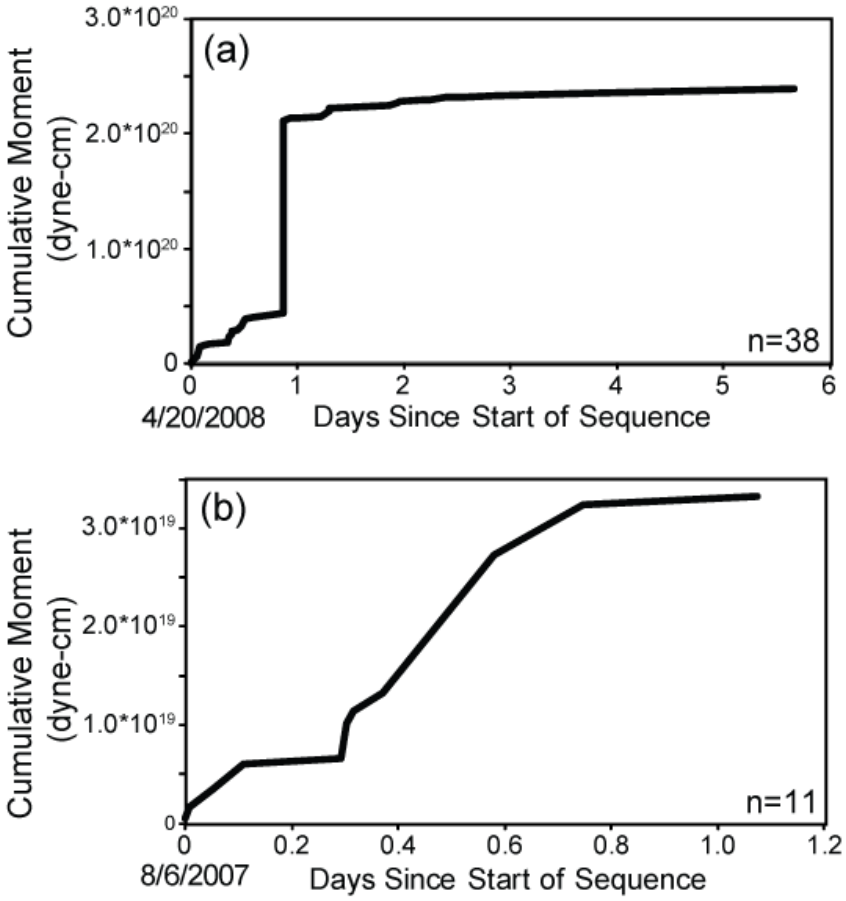

Figure 2.7. (a) Plot of cumulative seismic moment versus time for a MS/AS sequence (*M* 2.8 mainshock) beginning on 20 April 2008 and centered at 39.97°N and -111.89°E in the eastern portion of the study within the Intermountain Seismic Belt. Discontinuous moment-time curve is typical of MS/AS sequences. (b) Plot of cumulative seismic moment versus time for an earthquake swarm beginning on 6 August 2007 and centered at 40.52°N and -116.26°E in the central portion of the Great Basin. Roughly linear moment-time curve is characteristic for earthquake swarms.

Table 2.6. Spatial clusters of 10+ earthquakes within a 4 km radius

Latitude (N)	Longitude (E)	Type	Region	Total Events	Peak Activity	Max Mag
40.56	-111.27	swarm	ISB	11	12/2011-10/2012	0.9
39.32	-111.55	swarm	ISB	17	4/26/2004	2.3
40.80	-111.78	swarm	ISB	29	11/2004	2.2
39.93	-111.82	swarm	ISB	69	6-8/2011	3.3
39.97	-111.89	swarm	ISB	70	4/2008; 8/2008	2.8
39.04	-114.85	swarm	Central GB	34	5/2007-8/2007	2.5
40.53	-115.99	swarm	Central GB	19	7/2007	2.3
40.52	-116.26	swarm	Central GB	19	8/2007	2.1
38.65	-118.40	swarm	CNSB/WLFS	13	1/2012	1.3
41.21	-118.49	swarm	Northwest GB	11	12/2006-1/2007	2.1
39.83	-111.11	MS/AS	ISB	22	11/2010	2.3
40.50	-111.35	MS/AS	ISB	76	All	2.8
39.48	-111.49	MS/AS	ISB	57	11/14-16/2005	3.1
40.58	-111.51	MS/AS	ISB	11	4/2009	2.8
38.75	-111.56	MS/AS	ISB	30	2/2004 & 6/2004	2.6
40.88	-111.57	MS/AS	ISB	40	All	3.0
38.87	-111.93	MS/AS	ISB	13	11/19/2010	3.0
39.66	-111.93	MS/AS	ISB	118	3/2004	3.3
38.78	-112.09	MS/AS	ISB	18	7/2005	3.7
41.47	-112.14	MS/AS	ISB	44	All	2.4
39.34	-112.18	MS/AS	ISB	15	9/01/2005	2.4
38.51	-112.21	MS/AS	ISB	41	5/2007	2.9
41.43	-112.58	MS/AS	ISB	17	1-2/2006	2.2
38.58	-112.70	MS/AS	ISB	17	7-9/2005	3.5
40.64	-116.78	MS/AS	Central GB	30	9/2007	3.6
38.78	-117.95	MS/AS	CNSB/WLFS	46	All; 3-10/2012	3.3
38.52	-118.15	MS/AS	CNSB/WLFS	49	9/2008; 3/2009; 2012	3.3
40.21	-118.25	MS/AS	CNSB/West GB	43	11/2006	3.7
39.35	-118.46	MS/AS	CNSB/WLFS	29	All	2.9
40.34	-111.43	cluster	ISB	20	All	2.1
39.02	-111.47	cluster	ISB	52	All	3.7
40.64	-111.59	cluster	ISB	46	All	2.8
40.73	-111.60	cluster	ISB	25	All	2.2
41.29	-111.69	cluster	ISB	83	All	2.5
41.44	-111.72	cluster	ISB	47	All	2.6
39.15	-111.93	cluster	ISB	14	All	3.3
39.34	-111.95	cluster	ISB	171	All	2.9
39.54	-112.01	cluster	ISB	70	All	2.9
40.73	-112.05	cluster	ISB	41	All	2.9

Table 2.6. (Cont.) Spatial clusters of 10+ earthquakes within a 4 km radius

Latitude (N)	Longitude (E)	Type	Region	Total Events	Peak Activity	Max Mag
38.68	-112.16	cluster	ISB	29	All	2.2
38.62	-112.23	cluster	ISB	15	All	2.9
41.46	-112.39	cluster	ISB	16	All	1.4
38.70	-112.54	cluster	ISB	96	All	3.1
39.57	-115.80	cluster	Central GB	30	7/2006 - 5/2008	2.8
39.98	-117.85	cluster	CNSB	29	All	3.4
39.08	-118.10	cluster	CNSB	98	All	3.6
39.34	-118.10	cluster	CNSB	21	All	2.9
38.62	-118.21	cluster	CNSB/WLFS	14	7/2010	4.2
38.54	-118.39	cluster	CNSB/WLFS	338	All; 7-9/2012	4.3

In addition to the *M*5.9 Wells, Nevada event sequence, MS/AS sequences occur within the eastern portion of the study area along the ISB, in the western and southwest portions of the study area in association with the CNSB and Walker Lane Fault Zone (WLFZ), and within the central GB. The mainshocks for these sequences range from *M* 2.2 to 3.7 and were followed by decays in event magnitude and frequency over time. Of the 110 *M* 3.0 or larger events our final catalog, 30 occurred during the TA deployment from January 2006 to April 2009. Therefore, our ability to identify additional MS/AS sequences and clusters prior to 2006 and after April 2009 is impacted by a M_c of 2.5 for the interior of the GB within the ANSS catalog.

Clusters of consistent seismic activity were focused along the ISB and WLFZ (Table 2.6). These clusters are generally characterized by high event counts and random magnitude distributions throughout the entire study period; although, several include MS/AS sequences or earthquake swarms. For example, five separate earthquake clusters within a 30 km radius in the southwest corner of the study area (area "A", Figure 2.4) were continuously active with occasional events *M* 3.0 or larger over the duration of the

study period. In 2012, each of these clusters produced MS/AS sequences or earthquake swarms with transient increases in seismicity rate. There is no discernible temporal pattern or spatial migration associated with these earthquake swarms aside from the entire region being more seismically active in 2012.

Earthquake swarms occur across the entire study region, four out of 10 swarms are located within the central or northwestern GB, away from the CNSB, WLFZ, and ISB (Appendix B). Swarms do not appear to be associated with regions of recent (< 8 Ma) volcanism (Figure 2.4), and none are located in the vicinity of known oil and natural gas wells, wastewater injection wells, or geothermal power plants (Figure 2.8). Swarms in this study are dominated by small-magnitude earthquakes with the largest event in the sequence ranging from M_L 0.9 to 3.3. Periods of increased seismic activity associated with the swarms ranged from eight hours to 10 months, and the number of events within these sequences ranged from 6 to 66 (Appendix B). In addition to the periods of increased seismicity that defined each swarm, scattered small-magnitude events often occurred before and/or following the swarms. In several cases, an earthquake with a larger magnitude than any event in the swarm sequence occurred following a multiple year gap in seismic inactivity.

An apparent westward migration of earthquake cluster activity occurred within the central portion of the study area between July and September of 2007 (area “B”, Figure 2.4). The sequence begins with the eastern and central earthquake swarms in July and August, respectively, and culminates in a MS/AS sequence initiated by a M_L 3.6 earthquake on 13 September 2007. The eastern swarm is centered at 40.53°N and -115.99°E and consists of 17 earthquakes that occurred during a six day period starting at

01:38:10 UTC on 12 July 2007. The central swarm is located at 40.52°N and -116.26°E (approximately 24 km west of the eastern swarm) and consists of 11 earthquakes that occurred during 26-hour period beginning at 08:39:52 UTC on 6 August 2007. The western MS/AS sequence is centered at 40.64°N and -116.79°E, approximately 45 km WNW of the central swarm and 68 km WNW of the eastern swarm. All three clusters in the sequence are located adjacent to mapped north-south trending Quaternary faults (Figure 2.4) and are surrounded by more isolated background seismicity primarily recorded during the deployment of TA stations in the area.

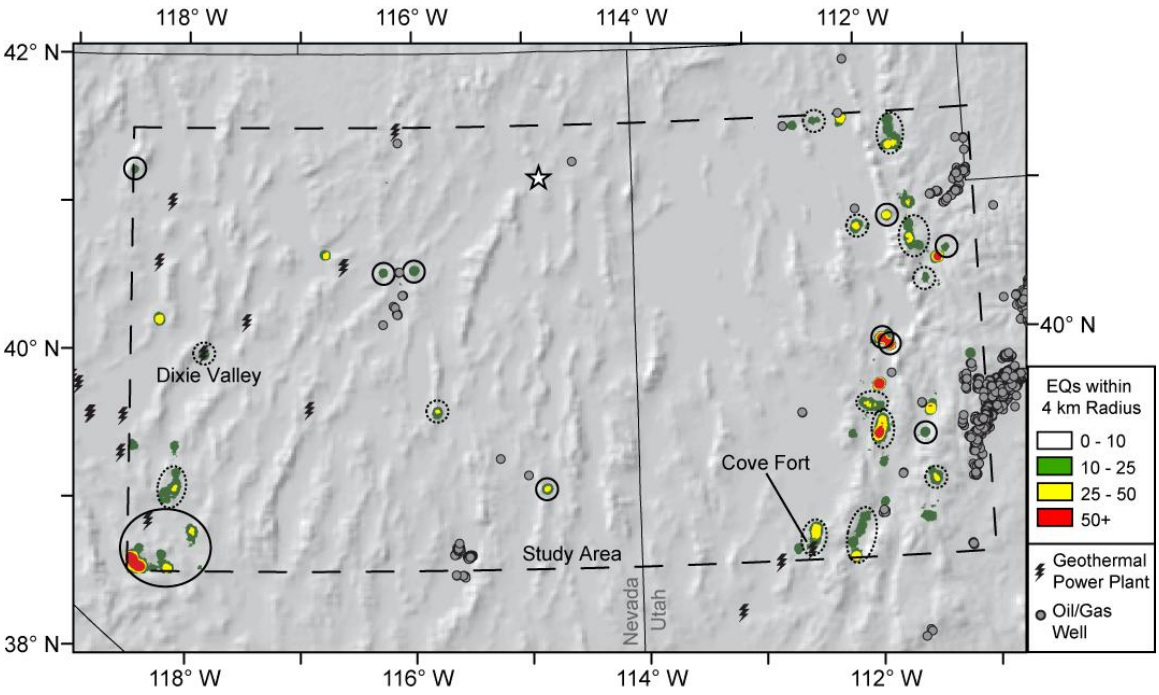

Figure 2.8. Earthquake clusters with 10 or more events within a 4 km radius from 2004 to 2013. Solid black circles are earthquake swarms; dashed black circles are clusters active during the entire study period; unlabeled clusters are MS/AS sequences. Bolt symbols are geothermal power plants from the National Renewable Energy Laboratory (NREL) database (https://maps.nrel.gov/geothermal-prospector/), and grey circles are oil and gas production and injection wells within the study area. Utah well data is from Utah Automated Geographic Reference Center (AGRC; http://gis.utah.gov/) and Nevada well data was provided by the Nevada Bureau of Mines and Geology (NBMG; http://www.nbmg.unr.edu/).

2.4 Discussion

2.4.1 Distribution of Small-Magnitude Seismicity within the Great Basin

The number and density of events in any seismicity catalog is strongly dependent upon the distribution of seismometers used to detect events. Despite having individual station installations that lasted from 18 to 24 months, the TA provides the first opportunity to synoptically and uniformly characterize small-magnitude seismicity within regions of the central GB that have not been previously sampled with this sensitivity. The improved density and spatial coverage of the TA reveals diffuse small-magnitude seismic activity across the entire study region, with areas of lower earthquake density between longitudes -114.5°E and -113°E (Figure 2.2). The distribution of seismicity is consistent with the findings of *Hammond et al.* (2014) who reported active strain accumulation across the entire GB and lower strain rates between -115° and -113° longitude. This geographic correlation suggests that active tectonic strain accumulation and seismic strain release are coupled and may be controlled by larger-scale tectonic features within the region, such as a rigid crustal block along the Nevada-Utah border.

The occurrence of the 2008 *M*5.9 Wells, Nevada earthquake within the northern GB and diffuse seismicity discovered throughout the majority of the GB as part of this study highlight the need for improved seismic monitoring within the central GB. While the deployment of TA stations within the study region improved the detection threshold of small-magnitude events, the two-year occupation of the TA stations in the region is insufficient to fully characterize seismic hazard considering deformation rates of 0.6 mm yr^{-1} across the interior of the GB (Hammond et al., 2014). Additionally, a thorough statistical analysis of the combined ANSS and TA-based catalog used in this study is

hindered by variable station coverage and density with time and differing earthquake location and magnitude determination methods between catalogs. Despite these limitations, we determine that the presence of TA stations within the study region improved detection thresholds from M_c 2.1 using only regional network stations to M_c 1.5. The addition of just three permanent stations within northern and eastern Nevada would greatly improve small-magnitude event detection and location across the interior of the GB and would allow for an improved and more meaningful analysis of seismicity within the region in the future.

2.4.2 Mechanisms for Producing Earthquake Swarms within the Great Basin

Earthquake swarms and clusters within the study area are predominately located away from regions of recent (< 8 Ma) volcanic activity, with the lone exception being a cluster located within the Lunar Craters volcanic field (Figure 2.4). Seismic activity associated with dike intrusions or pore pressure diffusion events is typically swarm-like with notable changes in background seismicity rates (Hill 1977; Špičák 2000; Smith et al., 2004). The Lunar Craters cluster is within the general trend of seismicity associated with the ISB. It is consistently active throughout the study period with no clear temporal bursts of seismicity that could be associated with transient magma injection events. Additionally, the cluster has a similar temporal event distribution as other clusters within the ISB. While a magmatic origin for this cluster cannot be ruled out, it is more likely that this seismicity cluster is similar to others along mapped Quaternary faults within the ISB and occurs as a result of ongoing tectonic deformation within the region (Figure 2.4).

The GB has a number of geothermal fields that are currently being used for geothermal power generation (Figure 2.8). Even non-pressure stimulated geothermal power plants have been shown to induce seismicity within regions of low seismic hazard (Brodsky and Lajoie 2013; Megies and Wassermann 2014). Two earthquake clusters are located adjacent to geothermal power plants within the study region. The Cove Fort geothermal power facility is within the Lunar Craters volcanic field (Figures 2.4 & 2.8). This plant began power production in 2013 and could not have triggered seismic events during the period of study. The Dixie Valley Terra Gen geothermal plant began operation in 1988 and is located within the trend of the CNSB. We review the historical ANSS catalog from 1931 to 2013 and find that the 56 events in the area of this cluster have each occurred since 1991. More detailed seismic monitoring at the Dixie Valley Terra Gen geothermal power plant is necessary to determine whether seismicity in this area is induced by geothermal power production or if it is more general background seismic activity associated with the CNSB.

Small to moderate earthquakes can be caused by the injection of fluids into the subsurface during wastewater injection and production of oil and natural gas (e.g., Ellsworth 2013). We examine well records from the Nevada Bureau of Mines and Geology and the Utah Automated Geographic Reference Center for evidence of potential anthropogenic triggering of earthquakes in relation to injection wells or oil and gas production wells. Only one well in the northeast corner of the study area is located near one of the 49 clusters identified in this study (Figure 2.8). This well was drilled in 2012 and all of the seismicity in this sequence occurred in 2010 or earlier. Therefore, none of

the seismicity clusters in this study were caused by oil and gas production or injection well activity.

Small-magnitude earthquake swarms occurred within portions of central and northwestern GB that are isolated from the more active ISB and CNSB. A similar widespread distribution of swarms and clusters was also observed within southern California (Vidale and Shearer, 2006), Arizona (Lockridge et al., 2012), and South America (Holtkamp et al., 2011). This suggests that earthquake sequences that deviate from Omori's aftershock law are a common faulting behavior regardless of tectonic environment.

Several of the continuously active clusters within this study contain temporal bursts of seismicity related to MS/AS sequences or earthquake swarms. A continuum of fault behavior has been reported within subduction zones, with an upper locked seismogenic zone near the upper portions of the fault and a lower portion of the fault being dominated by aseismic slip and non-volcanic tremor or swarms (Peng and Gomberg 2010; Lay et al., 2012). Swarms in this model consist of repeating earthquakes along an area of the fault surface that is strongly coupled and continually loaded by aseismic creep along neighboring areas of the fault (Nadeau et al., 1995). Within intraplate environments, such fault behavior would represent a gradual change from brittle seismic failure to ductile aseismic slip behavior at mid-crustal depths. Seismicity within the GB is mostly limited to the upper 15 km (Doser and Smith, 1989); therefore, if swarms are associated with a transition from brittle to ductile fault behavior, their hypocentral depths should be focused around 15 km. The small magnitude of events in this study and the 70 km spacing of TA stations resulted in poorly constrained focal

depths in our seismicity catalog; however, focal depths that we do determine for earthquake swarms are scattered throughout the upper crust. A systematic search for non-volcanic tremor or low-frequency earthquakes at TA stations nearest to selected swarms would further constrain whether a continuum of fault behavior occurs within continental interiors. While this type of analysis is beyond the scope of this study, the absence of a clear focal depth dependency for earthquake swarms and clusters within this study suggests that swarms are not limited to a zone of transition from brittle to ductile deformation within the crust.

Another mechanism for the cause of earthquake swarms and clustering is a variation in pore fluid pressure related to active geophysical process within the crust (Kurz et al., 2004). These changes in pore fluid pressure can be caused by dynamic stress triggering (Boese et al., 2014), diffusion of rainfall into fault systems (Hainzl et al., 2006), and increased loading from seasonal snow pack (Braunmiller et al., 2014). We manually reviewed waveforms for each event located as part of this study. While some scattered events may have been triggered by surface waves from teleseismic events, none of the earthquake clusters in this study appear to have been dynamically triggered. Additionally, diffusion from unusually large rain events would result in focused swarm activity in the upper few km of the crust (Hainzl et al., 2006), and swarms within in the study region have focal depths scattered throughout the entire upper crust. Finally, the peak periods of activity for swarm-like earthquake clusters are scattered throughout the calendar year and the Great Basin as a whole generally receives very little snowfall. Therefore, none of these mechanisms of pore pressure variation appear to be responsible for earthquake swarms and clusters within this study.

2.4.3 Constraining Models of Active Deformation within the Great Basin

Geodetic studies have reported transient deformation events within the GB (Wernicke and Davis, 2010; Chamoli et al., 2014). One model to explain these events is aseismic creep along a series of low-angle normal faults at the base of the seismogenic zone within the mid- to upper-crust (Chamoli et al., 2014). This model is consistent with the Basin and Range block faulting model in which listric range-bounding normal faults root into a mid-crustal detachment fault (Spencer and Reynolds, 1989). A M 3.0 earthquake with a stress drop of 60 to 100 bar slips about 1 cm at depth over a radius of 100 to 120 m (Lockridge et al., 2012; Segall 2010); therefore, small-magnitude events associated with earthquake swarms or clusters will not generate enough surface displacement ($<10^{-5}$ m) to be detectable above background noise levels in future geodetic and remote sensing studies. However, a transient pulse of aseismic creep along a mid-crustal detachment could load nearby range-bounding faults and possibly induce swarm-like activity within the interior of the GB. This mechanism could trigger a single earthquake swarm or cluster if the deformation event were highly localized, or it may also induce increased seismicity rates on multiple faults if associated with a larger-scale detachment surface.

We identify two areas in which clusters of seismic activity were temporally related (Figure 2.4). The first area consists of five separate earthquake swarms that were all active during 2012 and were located within a 30 km radius in the southwest corner of the study region. These swarms were each part of earthquake clusters within the WLFZ that were continuously active during the entire study period. There is no evidence of migration or other spatiotemporal trends associated with the peak periods of seismicity

for the 2012 swarms. The second area contains three earthquake clusters within the central GB. The seismic activity for these clusters began at the eastern swarm in July 2007 and concluded approximately 63 days later with a MS/AS sequence located 68 km to the west (Figure 2.4). Both of these sequences span several parallel sets of range bounding Quaternary faults (Figure 2.4); therefore, if the associated clusters are triggered by the same mechanism then it must be capable of impacting the entire spatial extent of these areas. If triggered by an aseismic transient displacement event along a 30 to 70 km long low-angle detachment fault within the mid-crust, it may be possible for future geophysical studies to identify such a feature. A recent study by *Hammond et al.* (2014) did not identify any transient signals within the central GB during the study period; however, the study did not utilize the Plate Boundary Observatory (PBO) geodetic stations nearest to the events. Our areas of temporally correlated seismicity are located entirely within the broad triangular sub-networks used in their strain analysis. We suggest that future studies use remote sensing data (geodesy, InSAR, etc.) to explore whether increased seismicity rates in these two regions were triggered by or associated with transient aseismic surface deformation events.

A sub-horizontal megadetachment at Moho depths (30-35 km) has been proposed as a model for GB extension (Wernicke et al., 2008). The megadetachment model suggests that region-wide transient deformation events within geodetic data may be accompanied by deep crustal seismicity within the GB (Wernicke et al., 2008). *Wernicke and Davis* (2010) report a transient deformation event in mid-2006 with decreasing westward velocities for stations in western portion of the study area. The megadetachment model also suggests that magmatic intrusions at the base of the Moho

(i.e., Smith et al., 2004) may accompany basin-wide transient deformation events (Wernicke et al., 2008). Our TA-based earthquake catalog contains no clusters of small-magnitude seismicity in association with the 2006 event, and we see no evidence of widespread deep crustal seismicity within the GB. However, our period of study was limited and future studies should continue to monitor the region for evidence of seismicity clusters in the deep crust.

The earthquake catalog generated as part of this study contains five localities in which six to eight mid- to lower-crustal earthquakes (hypocenter depths between 15 and 27 km) occur within a 10 km radius (Figure 2.6). These zones of mid- to lower-crustal earthquakes are not characterized by spatiotemporal clustering or swarm-like behavior as would be expected in association with a magma injection event similar to *Smith et al.* (2004). One potential explanation is that these zones of events with deeper focal depths are artifacts of local variations of in crustal velocity structure. However, there are very few upper crustal events located within the zones of deeper events. It is more likely that they represent scattered seismicity within regions with a depressed brittle-ductile transition. Future studies should examine focal plane solutions for events within these zones of mid- to lower-crustal seismicity to determine if they are associated with low angle normal faulting. Focal mechanisms consistent with reverse faulting would support magma injection within these areas and would be consistent with the megadetachment model of GB extension (Smith et al., 2004; Wernicke et al., 2008). Focal mechanisms that become increasingly sub-horizontal at mid-crustal depths would be consistent with ongoing detachment faulting within the GB (Chamoli et al., 2014).

2.5 Conclusions

We use USArray TA data and improved earthquake detection parameters to produce an earthquake catalog that is complete to M_c 1.5 for the GB from January 2006 to April 2009. Increasing the earthquake detection threshold within the interior of the GB allowed us to identify diffuse seismic activity across the entire region, with the exception of an apparently rigid crustal block between longitudes -114.5°E and -113° E. Widespread seismicity and active deformation across the majority of the GB (Chamoli et al., 2014; Hammond et al., 2014) dispels the model of the GB behaving as a rigid microplate with deformation and seismicity only focused at the western and eastern margins. This suggests that extension within the interior of the GB is ongoing and not limited to the more seismically active margins.

An improved earthquake detection threshold has facilitated the identification of earthquake swarms and continuously active earthquake clusters within the GB. We utilize multiple methods for the removal of human-generated seismic events from our catalogs to ensure that all spatial clusters of seismicity within the study area are tectonic in origin. Clusters of spatially correlated earthquakes are not focused within regions of recent (< 8 Ma) volcanism nor triggered by anthropogenic activity within the GB. Clusters, swarms and MS/AS sequences are distributed throughout the study region, which suggests that earthquake swarms and clusters are a general mechanism of fault behavior regardless of seismotectonic setting.

Our earthquake catalog contains two areas in which earthquake clusters are temporally associated. Within the central GB, three earthquake clusters within a region approximately 70 km wide were active between July and September 2007. Additionally,

five separate earthquake swarms were concentrated within a 30 km radius in the southwest corner of the study area in 2012. We eliminate volcanism, anthropogenic activity, dynamic stress triggering, and environmental influences such as rain and snow as potential causes for these sequences. We conclude that pore fluid pressure variation due to external geophysical phenomena such as local transient deformation events or subsurface fluid migration is the most reasonable interpretation for the cause of temporally correlated increases in seismicity rates within clusters along different range-bounding faults. To further constrain potential triggers for these areas and other clusters within our dataset, we recommend a detailed study of GPS, InSAR, and borehole strainmeter data within the study area. Additionally, swarms and clusters in this study area provide an excellent opportunity to use a waveform matching algorithm to search for evidence of non-volcanic tremor or low-frequency earthquakes (Peng and Gomberg 2010) to determine whether this type of fault behavior occurs within intracontinental environments.

CHAPTER 3

METASTABLE HIGH-PRESSURE REACTIONS IN NATURAL ENSTATITE: IMPLICATIONS FOR SLAB DYNAMICS AND DEEP EARTHQUAKES

3.1 Introduction

Enstatite $(Mg,Fe)SiO_3$ is estimated to comprise 18-25% of subducting lithosphere (Ringwood 1982; Irifune and Ringwood 1993). At equilibrium conditions, enstatite will completely dissolve into majoritic garnet by approximately 460 km depth (Akaogi and Akimoto, 1977; Irifune and Ringwood, 1987; Ringwood 1991). However, this diffusion-controlled reaction is one of the slowest processes in the mantle and is kinetically limited within the cold interior of subducting slabs (Nishi et al., 2008; van Meirlo et al., 2013). Additionally, slow chemical diffusion within the interior of cold slabs is expected to hinder the isochemical transformation of enstatite to wadsleyite plus stishovite and favor direct polymorphic transformation to akimotoite (Hogrefe et al., 1994). Kinetic inhibition of diffusion dependent equilibrium reactions in the $(Mg,Fe)SiO_3$ system have led to the interpretation that metastable enstatite can survive to the base of the mantle transition zone (MTZ) within subducting lithosphere (Hogrefe et al., 1994).

The persistence of metastable minerals into the MTZ may have significant implications for dynamics and rheology of subducting slabs. For example, the low relative density of metastable minerals may reduce subduction rates (Bina et al., 2001; Tetzlaff and Schmelling, 2009), and metastable enstatite has been recently discussed as a cause for stagnation of subducting slabs at the base of the MTZ (Nishi et al., 2013; van Mierlo et al., 2013; Agrusta et al., 2014; King et al., 2015). Additionally, rapid transformation of metastable olivine to ringwoodite has been associated with a

mechanism for the nucleation of deep focus earthquakes (Sung and Burns 1976; Green and Burnley, 1989), which can occur to depths of approximately 690 km (Kirby et al., 1996; Frohlich 2006). However, recent studies suggest that metastable olivine is unlikely to survive below 550 km within even the coldest and fastest slabs because transformation rates in olivine are greatly increased by both intracrystalline nucleation within coarse-grained olivine (Kerschhofer et al., 2000; Mosenfelder et al., 2001) and by small amounts of hydrogen within natural olivine grains (Kubo et al., 1998; Diedrich et al., 2009; Du Frane et al., 2013). Therefore, transformational faulting during the reaction of metastable enstatite to akimotoite has been suggested as a potential cause of the deepest recorded earthquakes (Hogrefe et al., 1994; Kirby et al., 1996; Frohlich 2006; Houston 2007) as well as the increase in global seismicity observed below 550 km (Persh and Houston, 2004).

Despite its potential importance to processes occurring within the mantle, to date there have been few experimental studies on the mechanisms and kinetics of polymorphic transformations in enstatite. Experimental studies investigating the nature of high-pressure phase transformations are commonly performed using hot-pressed, synthetically produced crystals. While these experiments provide idealized models for the kinetic behavior of end-member compositions, they do not account for the inclusion of minor elements (Al, OH, etc.) and other defects (inclusions, dislocations, etc.) that are common in natural samples. These factors can have a significant impact on the kinetics and mechanisms of phase transformation within the earth. For example, inclusion of <75 ppmw H_2O greatly increases transformation rates in olivine (Du Frane et al., 2013), and stacking faults in olivine can provide nucleation sites for topotaxial intracrystalline

growth of high-pressure polymorphs (Kerschhofer et al., 1996; Dupas-Bruzek et al., 1998). Additionally, rates for the transformation of olivine to wadsleyite been shown to increase with Fe content (Perrillat et al., 2013).

In this study, we perform a series of single crystal multi-anvil experiments to explore how natural compositions will impact high-pressure phase transformations in enstatite at high pressure and temperature. While we expect that experimentation with larger (~1 mm) natural crystals with potential defects will yield more complicated results, they are likely to provide a more accurate representation of processes occurring within natural systems at depth. Our results show that that nominally anhydrous Al- and Fe-bearing natural enstatite is more reactive than synthetic $MgSiO_3$, and we report the first experimental observations of intracrystalline transformation of enstatite to high-pressure polymorphs akimotoite, majorite and bridgmanite. We describe grain boundary and intracrystalline transformation of enstatite to multiple metastable high-pressure polymorphs, and we discuss the implications of these results on the metastability of enstatite within subducting slabs.

3.2 Experimental and Analytical Methodology

We investigate the behavior of enstatite at MTZ conditions by performing experiments using natural orthoenstatite (*Pbca*) crystals extracted from peridotite xenoliths collected at San Carlos, Arizona (Figure 3.1). Enstatite grains from disaggregated San Carlos xenoliths were sieved to include only crystals with a diameter range between 800 and 1000 μm. To simplify analysis of grain boundary nucleation and growth, candidate grains were rounded into spheroids using a Bond-type air mill

composed of 240 grit silicon carbide powder suspended within a marine epoxy matrix (Figure 3.2). We machine disks of grinding powder and epoxy to specifications similar to *Nitkiewicz and Sterner* (1988) and connected the mill to a filtered shop air line to grind sieved enstatite crystals into spheroids with a diameter of 600 to 800 μm. Enstatite spheroids produced in the air mill were typically prolate and elongated along the *c*-axis due to prominent {210} cleavage planes in orthopyroxene. We analyzed spheroids using a binocular optical microscope and selected samples that had the highest sphericity and were free of obvious fractures or inclusions. Selected enstatite spheroids were then placed in ethanol and ultrasonicated to remove any potential debris remaining from the ball milling process. Once cleaned, a single rounded enstatite grain was placed into a sterile container and left in a furnace at 100°C overnight to remove any potential volatiles.

We performed high-pressure phase transformation experiments using a 1100-ton multi-anvil press at Arizona State University, a COMPRESS 10/5 multi-anvil assembly (Figure 3.3a; Leinenweber et al., 2012), and custom designed silver (Ag) capsules. We used Ag capsules to minimize thermal gradients, chemical interaction between the sample and capsule, and hydrogen gain or loss during experiments (Diedrich et al., 2009; Du Frane et al., 2013). Custom Ag capsules were machined without the use of cutting oil to eliminate potential surface contamination. They were drilled using a carbide ball-end mill to produce a rounded bottom to the sample chamber, according to specifications in Figure 3.3b. We used a rounded sample chamber and introduced oil-free Ag cuttings between the enstatite grain and Ag capsule lid to reduce void space within the capsule chamber. These steps mitigate the risk of enstatite grains parting or cleaving during initial compression.

Figure 3.1. Peridotite xenoliths in basanite from Perodot Mesa within the San Carlos Apache Reservation in eastern, Arizona. Perodotite is composed of olivine, orthopyroxene, clinopyroxene and spinel.

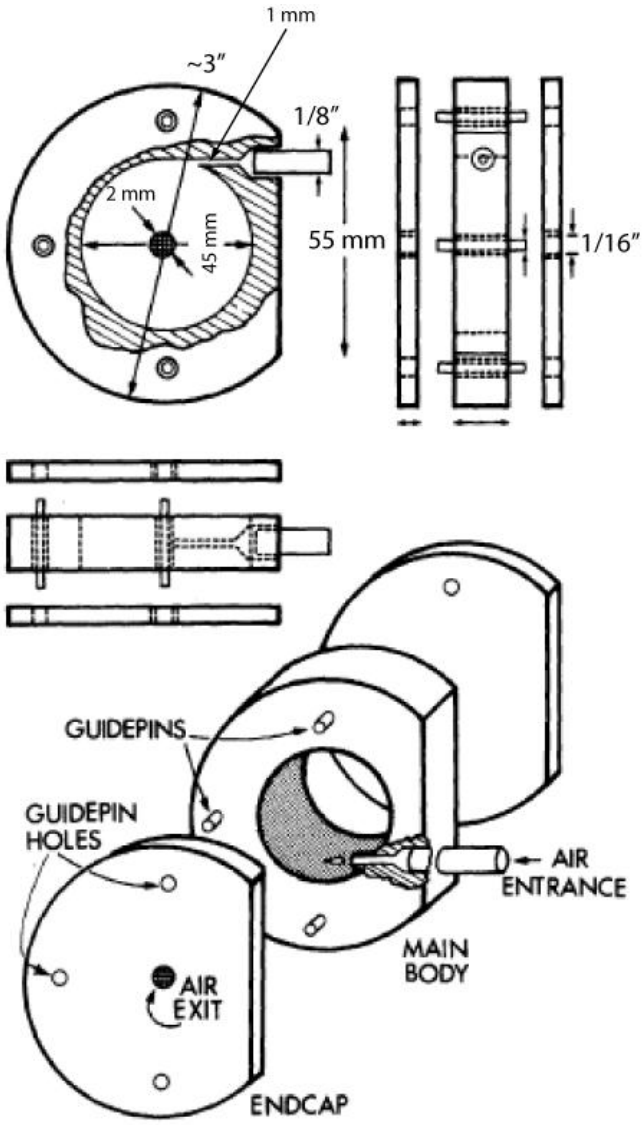

Figure 3.2. Specifications for a Bond-type air mill used to shape raw enstatite crystals into spheroidal shape. Modified from *Nitkiewicz and Sterner* (1988).

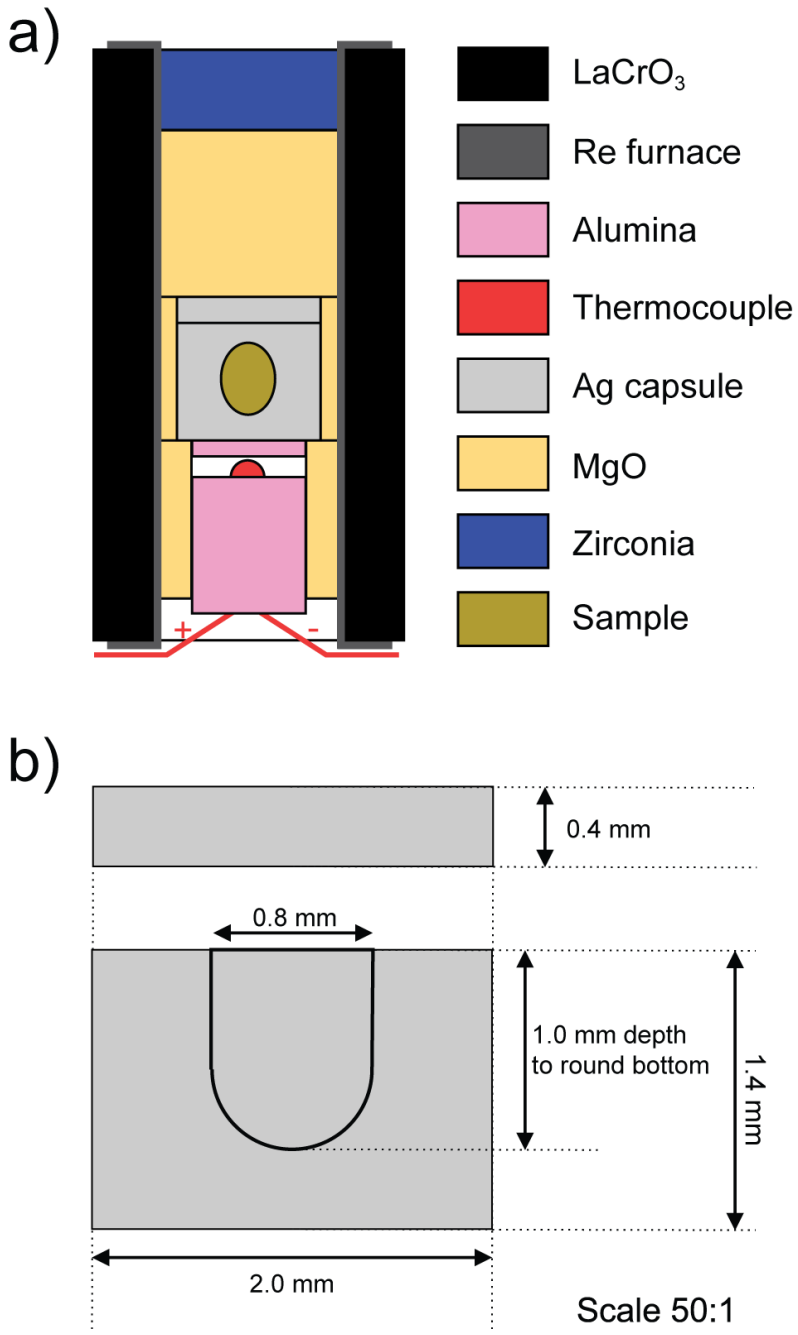

Figure 3.3. (a) Cross sectional diagram of the 10/5 multi-anvil cell assembly used for experiments in this study (Leinenweber et al., 2012). The sample is represented as green ellipse within Ag capsule. Figure not to scale. (b) Schematics for custom silver capsule designed for this study. Rounded bottom of capsule chamber produced using a 0.8 mm carbide ball end mill.

Prior to loading samples into the multi-anvil press, all assembly parts (Figure 3.3a) including the Ag capsule, Ag lid, and Ag cuttings were heated in a vacuum oven to 800°C for 10 minutes. This step removes any potential volatile contamination that may remain from machining or handling of assembly parts and anneals the Ag components to reverse effects of work hardening during machining and allows for a more efficient pressure sealing of the capsule. Once the sample and 10/5 assembly parts were cleaned, they were then placed into a desiccator until ready to be loaded into the multi-anvil press. Samples were loaded into the Ag capsule in random orientations; although, samples that were more prolate were loaded into the Ag capsule with the longer *c*-axis near vertical within the sample chamber.

We compressed experimental samples in this study to 5000 or 6640 psi oil pressure using the 17" diameter ram on the 1100 ton multi-anvil press. Pressure, as a function of press force, was calibrated from *in situ* experiments at the Advanced Photon Source at Argonne National Laboratory by *Diedrich et al.* (2009). At experimental temperatures of 1200°C to 1400°C, oil pressures are equivalent to 18.5 GPa and 21 GPa with errors estimated to be approximately ±0.5 GPa (Figure 3.4; Leinenweber et al., 2012). Once the desired pressure conditions were achieved, the furnace was heated at a rate of 100°C per minute to 1200, 1300 or 1400°C using a type-*c* thermocouple. The pressure effect of electromotive force on the thermocouple was not corrected; however, based on fluctuations in temperature readings we estimate a temperature precision of +/- 10°C for our experiments. Samples were held at the target temperature for 30 to 365 minutes and then rapidly quenched by cutting power to the furnace. Following a slow decompression, the Ag capsule containing the partially transformed enstatite sample was

extracted from the 10/5 assembly components and then encased within an epoxy resin disk to protect the sample during thin-section preparation.

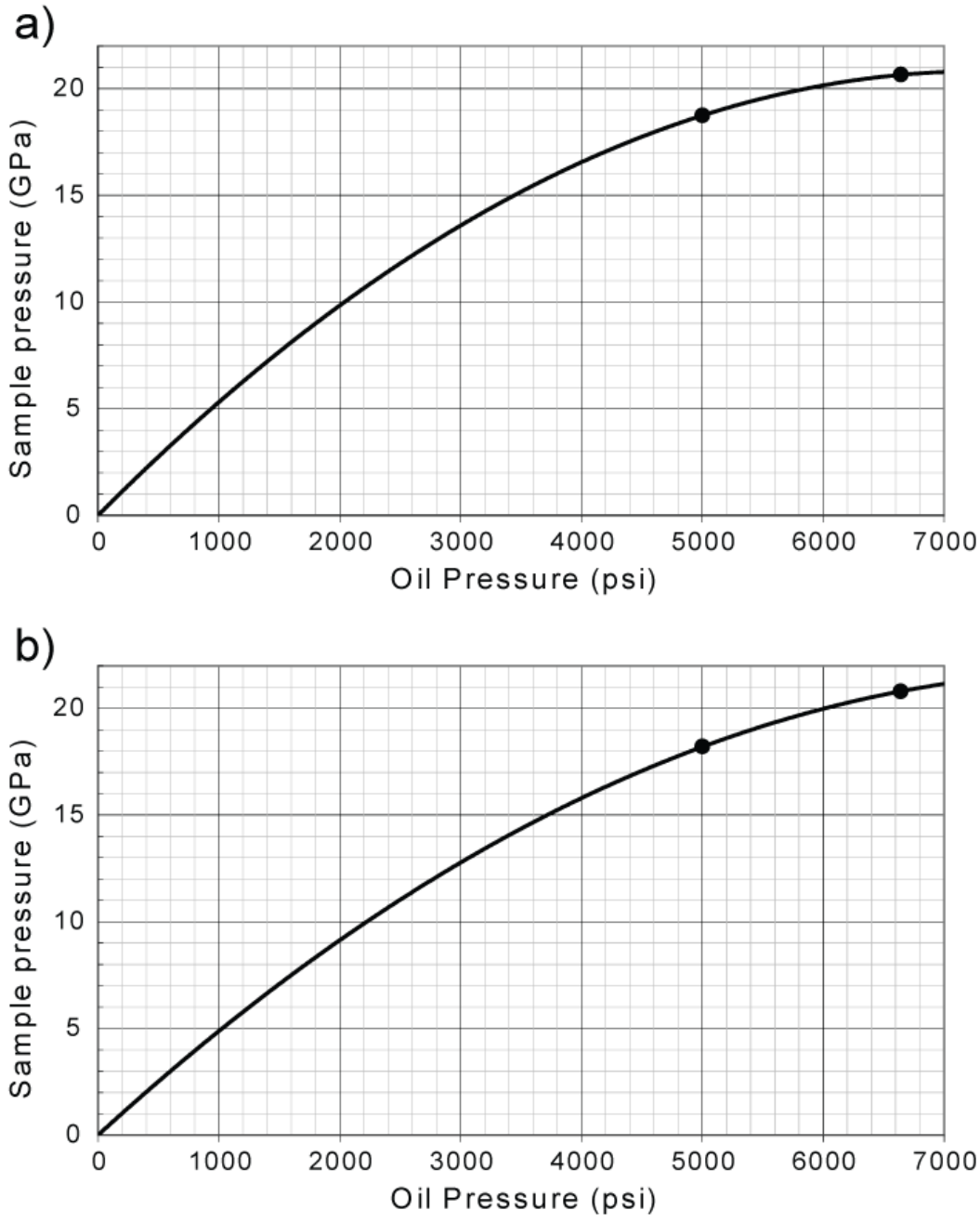

Figure 3.4. Pressure calibration curves for 1100-ton multi-anvil press at Arizona State University using the COMPRESS 10/5 multi-anvil assembly at (a) 1200°C and (b) 1400°C. Experiments in this study were performed at 5000 psi and 6640 psi oil pressure, which is equal to approximately 18.5 and 21 GPa.

We double polish the epoxy resin disk, Ag capsule, and recovered sample to thicknesses between 40-60 μm for microscopic analysis. In addition to being very brittle and prone to fracture, enstatite has two cleavage planes {210} that intersect at nearly right angles parallel to the *c*-axis. While polishing, we regularly inspect samples using both stereoscopic and petrographic microscopes to ensure that (1) interesting transformation features were not lost while polishing, (2) the polished section was at the maximum diameter for the sample, and (3) the enstatite was not being cleaved, parted, or otherwise damaged. In the event that interesting features were observed during thinning of the sample, their presence was noted and imaged using a petrographic microscope prior to continued thinning and polishing. Several recovered samples were highly cleaved or fractured while polishing, which limited analysis of the final thin section. In these cases, images taken mid-polish are the only data collected for damaged portions of samples. In addition to the six recovered experimental samples, we mounted 20 enstatite spheroids within two epoxy disks and prepared them as thin sections to fully characterize our starting material.

The reacted and unreacted enstatite grains were analyzed using a range of microscopic and spectroscopic techniques. Reflected and transmitted light microscopy was performed using an Olympus BX50 petrographic microscope. Raman spectroscopy was performed at the LeRoy Eyring Center for Solid State Science (LE-CSS) at Arizona State University using a Coherent Sapphire SF laser with a wavelength of 532 nm and a 1200 gr/mm diffraction grating. The laser has a spatial resolution of approximately 1 μm and was focused onto the sample using an 100X objective with a focal length of 0.2 mm. We sampled low pressure phases using a laser power of 12 mW; however, we generally

lowered laser power to 1.3 to 6 mW and increased sample collection times to 100s of seconds when sampling unstable high-pressure phases in recovered experimental samples.

Scanning electron microscopy (SEM) was performed using an FEI XL30 Environmental SEM with a Field Emission Gun (FEG) system at the LE-CSSS. To prevent charging, the samples were coated with a carbon film using an evaporation carbon coater. Samples were investigated primarily using backscatter electron (BSE) imaging. Imaging was performed using an acceleration voltage of 15 to 20 kV, spot size of 5.0, and working distance of 10 mm. At these settings, the instrument has a beam current of approximately 2.26 to 2.39 nA and a probe diameter of approximately 5 to 6 nm. Energy dispersive X-ray spectroscopy (EDS) was used for chemical analyses of starting material and high-pressure phases using an EDAX SiLi detector. Absorption and fluorescence effects for this system are corrected using a *ZAF* model. Process times for EDS analyses varied but were generally 4 to 10 μs to allow for at least 600 counts per second and a dead time of approximately 30%. Collection times for EDS analyses ranged from 10 seconds to over one minute, depending on the stability of the resulting spectra.

Transmission electron microscopy (TEM) was performed at the LE-CSSS using an FEI CM200-FEG. To image beam-sensitive microstructures within our starting material, we prepared TEM samples using two separate techniques; (1) a focused-ion beam (FIB) lift-out technique with an FEI Nova200 NanoLab using an acceleration voltage of 30 keV and beam current of 0.1 to 20 nA, and (2) sample thinning using a Gatan dimple grinder and a Gatan Precision Ion Milling System (PIPS) with an Ar ion beam angle of 7° from the surface and an accelerating voltage of 6 keV. We investigated

microstructures using diffraction contrast and high-resolution TEM imaging techniques. Mineral structures were identified with selected area electron diffraction (SAED). We performed chemical analysis on TEM samples by EDS using an EDAX SiLi detector, with quantitative data processing performed using the Emispec Vision system and theoretical K-factors.

3.3 Characterization of Starting Material

We used EDS on the FE-SEM to analyze chemical compositions of starting material as well as the enstatite cores of recovered experimental samples. Within recovered samples, we only selected interior enstatite regions that were at least 5 μm from high-pressure phases to avoid potential effects of chemical diffusion on our measurements. Based on EDS analyses, the average composition of starting material used in this study is $(Ca_{0.05}, Cr_{0.03,} Fe_{0.19,} Mg_{1.66}, Al_{0.07})(Al_{0.08}, Si_{1.92})O_6$ with an Mg/(Mg+Fe) ratio of 0.90 and 3.7 wt% Al_2O_3 (Table 3.1). This is in good agreement with previous studies that report Mg/(Mg+Fe) ratios of 0.93 to 0.89 and 3-5 wt% Al_2O_3 for San Carlos orthopyroxene (Frey and Prinz, 1978; Reynard et al., 2010; Zhang et al., 2012, 2014). Previous measurements of H_2O content in San Carlos enstatite range from 53 to 83 ppm based on Fourier transform infrared spectroscopy (FTIR) analyses performed by *Li et al.* (2008). This is considerably lower than values of 160-500 ppm H_2O measured for typical mantle-derived orthopyroxenes (Bell and Rossman, 1992; Grant et al., 2001; Li et al., 2008). Therefore, we consider San Carlos enstatite to be relatively low in H_2O for a natural enstatite within the mantle.

Table 3.1. Results from EDS analyses of San Carlos enstatite starting material and pyroxene cores of experimentally recovered samples.

Formula Units*	**Starting Material**		**Pyroxene Core** Sample BB1241						**Pyroxene Core** Sample BB1110		**Average**
Si	1.91	1.91	1.93	1.89	1.95	1.91	1.92	1.91	1.95	1.93	1.92
Fe	0.17	0.16	0.20	0.20	0.20	0.18	0.20	0.18	0.18	0.20	0.19
Mg	1.67	1.68	1.69	1.66	1.64	1.62	1.70	1.62	1.67	1.66	1.66
Al	0.18	0.17	0.10	0.18	0.11	0.19	0.11	0.19	0.14	0.16	0.15
Ca	0.04	0.04	0.05	0.05	0.06	0.05	0.05	0.05	0.04	0.05	0.05
Cr	0.02	0.02	0.04	0.03	0.03	0.03	0.03	0.03	0.00†	0.00†	0.03
Total	3.99	3.99	4.00	4.01	3.98	3.98	4.01	3.98	3.98	3.99	3.99
Fe/Fe+Mg	0.09	0.09	0.11	0.11	0.11	0.10	0.11	0.10	0.10	0.11	0.10

* Results given in formula units assuming pyroxene formula with 6 oxygens.
† Content of Cr not analyzed for sample BB1110.

3.4 Experimental Results

3.4.1 Nano-Fluid Inclusions within San Carlos Enstatite

Of the 20 San Carlos enstatite spheroids prepared as a control group for starting material used in this study, 14 (70%) contain abundant, but very small, rod-shaped inclusions (Figure 3.5). Due to the small size of the nano-inclusions, we were unable to identify them during a pre-screening of candidate San Carlos enstatite starting material. Based on the abundance of rod-shaped nano-inclusions within our starting material supply, there is a 0.07% chance that we were able to select six enstatite crystals that were each inclusion free. Therefore, we assume that any of our starting material could have contained nano-inclusions when loaded into the multi-anvil capsule.

Nano-inclusions are typically 0.3 to 0.5 μm by 20 to 40 μm with a single 2 to 8 μm long rod at the center (Figure 3.5a,b); however, they can also occur as series of intermittently spaced rods along a linear feature that extends throughout the entire sample (Figure 3.5c). Nano-inclusions are oriented parallel to extinction within the enstatite host

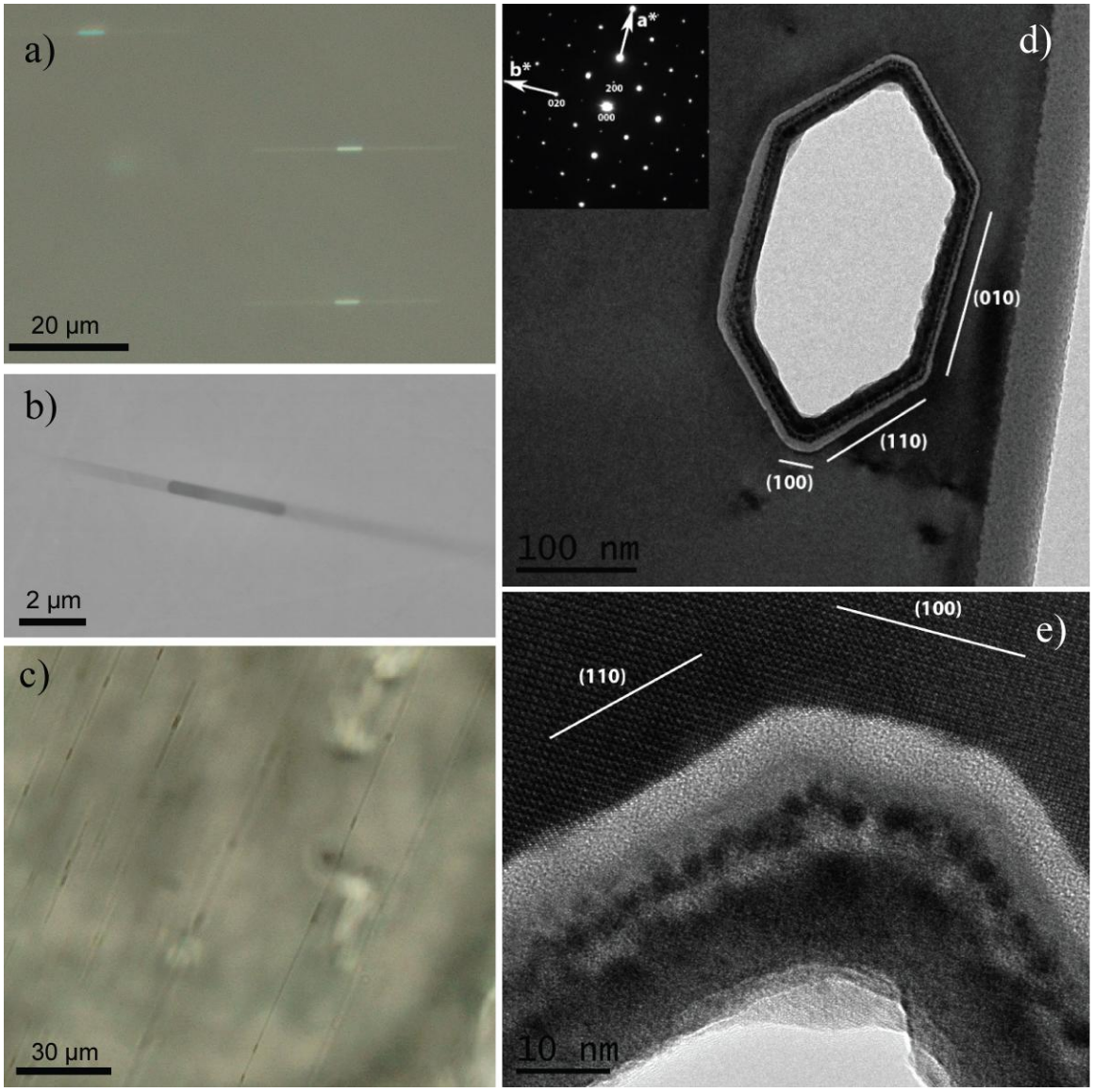

Figure 3.5. Nano-inclusions within San Carlos enstatite starting material. Optical micrographs in (a) transmitted and (b) reflected light. (c) SEM backscattered electron image of inclusion within starting material. (d, e) Brightfield TEM image of inclusions within starting material. Inset in (d) is electron diffraction pattern viewed down $[001]_{En}$ showing crystallographic orientation of principal axes within the enstatite host crystal. Note that inclusion morphology is a negative crystal with facets parallel to {100}, {010} and {110}. Material around the inner edge of the void is Pt, Ga, and Cu from the FIB milling process, with Cu form Cu grid, Pt from the Pt strap and Ga from milling with a Ga beam.

crystal in plane-polarized light images, and they are also parallel {210} cleavage planes. An orientation parallel to both cleavage and extinction within orthopyroxene can only be possible if rods are oriented along $[001]_{En}$. The mineralogy of these inclusions could not be determined using optical microscopy because their fine-scale structure is beyond the diffraction limit for visible light. The nano-inclusions are brighter than host enstatite in reflected light microscopy; therefore, they may be a highly reflective phase such as an oxide or sulfide, a fluid or vapor phase, or a void. Nano-inclusions have a lower contrast than enstatite in SEM BSE images, indicating that they have a lower atomic mass (*Z*) than host enstatite. We sampled the linear features and the rod-shaped cores of nano-inclusions using single spot EDS analyses on the SEM, and neither provided significant contribution to EDS spectra. This suggests that they are either too small to contribute significantly to the X-ray signal, or they are not chemically distinct from the host enstatite.

To analyze nano-inclusions using TEM, we cut a FIB section perpendicular to the long axis of the central rod of an inclusion. The FIB section contained a 300 nm by 150 nm void in the location where we expected to find the inclusion. This indicates that the nano-inclusions are composed of a material that is too soft to survive the FIB cutting process. The void shape is a negative crystal of the host enstatite with walls parallel to $\{100\}_{En}$, $\{010\}_{En}$, and $\{210\}_{En}$, confirming that inclusion morphology is crystallographically controlled by the enstatite host (Figure 3.5d,e). We prepared a second sample for TEM analysis using an Ar ion mill. While thinning the sample, *in situ* optical microscopy showed that the nano-inclusions were preferential sites for milling. The targeted inclusions were milled completely away when the sample was thin enough

for TEM analysis. After completing the ion milling process, we examined the sample with TEM and found only enstatite.

We collected Raman spectra from nano-inclusions that were at or very near the polished surface of starting material samples. In most cases, nano-inclusions were not Raman active because they were either (1) too small to contribute significantly to the spectra, or (2) too thin to be able to accurately targeted with the laser. However, spectra from several nano-inclusions at the surface of the samples include Raman peaks consistent with spectra of the epoxy that was used for the preparation of sample thin sections (Figure 3.6). All of the samples used in this study were rinsed with distilled water to remove dust and polishing debris from the surface prior to analysis, and no epoxy spectra were identified in any other spectra collected as part of this study. Therefore, it is possible that the Raman spectra collected while attempting to sample nano-inclusions within our starting material were instead sampling epoxy debris that had collected within voids during sample polishing. These voids may have been left behind after polishing into nm-scale fluid or vapor inclusions within our starting material.

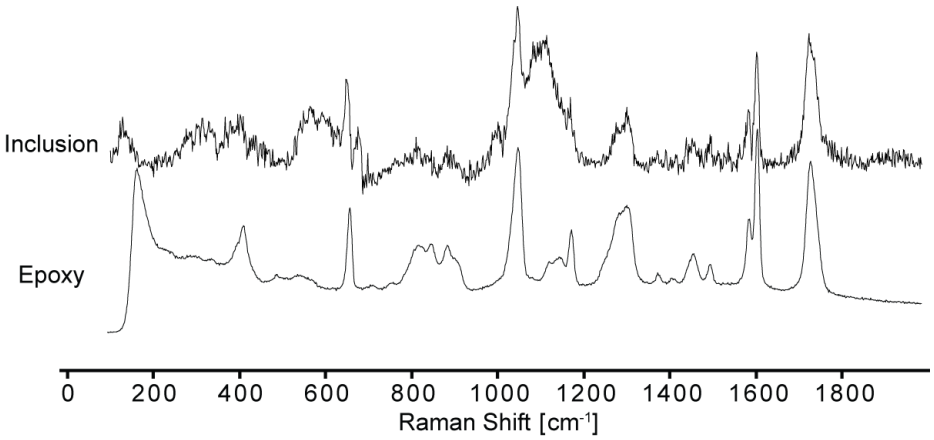

Figure 3.6. Raman spectra showing that an inclusions within San Carlos enstatite (top) contain epoxy used to prepare thin sections (bottom). Peaks associated with San Carlos enstatite have been subtracted from the spectrum of the inclusion.

3.4.2 Metastable High-Pressure Polymorphic Reactions

We examine recovered experimental samples using optical microscopy, SEM, and Raman spectroscopy to identify high-pressure phases. Samples transformed at 21 GPa were within the akimotoite stability field, yet metastable majorite and bridgmanite occur in addition to akimotoite within these samples (Table 3.2, Figure 3.7). Samples transformed at 18.5 GPa were within the wadsleyite plus stishovite and ringwoodite plus stishovite stability fields; however, Raman spectroscopy of these samples indicate the presence of only $MgSiO_3$ polymorphs. Additionally, a comparison EDS data shows that pyroxene cores and high-pressure phases have the same Si content among all phases. The common occurrence of metastable $(Mg,Fe)SiO_3$ polymorphs in all samples and the absence of decomposition reactions at spatial scales above those detectable using Raman spectroscopy and EDS suggests that metastable polymorphic reactions are favored over thermodynamically stable decomposition reactions within our experiments.

Table 3.2. Pressure-temperature-time conditions for multi-anvil experiments and high-pressure phases confirmed using Raman spectroscopy.

Sample ID	*P* (GPa)	*T* (°C)	*t* (min)	High-Pressure Phases	
				(Rim)	(Intracrystalline)
BB1166	18.5	1200	365	aki	aki*
BB1158	18.5	1400	60	aki,maj	aki, maj
BB1062	21	1200	220	aki, maj	aki, maj
BB1241	21	1300	90	aki, maj, brd	aki, maj, brd
BB1244	21	1300	300	aki, brd	aki, brd
BB1110	21	1400	30	aki, maj, brd	aki, maj, brd

* Akimotoite occurs near rim and may be associated with grain boundary nucleation.

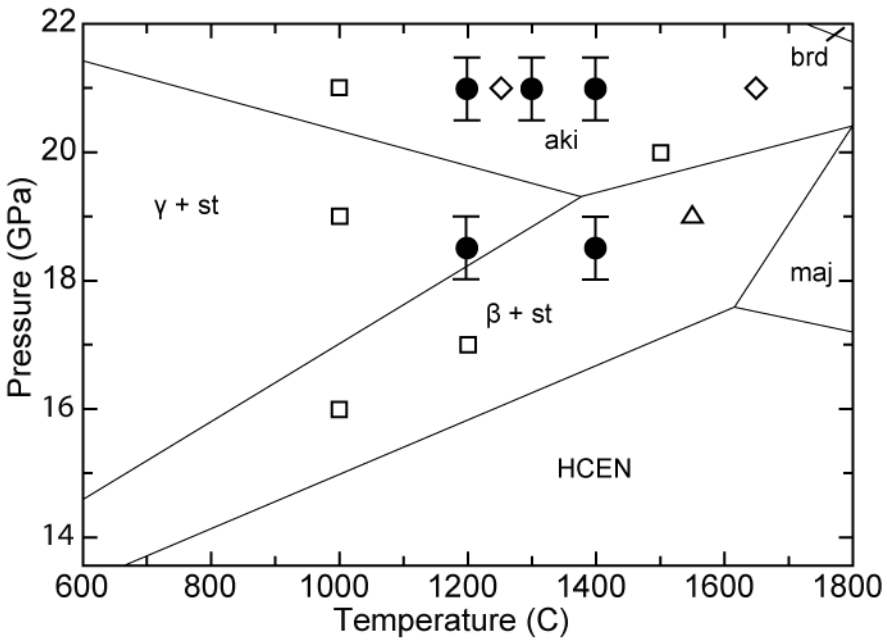

Figure 3.7. Phase diagram for end-member $MgSiO_3$ composition computed using PERPLEX software (Connolly 2009) with thermodynamic models and parameterization from (Stixrude and Lithgow-Bertelloni 2011). Black lines are equilibrium boundaries for $MgSiO_3$ system with phases (β=wadsleyite; γ=ringwoodite; st=stishovite; aki=akimotoite; maj=majorite; brd=bridgmanite; HCEN=high-clinoenstatite). Solid black circles represent experiments performed as part of this study with error in pressure indicated for each. White polygons represent transformation experiments in which *Hogrefe et al.* (1994) observed no transformation (squares), complete transformation to akimotoite (diamonds), and minor transformation of to wadsleyite plus stishovite (triangle) using end-member $MgSiO_3$.

3.4.3 High-Pressure Phases within Reaction Rims

Within solid-state transformation experiments, reactions occur as a result of heterogeneous nucleation along grain boundaries (Rubie and Ross, 1994). As transformation progresses, a polycrystalline reaction rim of incoherent high-pressure phases grows towards the interior of the host grain. Within our experiments, polycrystalline reaction rims of high-pressure phases occur in all samples. The occurrence and associations of high-pressure phases within reaction rims vary depending on experimental conditions (Table 3.2). At 18.5 GPa and 1200°C (BB1166), the reaction

rim consists entirely of akimotoite. At 18.5 GPa and 1400°C (BB1158), Raman spectroscopy shows that the reaction rim is primarily majorite; however, portions of the extreme outer margin of the rim contain both akimotoite and majorite (Figure 3.8). At 21 GPa and 1200°C (BB1062), the polycrystalline reaction rim is primarily akimotoite; however, some regions within the reaction rim contain weak Raman peaks at 595 cm^{-1} and 930 cm^{-1} indicating the presence of lesser amounts of majorite. Zones of majorite within the reaction rim of this sample are not clearly distinguishable from areas of akimotoite in BSE or optical images.

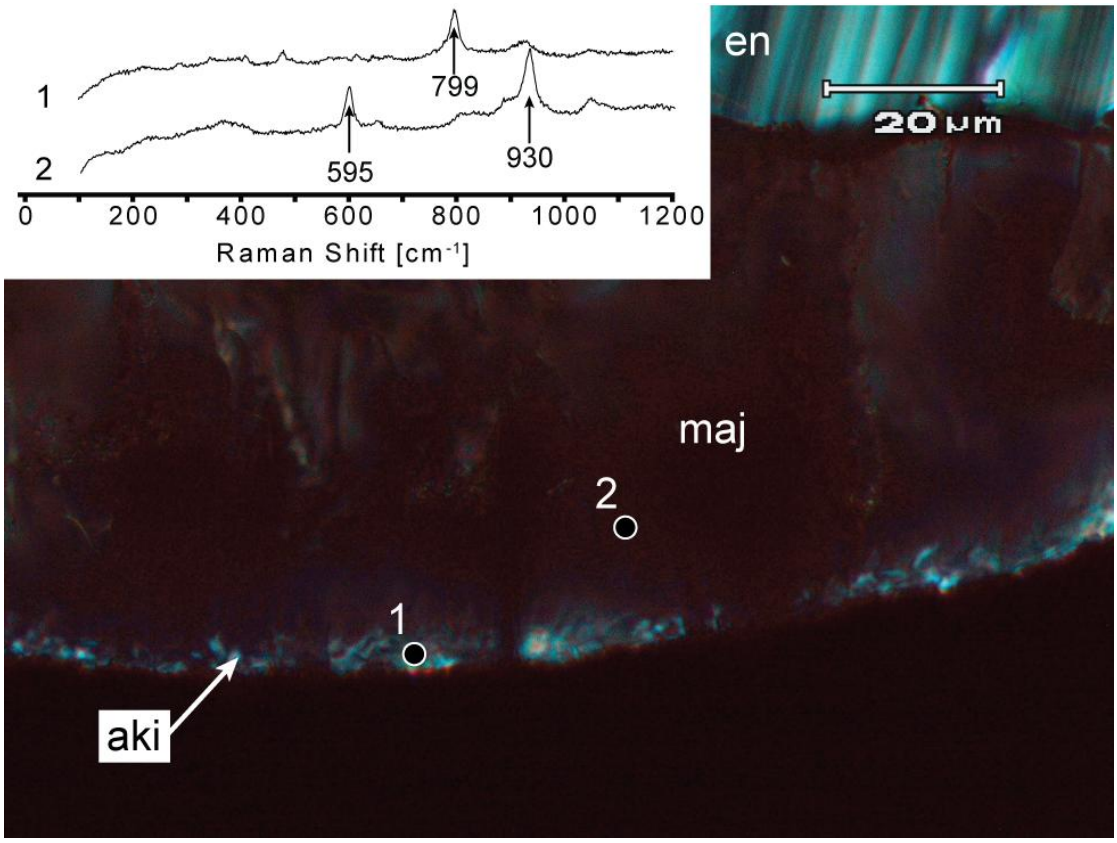

Figure 3.8. Optical micrograph of the reaction rim in sample BB1158 (18.5 GPa, 1400°C) using cross polarized transmitted light with condenser lens inserted. Outer edge of sample rim is akimotoite (aki) with characteristic Raman peak at 799 cm^{-1}. Dominant phase within the reaction rim is majorite, confirmed by Raman peaks at 595 cm^{-1} and 930 cm^{-1}.

The samples transformed at 21 GPa and 1300 to 1400°C have a more complex phase assemblage within their reaction rims. The outermost rim in these samples is a mixture of fine-grained akimotoite and bridgmanite, while the interior of the rims contains majorite, akimotoite, or a mixture of both majorite and akimotoite (Figure 3.9). Within reaction rims, bridgmanite is always associated with akimotoite and appears as a bright phase in BSE images. Akimotoite occurs in isolation towards the interior of the reaction rim in these samples and is distinguished from other high-pressure phases in BSE images by its dark contrast. The thickness of the bridgmanite and akimotoite zone

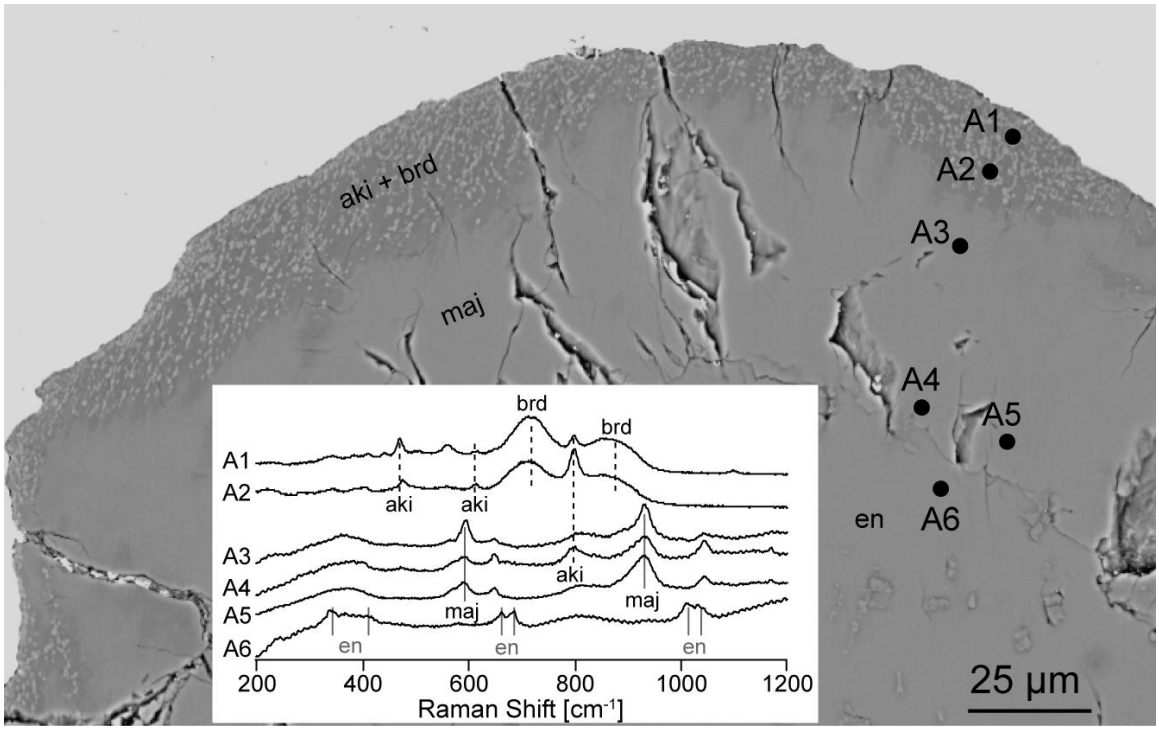

Figure 3.9. Backscatter electron image of high-pressure phases within reaction rim of sample BB1110 transformed at 21 GPa and 1400°C. Inset shows Raman spectra for selected points within the rim and core of the sample. Bright phase at the edge of the rim is bridgmanite (brd), identified by broad Raman peaks at 732 cm^{-1} and 897 cm^{-1}. Akimotoite (aki) is dark phase at outer portion of rim, identified by a strong Raman peak at 799 cm^{-1}. Majorite (maj) is at neutral contrast with enstatite (en) core and is identified by peaks at 595 cm^{-1} and 930 cm^{-1}

within the outer portion of reaction rims is strongly temperature dependent, as it is only 2 to 5 μm thick in each of the experiments transformed at 21 GPa and 1300°C but is up to 25 μm thick within sample BB1110 (21 GPa, 1400°C). We were unable to identify bridgmanite with TEM. This is probably because bridgmanite is highly unstable at ambient pressures and is easily vitrified during FIB-section preparation and TEM analysis. While Raman spectra of the phase did not contain lower modes typical of bridgmanite, data from our samples contain broad peaks at 732 cm^{-1} and 897 cm^{-1} that are consistent with published spectra of $MgSiO_3$ perovskite (Bolfan-Cassanova et al., 2003).

We used EDS to investigate chemical variations within the outer portion of the reaction rim within the sample transformed at 21 GPa and 1400°C. Relative atomic percentages of cations within each sampled phase were normalized to satisfy charge balance in the $(A,B)_2Si_2O_6$ pyroxene formula (Table 3.3). EDS spectra from the brighter high-contrast phase shows four compositional variants, including a phase that is nearly isochemical with starting material except for slightly elevated Fe levels (Type 1), a high Mg phase with low Fe and Al (Type 2), a phase with high Fe and Al and low Mg (Type 3), and a phase with low Si and high Fe, Mg, and Ca (Type 4). The EDS data from the darker low-contrast phase between bright spots has two compositional variants, a phase with the same composition as starting material (Type A) and a phase with low Fe and high Mg (Type B). Therefore, at high temperatures, phase transformations within the outer portion of the reaction rims are more complex than simple isochemical polymorphic reactions.

We performed TEM analyses on a FIB section extracted from the outer portion of the reaction rim in Sample BB1110 (21 GPa, 1400°C). Based on electron diffraction data,

Table 3.3. EDS analyses of bright phase and dark phase within the outer portion of the reaction rim in Sample BB1110 (21 GPa, 1400°C).

Formula Units*	Starting Material	Bright Phase†				Dark Phase†	
		Type 1	Type 2	Type 3	Type 4	Type A	Type B
Si	1.94	1.93	1.95	1.95	1.84	1.93	1.93
Fe	0.19	0.22	0.11	0.25	0.26	0.20	0.11
Mg	1.66	1.65	1.75	1.54	1.75	1.66	1.79
Al	0.15	0.16	0.12	0.18	0.15	0.14	0.14
Ca	0.04	0.04	0.05	0.04	0.08	0.06	0.03
Total	3.98	4.00	3.99	3.96	4.08	3.99	4.00
Fe/Fe+Mg	0.10	0.12	0.06	0.14	0.13	0.11	0.06

* Results given in formula units assuming pyroxene formula with 6 oxygens.
† All values are averages from spectra sampled within the outer 25 μm of reaction rim where both akimotoite and bridgmanite are present.

akimotoite is the only crystalline phase within this FIB section and the remainder of the sample is composed of amorphous phases. We performed EDS analyses on the FIB section and identified three distinct compositions for amorphous material, including (1) grains with similar compositions as our starting material, (2) a calcium rich grain containing elemental proportions consistent with $CaSiO_3$, and (3) an amorphous SiO_2 phase. The formation of amorphous SiO_2 and $CaSiO_3$ phases is an indication that long-range diffusion and elemental partitioning occured during the nucleation and growth of high-pressure phases in samples transformed at the highest pressures and temperatures.

3.4.4 Intracrystalline Growth of High-Pressure Phases

Each of our experiments produced growth of high-pressure $(Mg,Fe)SiO_3$ polymorphs within the interior of the samples. Intracrystalline transformation features have multiple morphologies and crystallographic orientations relative to the pyroxene host, which suggests that each type of feature has a different nucleation and growth mechanism. A detailed analysis of these mechanisms is beyond the scope of this study.

Here we document the occurrence and associations of (Mg,Fe)SiO_3 polymorphs within sample interiors.

Sample BB1166 (18.5 GPa and 1200°C) became heavily fractured and damaged during polishing. Optical micrographs were taken during the polishing process to document features before they were damaged. A 30 by 40 µm intracrystalline growth composed of akimotoite was clearly visible within this sample in optical microscopy (Figure 3.10). This feature was only 20 to 30 µm from the reaction rim and there are other regions where the akimotoite extends 30 µm into the interior of the sample; therefore, it is unclear whether the growth feature is associated with irregular growth of a reaction rim or whether it represents akimotoite growth via an intracrystalline nucleation mechanism. The intracrystalline feature was not preserved in the final thin section of

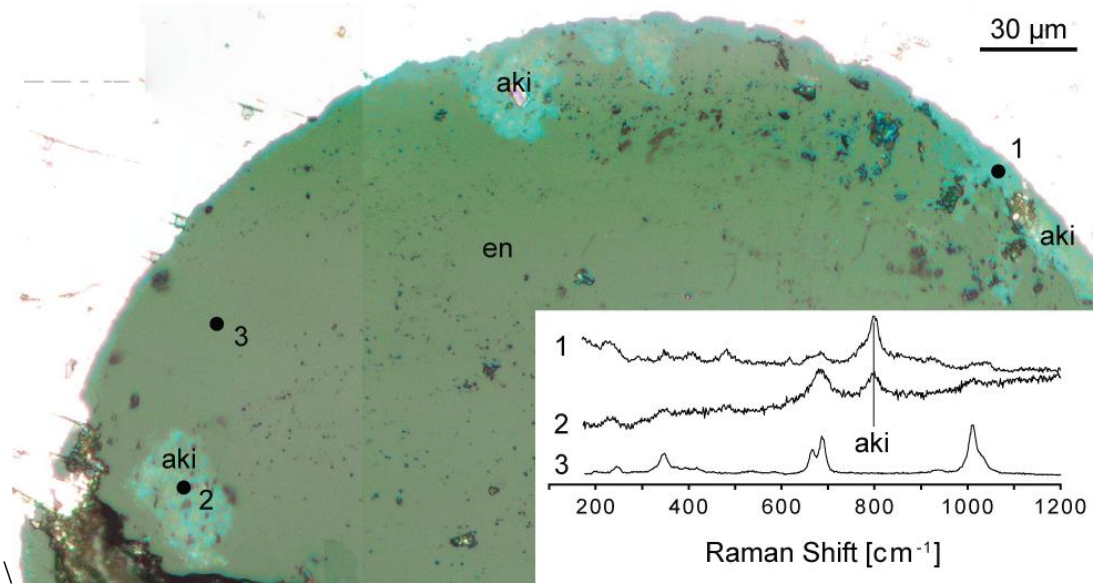

Figure 3.10. Mosaic of high resolution reflected light micrographs of sample BB1166 (18.5 GPa, 1200°C) taken during sample thinning and thin section preparation. Images were taken to document features that would be destroyed by further thin section preparation. Dark features on the surface are pits, fractures, and debris from sample polishing. Inset contains Raman spectra of (1) akimotoite (aki) reaction rim with characteristic aki peak at 799 cm^{-1}, (2) intracrystalline growth feature, and (3) enstatite core.

sample BB1166 due to either continued removal of material during thinning or additional fracturing, and the final polished thin section of this sample contained no other intracrystalline growth features.

Within the sample BB1158 (18.5 GPa, 1400°C), a 10 μm-wide plane of polycrystalline akimotoite has a near vertical intersection with the sample thin section. Similar features are also present in BB1110 (21 GPa, 1400°C) and are possibly caused by grain boundary nucleation of akimotoite along a preexisting cleavage surface or some other planar feature within the sample that was present prior to sample heating. Sample BB1158 also contains intracrystalline growth of majorite that occurs as either (1) 10 to 15 μm tusk-shaped features that extend radially from the reaction rim towards the core of the sample or (2) irregular areas of majorite growth that occur along fractures within the enstatite core.

Within sample BB1062 (21 GPa, 1200°C), intracrystalline growth of akimotoite occurs along elongated features that are generally less than 1 μm to 5 μm in width. Larger features up to 15 μm or more in length have Raman spectra with low intensity peaks that are consistent with majorite. There are several areas within the sample where intracrystalline growth is significantly larger and more nodular in shape than the other elongated features. These areas appear to be locations where several larger strands have grown together, and Raman spectra for these features have higher intensity majorite peaks.

Samples transformed at 21 GPa and 1300°C to 1400°C contain bridgmanite lamellae that are up to 2 μm wide (Figure 3.11). The bridgmanite lamellae can occur in

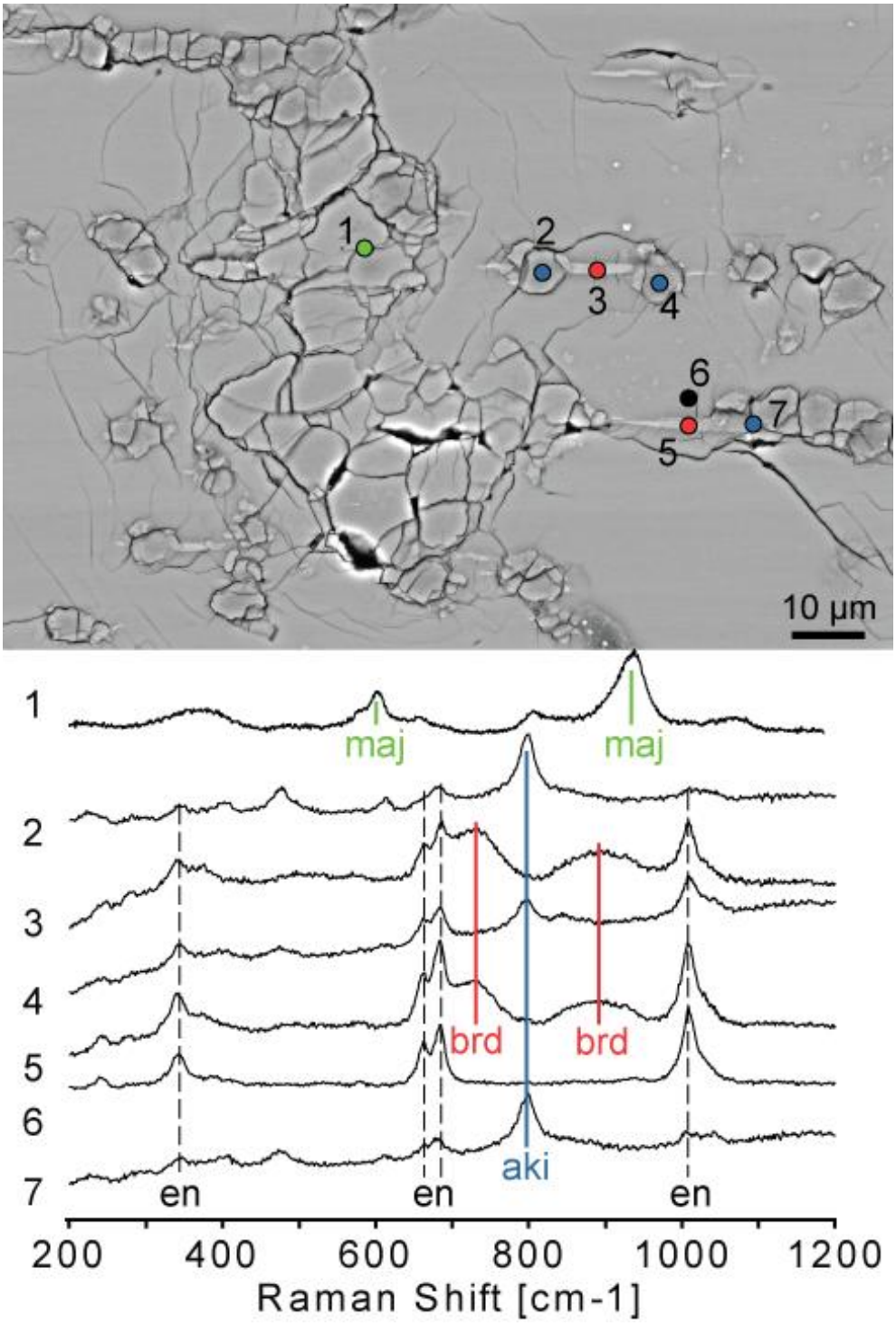

Figure 3.11. Top: Backscatter electron image of intracrystalline growth features within BB1241 (21 GPa, 1300°C). Numbered circles represent areas sampled by Raman spectroscopy (bottom) and are color coded by dominant high-pressure phases. Akimotoite (aki) is blue; majorite (maj) is green, and bridgmanite (brd) is red.

isolation from other high-pressure phases; however, they most commonly occur at the ends of 5 to 10 μm wide bands of akimotoite or nodular-shaped regions of majorite and akimotoite that are approximately 30 to 50 μm in diameter. This suggests that the bridgmanite may be the first to form, providing nucleation sites for other high-pressure phases within the interior of the host pyroxene grain. Intracrystalline majorite within 21 GPa samples is always associated with akimotoite and occurs only within larger nodular intracrystalline growth features. For sample BB1244 (21 GPa, 1300°C), we selected a more ellipsoidal grain to have a better idea of crystallographic orientation in optical thin section. The prolate ellipsoid was loaded into the capsule chamber with the longer *c* axis along the capsule rotation axis. We produced a thin section roughly parallel to $(001)_{En}$ by polishing a cross section of the recovered capsule perpendicular to the capsule axis.

Carful observation during thin section preparation allowed for the identification of rod-shaped intracrystalline growth features that were nearly vertical within the sample (Figure 3.12). These features are semi-rounded in optical thin section, approximately 5 to 10 μm in diameter and, based on Raman spectra, are entirely composed of akimotoite. Focusing and defocusing the akimotoite rods in optical microscopy shows that they project down into the sample thin section along the same plunge as the linear intersection of cleavage planes within the pyroxene host; therefore, the rods are parallel to $[001]_{En}$. Similar semi-rounded intracrystalline growth features approximately 5 to 10 μm in diameter are within thin sections of each sample transformed at 21 GPa and 1300°C to 1400°C; however, these samples were not pre-oriented within the capsule and crystallographic relation of these features to their respective enstatite hosts has not been determined.

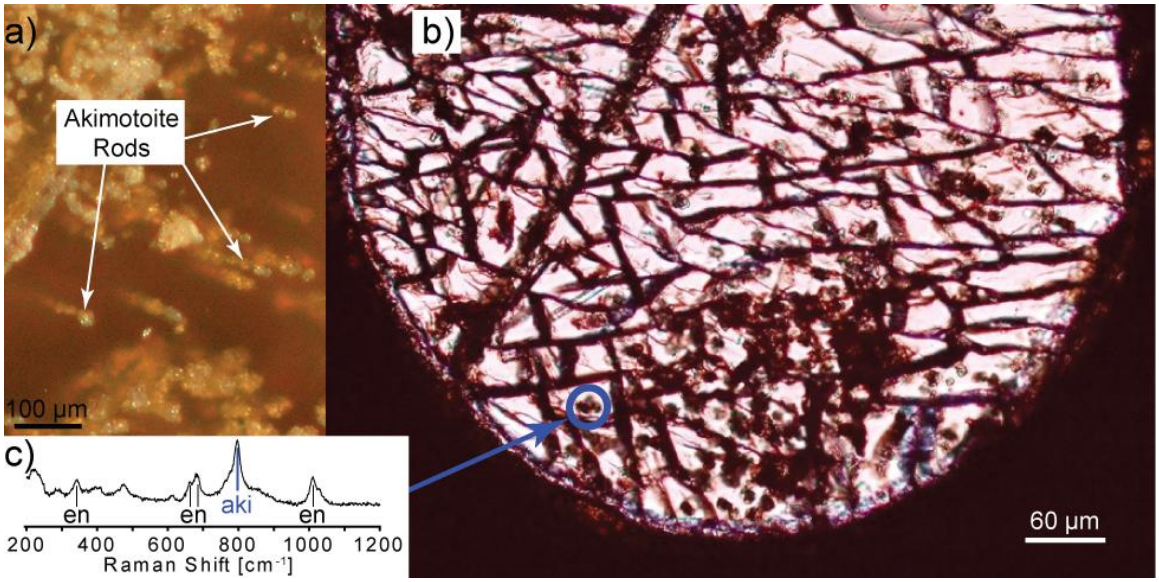

Figure 3.12. (a) Photomicrograph taken under incandescent light while thinning sample BB1241 (21 GPa, 1300°C). Rods of akimotoite project down into the partially thinned sample. (b) Transmitted light photomicrograph displaying pyroxene cleavage planes (dark lines) and intracrystalline growth (dark spots). (c) Raman spectrum taken from semi-rounded cross section of akimotoite rods within final polished thin section.

3.5 Discussion

3.5.1 Metastable Polymorphic Reactions in Natural Enstatite

As subducting oceanic lithosphere enters the MTZ, the interior of the slab can be as much as 900°C to 1000°C colder than the surrounding mantle (Kirby et at., 1996; Collier et al., 2001). These low temperatures can inhibit transformation of enstatite to equilibrium phase assemblages of wadsleyite and ringwoodite plus stishovite and will favor direct transformation of enstatite to metastable high-pressure polymorphs (Hogrefe et al., 1994; Tomioka 2007). To better understand metastable reactions within each of our recovered experimental samples, we created a phase diagram that displays both equilibrium phase boundaries within the $MgSiO_3$ system and metastable phase boundaries between enstatite and each of its high-pressure polymorphs (Figure 3.13). The

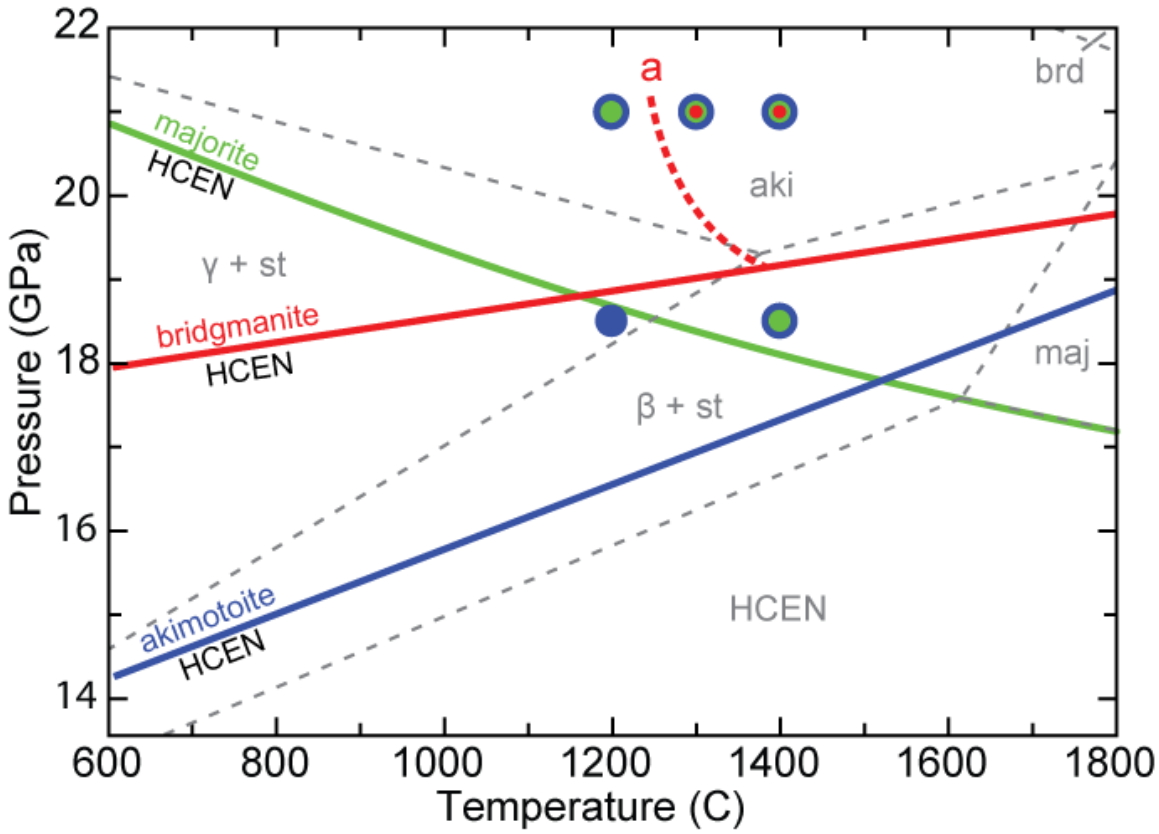

Figure 3.13. Phase diagram for end-member $MgSiO_3$ composition computed using Perple_X software (PERPLEX 2015) with thermodynamic models and parameterization from *Stixrude and Lithgow-Bertelloni* (2011). Dashed grey lines are equilibrium boundaries for high-pressure phases within the $MgSiO_3$ system: wadsleyite (β), ringwoodite (γ), stishovite (st), akimotoite (aki), majorite (maj) bridgmanite (brd), and high-clinoenstatite (HCEN). Colored solid lines are metastable boundaries for each high-pressure $MgSiO_3$ polymorph relative to HCEN. Colored circles correspond to high-pressure phases present within experiments performed as part of this study (blue=aki; green=maj; red=brd). Dashed red line (a) is experimentally constrained kinetic boundary for metastable brd-HCEN boundary.

metastable phase boundaries in Figure 3.13 represents conditions where the Gibbs free energy between enstatite and each high-pressure polymorph are equal. Within our recovered experimental samples, transformation of enstatite to a specific metastable high-pressure polymorph occurs only at pressure and temperature conditions where that polymorph is metastable relative to the enstatite starting material (Figure 3.13). In other words, enstatite may transform to any metastable high-pressure polymorph, provided that

it requires less energy to grow that polymorph than it does to maintain enstatite starting material at high pressures and temperatures. For example, the presence of akimotoite within all samples is consistent with each of the six experiments being performed at conditions where akimotoite is thermodynamically stable relative to high-clinoenstatite. Additionally, all experiments except BB1166 (18.5 GPa, 1200°C) were performed above the metastable enstatite-majorite boundary, and BB1166 is the only sample in this study that does not contain majorite. Finally, experiments at 21 GPa were performed at conditions in which bridgmanite is stable relative to enstatite, and bridgmanite was detected using Raman spectroscopy in all 21 GPa samples except for BB1062 (1200°C). The absence of bridgmanite at 1200°C suggests that a kinetic barrier may exist for the enstatite-bridgmanite reaction between 1200°C and 1300°C (Figure 3.13).

The growth of multiple metastable phases within many samples suggests that kinetic factors control which phase will nucleate when more than one $(Mg,Fe)SiO_3$ polymorph is stable relative to enstatite starting material. For example, within the interior of samples transformed at 21 GPa and 1300°C to 1400°C, bridgmanite lamellae occur (1) in isolation with no other high-pressure phases present, (2) extending out from 5 to 10 μm wide bands of akimotoite, or (3) extending from nodular-shaped areas of majorite and akimotoite that are approximately 30 to 50 μm in size (Figure 3.11). While the nucleation mechanism for the growth of bridgmanite lamellae is unclear, it appears that heterogeneous nucleation of akimotoite occurs along grain boundaries of bridgmanite lamellae. The absence of a bridgmanite core within the akimotoite bands indicates that the bridgmanite was kinetically easier to nucleate initially, but was later replaced by more thermodynamically stable akimotoite. A similar process may be responsible for

intracrystalline growth of majorite; although, details of this reaction were not examined as part of this study.

3.5.2 Increased Reactivity of Natural Enstatite Relative to Pure-$MgSiO_3$

Our samples of San Carlos enstatite transform to high-pressure polymorphs much more readily than experiments by *Hogrefe et al.* (1994), who observed transformation of pure-$MgSiO_3$ enstatite to akimotoite only above 21 GPa and reported no transformation of enstatite after 30 hours at 1500°C and 20 GPa (Figure 3.5). An increased threshold for observable reactions in enstatite can be caused by several notable differences in experimental design between the current study and *Hogrefe et al.* (1994). The previous study used a powdered mixture of end member $MgSiO_3$ enstatite and Mg_2SiO_4 forsterite, and samples were annealed to create an equilibrium microstructure within starting material. In the present study, we use single crystals of natural Al- and Fe-bearing enstatite to simulate a complex chemistry, larger grain sizes, and the presence of defects expected for natural crystals within the mantle. The potential for each of these differences to increase the threshold for reactions in natural enstatite is discussed below.

To explore effects of the addition of Al and Fe on the metastable boundaries, we modeled phase diagrams in which 10 mol% Al and Fe were separately added to the $MgSiO_3$ system (Figure 3.14). The addition of 10 mol% Al and Fe is significantly more than 3-5 mol% Al and 5-7 mol% Fe measured for our starting material using EDS (Table 3.1). The addition of 10 mol% Al decreases the pressure of the high-clinoenstatite to majorite metastable boundary, and the addition of 10% Fe increases the pressure of the high-clinoenstatite to majorite metastable boundary. The addition of 10% Al and 10% Fe

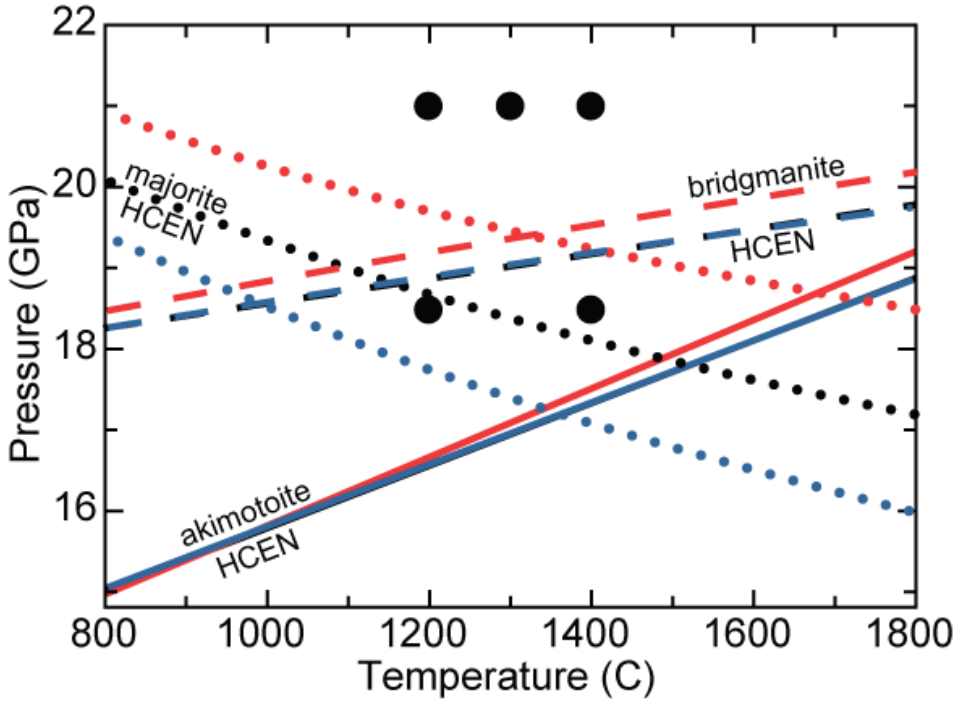

Figure 3.14. Phase diagram containing metastable boundaries for $MgSiO_3$ polymorphs relative to high-clinoenstatite (HCEN). Three lines plotted for each metastable boundary are for end-member $MgSiO_3$ composition (black), $MgSiO_3$ with 10 mol% Al added to the system (blue), and $MgSiO_3$ with 10 mol% Fe added to system (red). Solid black circles represent experiments performed as part of this study. Phase boundaries were computed using Perple_X software (Connolly 2009) with thermodynamic model and parameterization from *Stixrude and Lithgow-Bertelloni* (2011).

appeared to have little effect on the metastable boundaries between high-clinoenstatite and both akimotoite and bridgmanite. Based on these calculations, the net effects of compositional variations in our starting material from pure $MgSiO_3$ enstatite do not appear to be a significant control on phase stability.

Mantle-derived orthopyroxenes typically contain between 160-500 ppm H_2O (Bell and Rossman, 1992; Grant et al., 2001; Li et al., 2008). Previous studies have shown that as little as 75 ppm H_2O can greatly increase transformation rates within olivine (DuFrane et al., 2013). Therefore, it is possible that increased reactivity within

our experiments (relative to previous results using anhydrous $MgSiO_3$ enstatite) is due to the inclusion of nominal amounts of H_2O within natural San Carlos enstatite. However, at 80 ppm H_2O, San Carlos enstatite represents a lower limit for water content of orthopyroxene in the mantle (Li et al., 2008). If the nominal H_2O content of San Carlos enstatite starting material is the primary reason for the increased reactivity in our experiments compared to previous studies using pure synthetic $MgSiO_3$ starting material, then our experimental results are more representative of processes occurring within subducting oceanic lithosphere. Future studies should characterize the impact of nominal amounts of H_2O on the kinetics of phase transformations in enstatite by performing a series of experiments using starting material with varying amounts of H_2O (i.e. Diedrich et al., 2009; Du Frane et al., 2013).

3.5.3. Kinetic Controls on Polymorphic Transformation within Reaction Rims

A polycrystalline reaction rim of high-pressure phases was produced along the outer margin of the enstatite host grain in all of the experiments performed as part of this study. Samples transformed at 18.5 GPa were in either the wadsleyite plus stishovite stability field or the ringwoodite plus stishovite stability field; however, these samples contain no detectible eutectoid-type reactions to silica and olivine polymorphs. At 21 GPa, the only indication of eutectoid-type reactions was a single nm-scale amorphous SiO_2 grain detected during TEM analysis of the reaction rim within the sample transformed at 1400°C. *Hogrefe et al.* (1994) reported minor transformation of pure-$MgSiO_3$ enstatite to wadsleyite at 1550°C and 19 GPa. The sluggishness of eutectoid-type reactions within enstatite has been attributed to difficulty of long-range diffusion of

Mg and Si that is required for simultaneous growth of Mg_2SiO_4 and SiO_2 product phases (Hogrefe et al., 1994). The scarcity of Mg_2SiO_4 and SiO_2 polymorphs within our experiments suggests that a kinetic barrier also exists for the reaction of natural enstatite to wadsleyite or ringwoodite plus stishovite. Therefore, metastable polymorphic reactions are expected to dominate within natural enstatite at temperatures where diffusion-controlled processes are limited.

Reaction rims in all three samples transformed at 21 GPa and 1300°C to 1400°C contain a multi-phase assemblage of akimotoite and amorphous bridgmanite (Figure 3.9). This akimotoite-bridgmanite zone occurs only in the outer portions of the reaction rims, and the interior of each rim is composed of akimotoite or majorite. Solid-state transformation experiments using single crystals of olivine have shown that the large volume decreases associated with high-pressure polymorphic reactions cause elastic strain energy to build up between reaction rims and untransformed cores (Liu et al., 1998; Mosenfelder et al., 2000; Morris 2002). The thickness of the bridgmanite plus akimotoite zone within the outer rims of both 21 GPa and 1300°C samples ranges from 2 to 5 μm despite experiment durations differing by 3.5 hours (Table 3.1). If the large volume change associated with enstatite to bridgmanite and akimotoite reactions accumulated elastic strain within the outer rim of these samples, any experiment run at the same set of pressure and temperature conditions would have transformation rates drop to zero at the same time resulting in uniform final rim thicknesses. Therefore, within the 21 GPa and 1300°C samples, a similar width of the akimotoite-bridgmanite zone for different run durations indicates that growth of this phase assemblage is likely to have been slowed by the buildup of elastic strain from the volume change in these reactions.

3.5.4 Fluid Inclusions as a Catalyst for Polymorphic Reactions

Nano-scale rod-shaped inclusions are present within 70% of the untransformed San Carlos enstatite crystals analyzed in this study. These nano-scale inclusions are oriented along $[001]_{En}$ have a negative crystal form that is crystallographically controlled by the enstatite host (Figure 3.5). They are not Raman inactive, do not survive FIB or ion milling processes, have a low *Z* in BSE imaging, and a high contrast in reflected light microscopy. Based on negative crystal form of the inclusions, we conclude that the nano-inclusions within San Carlos enstatite formed as fluid inclusions during the growth of the host crystals.

Since 70% of the San Carlos enstatite starting material we characterized contained nano-fluid inclusions, there is a 0.07% chance that we selected six inclusion-free San Carlos enstatite samples from our starting material supply. Thus we assume that any of our samples may have contained nano-fluid inclusions prior to being loaded into the multi-anvil apparatus. However, no nano-fluid inclusions are present within the untransformed enstatite cores of recovered experimental samples. Because a fluid or gas filled inclusion would not survive under experimental conditions used in this study, it is likely that any nano-fluid inclusions were resorbed into the enstatite host grain during compression and heating during the multi-anvil experiments.

Resorbed nano-fluid inclusions within starting material may enhance growth of high-pressure phases within the interior of enstatite grains in several ways. First, the closing of a fluid inclusion could result in the development of stacking faults or other structural defects within natural enstatite grains. In previous studies using olivine, stacking faults have been shown to serve as heterogeneous nucleation sites for high-

pressure phases (Kerschhofer et al., 1996; Dupas-Bruzek et al., 1998). Second, fluid inclusions provide areas of elevated H_2O or CO_2 content that produce pathways of high diffusivity (Carter et al., 2015). Nano-fluid inclusions within enstatite could result in a zone of high diffusivity along $[001]_{En}$, generating rod-shaped growths of high-pressure phases within the interior of enstatite crystals. Experimental samples transformed at 21 GPa contain rods of polycrystalline akimotoite parallel to $[001]_{En}$ (Figure 3.12). These results suggest that nan-fluid inclusions were present within host enstatite grains prior to experimentation and they contributed to intracrystalline nucleation and growth of akimotoite along $[001]_{En}$.

Each experimental sample within this study contains intracrystalline growth of high-pressure $(Mg,Fe)SiO_3$ polymorphs. While nano-fluid inclusions within our starting material are likely to have resulted in polycrystalline akimotoite rods parallel to $[001]_{En}$, crystallographic orientations of bridgmanite lamellae and other multi-phase intracrystalline growth features are not consistent with nucleation along $[001]_{En}$. This is an indication that multiple intracrystalline nucleation mechanisms occurred within our experimental samples, some of which do not appear to be dependent upon the presence of inclusions within the starting material. Future studies should fully explore the range of intracrystalline transformation mechanism active within natural San Carlos enstatite.

3.5.5 Implications for Enstatite within the Mantle

Within our experiments, direct transformation of natural Al- and Fe-bearing enstatite to high-pressure polymorphs occurs at conditions as low as 18.5 GPa and 1200°C. This is much lower than 21 GPa and 1550°C observed in experiments using end

member $MgSiO_3$ (Hogrefe et al., 1994). While kinetic factors may inhibit transformation of enstatite to akimotoite in colder slabs, we are unable to constrain the lower limit of kinetic boundaries for observable reactions in the transformation of natural enstatite to akimotoite because our lowest pressure and temperature experiments contain akimotoite. Future solid-state high-pressure experiments are necessary to further constrain pressure and temperature limits of observable reaction for each of the three $MgSiO_3$ polymorphs.

At low temperatures within subducting slabs, kinetic factors inhibit both (1) the dissolution of pyroxene into majorite garnet and (2) the breakdown of enstatite into Mg_2SiO_4 and SiO_2 phases (Hogrefe et al., 1994; Nishi et al., 2008). Recent studies suggest that limited diffusion of pyroxene components within subducting slabs enables enstatite to remain metastable to the base of the MTZ, with significant implications for buoyancy and stagnation of slabs (Nishi et al., 2013; Agrusta et al., 2014; Van Mierlo et al., 2014; King et al., 2015). The metastable boundaries for $MgSiO_3$ polymorphs show that as temperature decreases, majorite becomes increasingly unstable relative to akimotoite and bridgmanite at MTZ conditions (Figure 3.13). Therefore, direct transformation of metastable enstatite to metastable akimotoite is the most energetically favorable polymorphic reaction within cold subducting lithosphere. This reaction will occur at shallower depths and lower temperatures than the enstatite to majorite reaction that is currently used in thermo-kinetic subduction models. Further studies on the reaction rates of the enstatite-akimotoite transformation are necessary to provide quantitative kinetic data to constrain future thermo-kinetic and geodynamic models involving metastable enstatite.

The rapid transformation of metastable olivine has been suggested as a potential nucleation mechanism for deep focus earthquakes (Kirby et al., 1996; Frohlich 2006; Houston 2007). However, intracrystalline transformation mechanisms (Kerschhofer et al., 2000; Mosenfelder et al., 2001) and the presence of nominal amounts of H_2O (Diedrich et al., 2009; Du Frane et al,. 2013) within olivine enhance transformation rates and limit the metastable olivine wedge to a maximum depth of 550 km. Transformational faulting caused by the metastable transformation of enstatite to akimotoite has been proposed as a potential cause for the deepest earthquakes (Kirby et al., 1996; Frohlich 2006; Houston 2007), and enstatite is thought to remain metastable to greater depths than olivine due to the limited reactivity in experiments using end member $MgSiO_3$ (Hogrefe et al., 1994). Our results show that natural San Carlos enstatite produces abundant intracrystalline growth of high-pressure phases. If intracrystalline nucleation within enstatite is active in subducting slabs, then transformation of metastable enstatite to high-pressure phases is likely to be complete a much shallower depths than previously estimated. Additionally, natural enstatite grains contain crystallographic defects and trace amounts of H_2O that can enhance nucleation and growth rates. Our experiments show that a combination of these factors will increase reactivity in natural enstatite relative to annealed synthetic $MgSiO_3$. Therefore, the maximum depth of metastable enstatite within subducting slabs is likely to be much shallower than previous studies suggest, and transformational faulting of enstatite to akimotoite is unlikely to be the cause of the deepest earthquakes within the MTZ.

3.6 Conclusions

Metastable enstatite is thought to survive to greater depths within cold interior of subducting slabs than metastable olivine. This interpretation is based on kinetic data showing that the diffusion controlled reactions of enstatite to majorite garnet and enstatite to wadsleyite or ringwoodite plus stishovite will be inhibited within the cold interior of subducting slabs (Hogrefe et al., 1994; Nishi et al., 2008; Van Mierlo et al., 2013). We show that direct polymorphic transformation of enstatite to akimotoite is the preferred polymorphic reaction within solid-state transformation experiments using natural San Carlos enstatite. Additionally, metastable polymorphic reactions occur more readily in natural samples than in end-member $MgSiO_3$. The H_2O content of San Carlos enstatite represents a minimum of the range for mantle-derived orthopyroxenes; therefore, we expect that greater concentrations of H_2O within enstatite in subducting slabs would further increase transformation rates. Our experiments resulted in abundant intracrystalline transformation of high-pressure phases. If present within subducting slabs, these additional nucleation sites will increase bulk transformation rates of enstatite within the mantle. Therefore, given the low H_2O content of our starting material, the presence of abundant intracrystalline transformation of high-pressure phases, and an increased range of observable reactions our samples, it is likely that metastable natural enstatite within the cold interior of subducting slabs will transform to high-pressure phases at much shallower depths than previously thought.

These findings have important implications for the behavior of subducting slabs within the MTZ. If natural enstatite is more reactive within the interior of cold subducting slabs than previous studies indicate, then transformational faulting caused by rapid

transformation of metastable enstatite to akimotoite is less likely to cause the deepest recorded earthquakes. Additionally, enhanced reactivity of natural enstatite will have significant effects on thermo-kinetic and geodynamic models of the behavior of subducting slabs within the MTZ. Future studies examining the effects of negative density contrast and buoyancy caused by metastable enstatite should account for these results to refine models of slab behavior, such as the stagnation of slabs at the base of MTZ.

CHAPTER 4

INTRACRYSTALLINE TRANSFORMATION OF HIGH-CLINOENSTATITE AT MANTLE TRANSITION ZONE CONDITIONS: IMPLICATIONS FOR RATES, CRYSTALLOGRAPHIC PREFERRED ORIENTATIONS AND DEEP FOCUS EARTHQUAKES

4.1. Introduction

Enstatite $(Mg,Fe)SiO_3$ is one of the most abundant minerals in the upper mantle, and it is estimated to comprise 18-25% of subducting lithosphere (Ringwood 1982; Irifune and Ringwood 1993; Hogrefe et al., 1994). At ambient mantle conditions, enstatite will react into majoritic garnet via solid solution by approximately 460 km depth (Akaogi and Akimoto 1977; Irifune and Ringwood 1987; Ringwood 1991). However, this diffusion-controlled reaction is one of the slowest processes in the mantle and is kinetically limited within the cold interior of subducting slabs (Nishi et al., 2008; van Meirlo et al., 2013). Additionally, slow chemical diffusion within the interior of cold slabs is expected to hinder the isochemical transformation of enstatite to wadsleyite plus stishovite and favor the polymorphic transformation to akimotoite (ilmenite structure) (Hogrefe et al., 1994). Kinetic inhibition of diffusion-dependent equilibrium reactions in the $(Mg,Fe)SiO_3$ system have led to the interpretation that over-pressured metastable enstatite can survive to the base of the mantle transition zone (MTZ) (Hogrefe et al., 1994).

To study the behavior of metastable enstatite within the MTZ, it is first necessary to understand phase relations within the $(Mg,Fe)SiO_3$ system at upper mantle conditions. $(Mg,Fe)SiO_3$ that crystallizes from melt is typically orthoenstatite (OEN) with space

group *Pbca*. Depending on composition and pressure-temperature path, descending OEN within subducting slabs will transform to a monoclinic structure of either a *C2/c* or $P2_1/c$ space group (HCEN or HCEN2, respectively) between 7 and 16 GPa (Angel et al., 1992; Shinmei et al., 1999; Ulmer and Stalder 2001; Zhang et al., 2012, 2013). The transformation of ortho- to clinoenstatite has been shown to cause polysynthetic twinning parallel to (100) (Buseck and Iijima 1975; Milke et al., 2007). Stacking disorder has also been reported along the (100) plane of $FeSiO_3$ during ortho- to clinoferrosilite transitions at 4.2 GPa (Hugh-Jones et al., 1996), and within the Tenham meteorite which showed a streaking of diffraction spots parallel to a^* (Tomioka and Fujino 1999).

Planar defects within crystals may impact rheology and phase transformations within subducting slabs. For example, within experiments applying varying orientations of maximum compressive stress to polysynthetically twinned TiAl crystals, the resulting shear deformation is preferentially aligned parallel to pre-existing twin boundaries (Fujiwara et al., 1990). Additionally, stacking faults within single crystals of olivine can serve as heterogeneous nucleation sites for coherent intracrystalline growth of high-pressure phases (Kerschhofer et al, 1996; Dupas-Bruzek et al., 1998). A reduction of grain size from intracrystalline transformation may promote rheological weakening within the slab (Kerschhofer et al., 2000), thus providing potential pre-existing zones of weakness necessary for the cascading shear failure model of deep focus earthquakes (Karato et al., 2001; Chen and Wen, 2015).

Within pyroxenes, topotaxial growth of akimotoite within clinoenstatite grains has been reported in shock-melt veins within the Tenham L6 chondrite (Tomioka and Fujino 1997, 1999), and a shear-induced mechanism for topotaxial transformation of

clinopyroxene to ilmenite structure was observed using analog $FeGeO_3$ systems (Hattori et al., 2001). These findings led to the proposal of a diffusionless, shear-induced mechanism for the topotaxial transformation of metastable clinoenstatite to akimotoite (Tomioka 2007). In this mechanism, stacking faults along $(100)_{cEn}$ adjust close-packed oxygen layers from cubic to hexagonal close-packed arrangement and a series of four partial dislocations result in topotaxial transformation of enstatite to akimotoite with $(100)_{cEn} \parallel (001)_{aki}$ and $[011]_{cEn} \parallel [110]_{aki}$ (Tomioka 2007).

Mechanisms for the transformation of metastable clinoenstatite to akimotoite may be related to several large-scale geophysical observations within the MTZ. First, transformational faulting during the reaction of metastable clinoenstatite to akimotoite has been suggested as a potential cause of the deepest recorded earthquakes (Hogrefe et al., 1994; Kirby et al., 1996; Frohlich 2006; Tomioka 2007), as well as the increase in global seismicity observed below 550 km (Persh and Houston 2004). When included in thermo-kinetic models of slab behavior, intracrystalline transformation mechanisms increase bulk transformation rates and thus reduce the depths to which metastable phases can survive within subducting lithosphere (Mosenfelder et al., 2001). Second, it is possible for minerals within the mantle to inherit crystallographic preferred orientation (CPO) from lower pressure phases (Dobson et al., 2013). Akimotoite is the most seismically anisotropic mineral within the MTZ (Zhou et al., 2014) and CPO within akimotoite may be seismically detectable (Shiraishi et al., 2008). Topotaxial growth of akimotoite from metastable clinoenstatite would provide a mechanism for the inheritance of CPO from previously deformed clinoenstatite, which would limit the effectiveness of seismic anisotropy as an indicator of slab flow and deformation at the base of the MTZ.

Despite its potential importance to processes occurring within subducting slabs within the MTZ, to date there have been no experimental studies on the mechanisms and kinetics of these reactions using natural, single crystals of enstatite. In a contemporaneous study, we report that natural enstatite is much more reactive than pure $MgSiO_3$ within solid-state transformation experiments (Chapter 3). In this study, we perform a series of multi-anvil experiments using single crystals of natural San Carlos enstatite to explore transformation mechanisms within the $(Mg,Fe)SiO_3$ system at MTZ conditions. Polysynthetic twinning of clinoenstatite is present within all recovered experimental samples and $(100)_{cEn}$ twin boundaries appear to serve as nucleation sites for both coherent and incoherent growth of multiple high-pressure phases. We suggest that growth of high-pressure phases along polysynthetic twin boundaries within clinoenstatite favors a cascading failure of shear instabilities (Karato et al., 2001; Chen and Wen, 2015) rather than transformational faulting of enstatite (Hogrefe et al., 1994; Kirby et al., 1996; Frohlich 2006; Tomioka 2007) for the generation of deep-focus earthquakes. Additionally, topotaxial relationships in high-pressure reactions from clinoenstatite may provide a means for the inheritance of CPO in the lower MTZ.

4.2 Experimental and Analytical Methodology

We investigate the behavior of natural enstatite at MTZ conditions by performing a series of high-pressure experiments using natural Al- and Fe-bearing San Carlos orthoenstatite (*Pbca*) as starting material. Experimentation using larger (~1mm) natural crystals is likely to provide a more accurate representation of processes occurring within subducting slabs as they pass through the MTZ. Crystals from San Carlos xenoliths have

been used as starting material for kinetic experiments in the $(Mg,Fe)_2SiO_4$ system (Kerschhofer et al., 1996, 1998, 2000; Liu et al., 1998; Mosenfelder et al., 2000; Diedrich et al., 2009; Du Frane et al., 2013) because they contain very little H_2O (> 4 ppm for olivine; see Li et al., 2008), and they have similar compositions as lherzolite within subducting lithosphere. San Carlos orthopyroxene has a composition of $(Ca_{0.05}, Cr_{0.03,}$ $Fe_{0.19,}$ $Mg_{1.66}$, $Al_{0.07})(Al_{0.08}, Si_{1.92})O_6$ with an Mg/(Mg+Fe) ratio of 0.93 to 0.89, 3-5 wt% Al_2O_3 (Table 3.1; Frey and Prinz, 1978; Reynard et al., 2010; Zhang et al., 2012, 2014), and 53 to 83 ppm H_2O (Li et al., 2008). Experiments were performed using the 1100-ton multi-anvil press at Arizona State University, the COMPRESS 10/5 multi-anvil assembly (Figure 3.3a; Leinenweber et al., 2012), and custom designed silver (Ag) capsules (Figure 3.3b). We compressed experimental samples to 18.5 GPa and 21 GPa and heated samples to 1200, 1300 or 1400°C at a rate of 100°C per minute. The reader is referred to Chapter 3 for additional details about sample preparation, capsule and assembly design, experimental errors, and sample recovery.

Recovered experimental samples were analyzed by optical microscopy, Raman spectroscopy, scanning electron microscopy (SEM), and transmission electron microscopy (TEM) at Arizona State University in the LeRoy Eyring Center for Solid State Science (LE-CSS). Raman spectroscopy was performed using a Coherent Sapphire SF laser with a wavelength of 532 nm and a 1200 gr/mm diffraction grating. The laser has a spatial sampling resolution of approximately 1 μm and was focused onto the sample using an 100X objective with a focal length of 0.2 mm. We sampled low pressure phases using a laser power of 12 mW; however, we generally lowered laser power to 1.3 to 6

mW and increased sample collection times to 100s of seconds when sampling unstable high-pressure phases in recovered experimental samples.

Scanning electron microscopy (SEM) was performed using an FEI XL30 Environmental SEM with a Field Emission Gun (FEG) system at the LE-CSSS. To prevent charging, a carbon film was applied to samples using an evaporation carbon coater. Samples were investigated primarily using backscatter electron (BSE) imaging. Imaging was performed using an acceleration voltage of 15 to 20 kV, spot size of 5.0, and working distance of 10 mm. At these settings, the instrument has a beam current of approximately 2.26 to 2.39 nA and a probe diameter of approximately 5 to 6 nm. Energy dispersive X-ray spectroscopy (EDS) was used for chemical analyses of starting material and high-pressure phases using an EDAX SiLi detector. Absorption and fluorescence effects for this system are corrected using a *ZAF* model. Process times for EDS analyses varied but were generally 4 to 10 μs to allow for at least 600 counts per second and a dead time of approximately 30%. Collection times for EDS analyses ranged from 10 seconds to over one minute, depending on the stability of the resulting spectra.

Transmission electron microscopy (TEM) was performed at the LE-CSSS using an FEI CM200-FEG. To image beam-sensitive microstructures within our starting material, we prepared TEM samples using two separate techniques; (1) a focused-ion beam (FIB) lift-out technique with an FEI Nova200 NanoLab using an acceleration voltage of 30 keV and beam current of 0.1 to 20 nA, and (2) sample thinning using a Gatan dimple grinder and a Gatan Precision Ion Milling System (PIPS) with an Ar ion beam angle of 7° and an accelerating voltage of 6 keV. We investigated microstructures using diffraction contrast and high-resolution TEM imaging techniques. Mineral

structures were identified with selected area electron diffraction (SAED). We performed chemical analysis on TEM samples by EDS using an EDAX SiLi detector, with quantitative data processing performed using the Emispec Vision system and theoretical K-factors

4.3 Experimental Results

4.3.1 Transformation of Pyroxene Cores

We use Raman spectroscopy to distinguish OEN from LCEN and constrain the reaction sequence that occurred within the pyroxene core of experimental samples. LCEN ($P2_1/c$) is distinguished from OEN (*Pbca*) by the absence of Raman peaks at 83 cm^{-1} and 443 cm^{-1}, the addition of peaks at 115 cm^{-1} and 369 cm^{-1}, and the shifting of the peak at 237 cm^{-1} to 242 cm^{-1} (Ulmer and Stalder, 2001; Lin 2004; Reynard et al., 2008). The Raman data show that San Carlos enstaite starting material is OEN (*Pbca*), and recovered experimental samples are LCEN ($P2_1/c$) (Figure 4.1). This is corroborated by TEM analysis and selected area electron diffraction data for the pyroxene cores of recovered experimental samples. When viewed along the [010] zone axis, experimental samples have a β^* angle that is approximately 71°, which is indicative of a clinopyroxene phase. The pattern viewed down zone [010] also contains $h + k$ equals odd reflections, which is consistent with the primitive lattice of LCEN ($P2_1/c$). Therefore, we conclude that the pyroxene core within recovered exerimental samples is LCEN ($P2_1/c$) phase.

Each recovered experimental sample contains abundant polysynthetic twinning that is not present within OEN starting material. The twinning is clearly discernable using optical microscopy with cross-polarized light (Figure 4.2a). The transformation of ortho-

to clinopyroxene results in a halving of the enstatite unit cell along the *a** direction. The loss of symmetry from ortho- to clinopyroxene allows the product phase to have two potential orientations that are related by reflection symmetry along the (100) plane (Figure 4.2b). TEM analysis of FIB sections taken from the transformed pyroxene core of recovered experimental samples confirms that abundant clinoenstatite twins are related by reflection along the (100) plane (Figure 4.2c). Since these twinning domains are easily identified in optical microscopy, they provide a useful reference to compare crystallographic relationships between high-pressure transformation features and the pyroxene host.

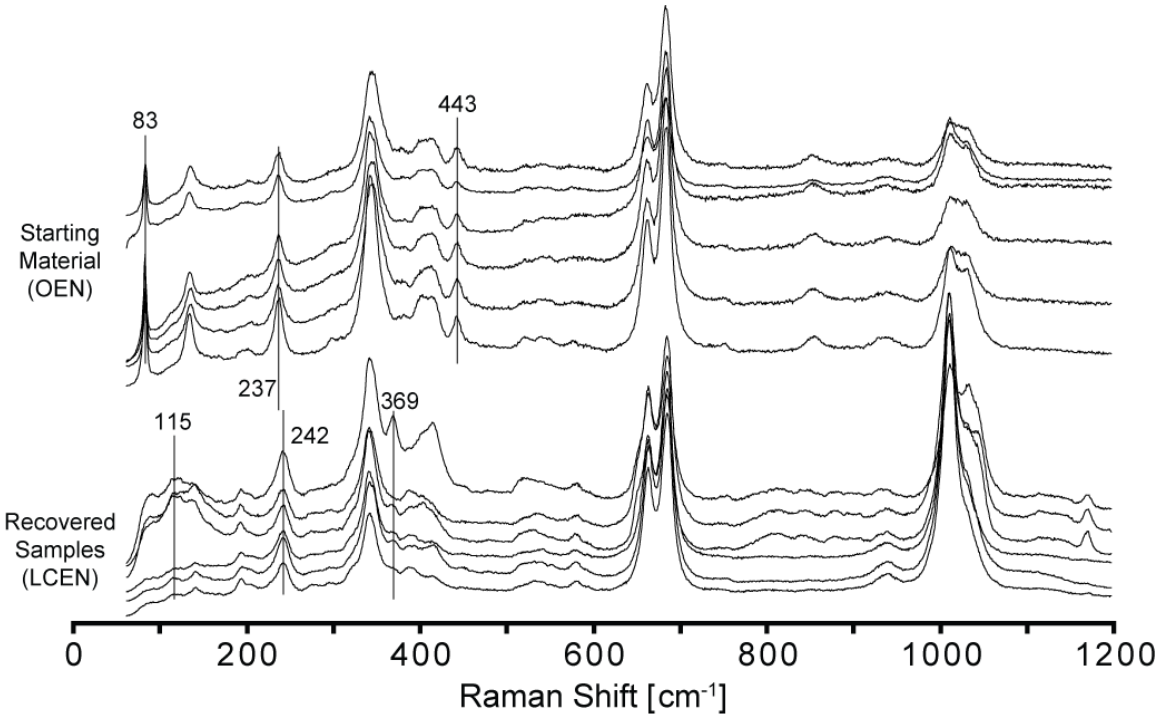

Figure 4.1. Raman spectra for six unoriented crystals of San Carlos orthoenstaite starting material (top) and unoriented experimentally transformed clinoenstaite cores (bottom). Vertical lines represent peaks that are not present in LCEN (83 cm^{-1}, 443 cm^{-1}), peaks that are not present in OEN but are present in LCEN (115 cm^{-1}, 369 cm^{-1}), and a peak that is shifted during the transformation of OEN to LCEN (237 to 242 cm^{-1}).

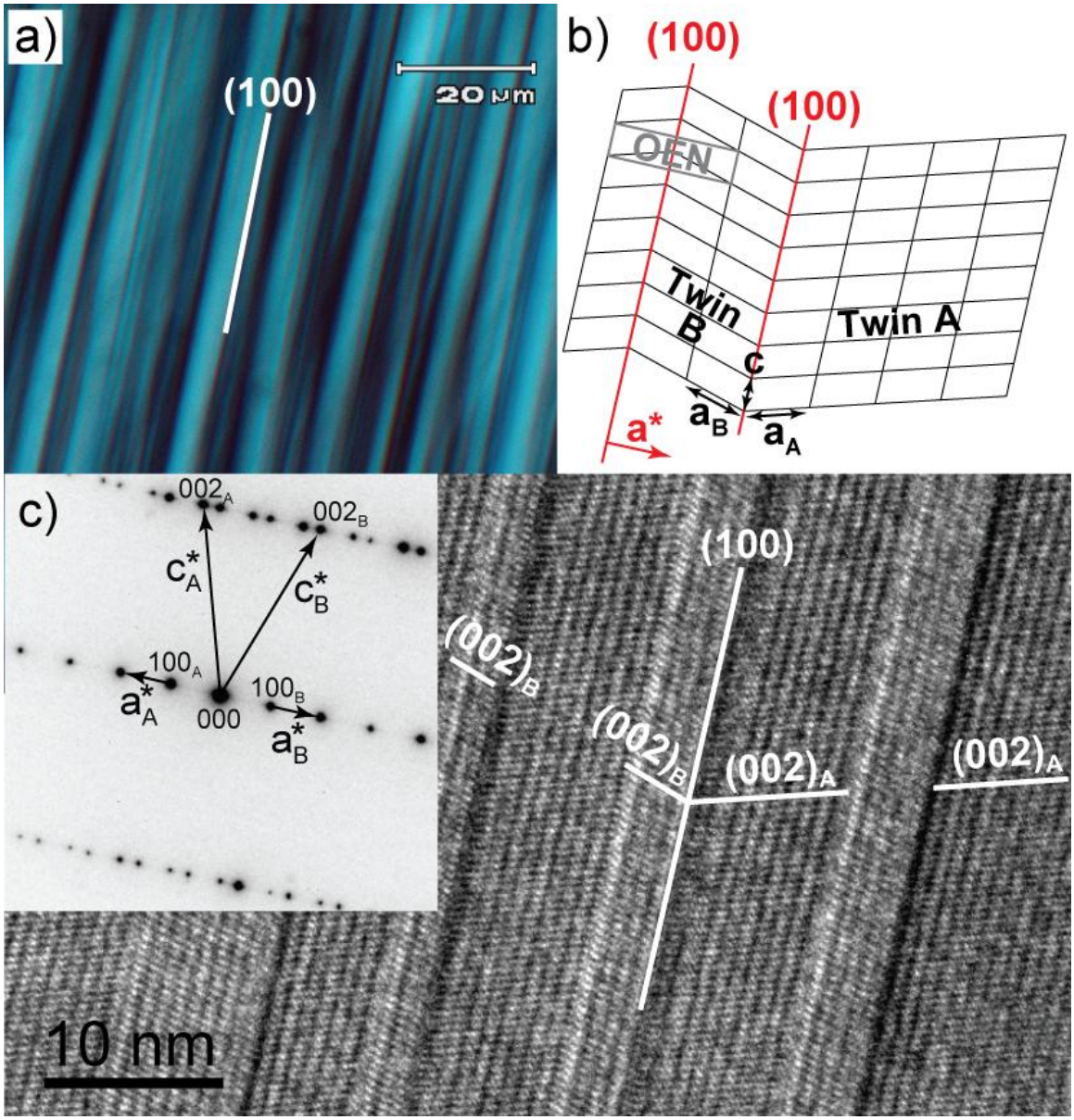

Figure 4.2. (a) Cross-polarized transmitted light optical micrograph of transformed low-clinoenstatite (LCEN) core within sample BB1158. (b) Schematic diagram of reflection twins along (100) within LCEN cores of recovered experimental samples. The twins occur when orthoenstatite (OEN) starting material (grey rectangle) halves its length along the a* direction during transformation to LCEN (black quadrilaterals) giving the product phase one of two orientation variants (A or B). (c) Transmission electron microscopy of twinned LCEN within sample BB1110. Electron diffraction (inset) viewed along $[010]_{LCEN}$ confirms a refection twin on $(100)_{LCEN}$. Brightfield HRTEM image of sample BB1110 displaying repeated twin domains with alternating orinetations of (002) lattice fringes.

4.3.2 Topotaxial Growth of High-Pressure Phases

Within the sample transformed at 21 GPa and 1400°C, akimotoite lamellae are present within clinoenstatite (cEn) core (Figure 4.3). We cut a FIB section of the area and determined the crystallographic relationship between the akimotoite lamellae and the clinoenstatite host using high resolution TEM imaging and selected area electron diffraction. Diffraction patterns of the lamellae and host are indexed as two clinoenstatite patterns viewed down the $[011]_{cEn}$ and $[0\overline{1}\overline{1}]_{cEn}$ zone axes and two akimotoite patterns viewed along $[110]_{aki}$, and $[\overline{1}\overline{1}0]_{aki}$. The patterns for each mineral are related by reflection twinning along the $(100)_{cEn}$ and $(001)_{aki}$ planes, and a^*_{cEn} parallels c^*_{aki} in all patterns (Figure 4.3b). Twining is ubiquitous within the cEn host material of recovered samples; however, lamellae are most commonly slabs of untwinned akimotoite. High resolution transmission electorn micrographs show that akimotote forms as tabular lamellae that grow out from cEn twin boundaries (Figure 4.3c).

In several locations, wadsleyite and stishovite grains up to 20 by 100 nm occur along the interface between twinned akimotoite and cEn. Electron diffraction patterns viewed down zones $[101]_{wds}$ and $[101]_{st}$ show that cEn, akimotite, wadsleyite, and stishovite each share topotaxial relationships with one another, with vectors $[10\bar{1}]^*_{wds}$, $[010]^*_{st}$, a^*_{cEn}, and c^*_{aki} all in parallel (Figure 4.3d). These vectors are perpendicular to the close packed oxygen layers for each mineral; therefore, close packed oxygen layers in cEn and each product phase are parallel and possibly continuous (Figure 4.4). The orientations and morphology of high-pressure product phases are consistent with coherent nucleation and growth along the $(100)_{cEn}$ twin boundaries.

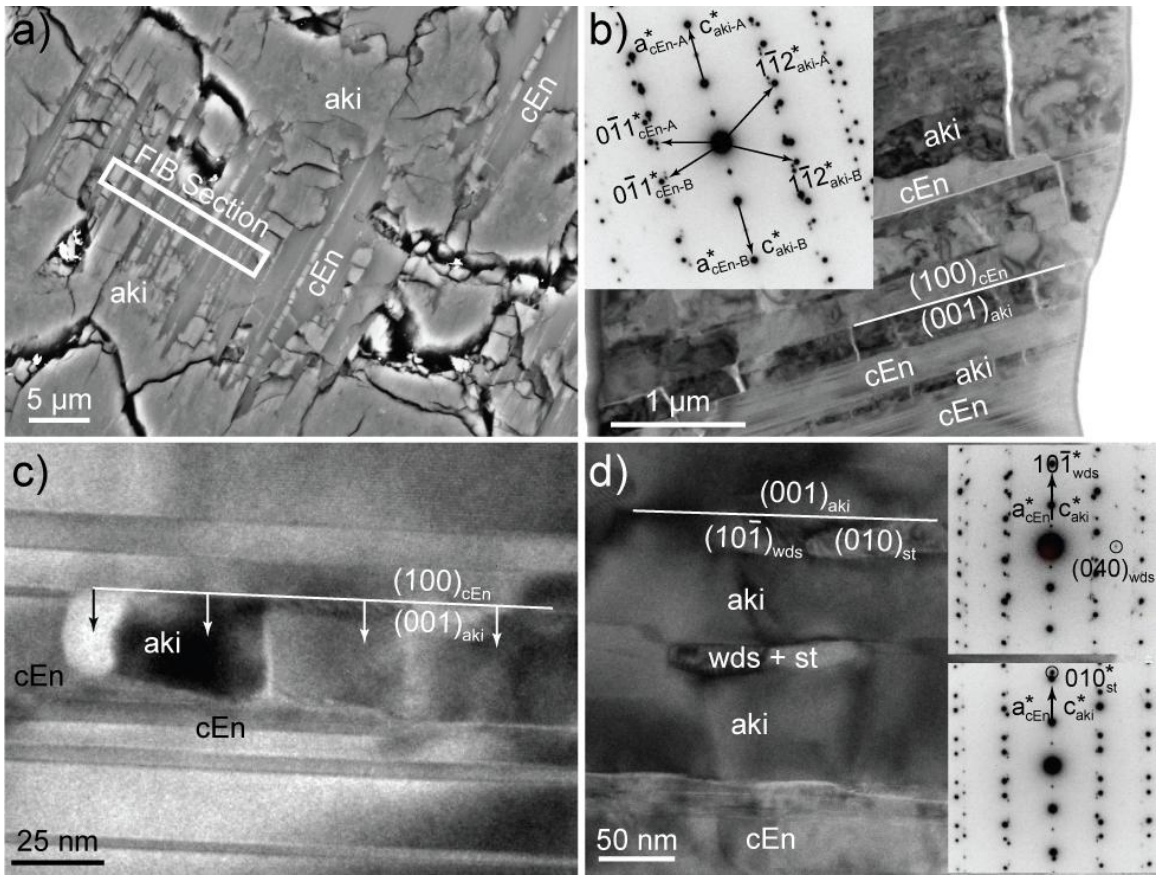

Figure 4.3. (a) FESEM BSE micrograph of akimotoite (aki) lamellae within clinoenstiate (cEn) core of sample BB1110 (21 GPa, 1400°C). Area of FIB section for TEM analysis outlined in white. (b) Transmission electron micrograph of alternating aki and cEn lamellae. Selected area electron diffraction pattern (inset to b) shows twins of both cEn and aki viewed down zone axes $[011]_{cEn}$, $[0\overline{11}]_{cEn}$, $[110]_{aki}$, and $[\overline{110}]_{aki}$ with a^*_{cEn} parallel to c^*_{aki}. (c) Coherent nucleation of aki lamellae along a continuous, preexisting twin boundary within cEn host. Voids along aki lamellae form by differential expansion of during sample quench. (d) Transmision electron micrograph showing growth of wadsleyite (wds) and stishovite (st) along twin boundaries within akimotoite. Inset electron diffraction patterns show topotaxial relationships for all four phases, with $[10\bar{1}]^*_{wds}$ and $[010]^*_{st}$ parallel to a^*_{cEn} and c^*_{aki}. Diffraction patterns are viewed down $[101]_{wds}$, $[101]_{st}$, and the same zone axes of cEn and aki as in (b).

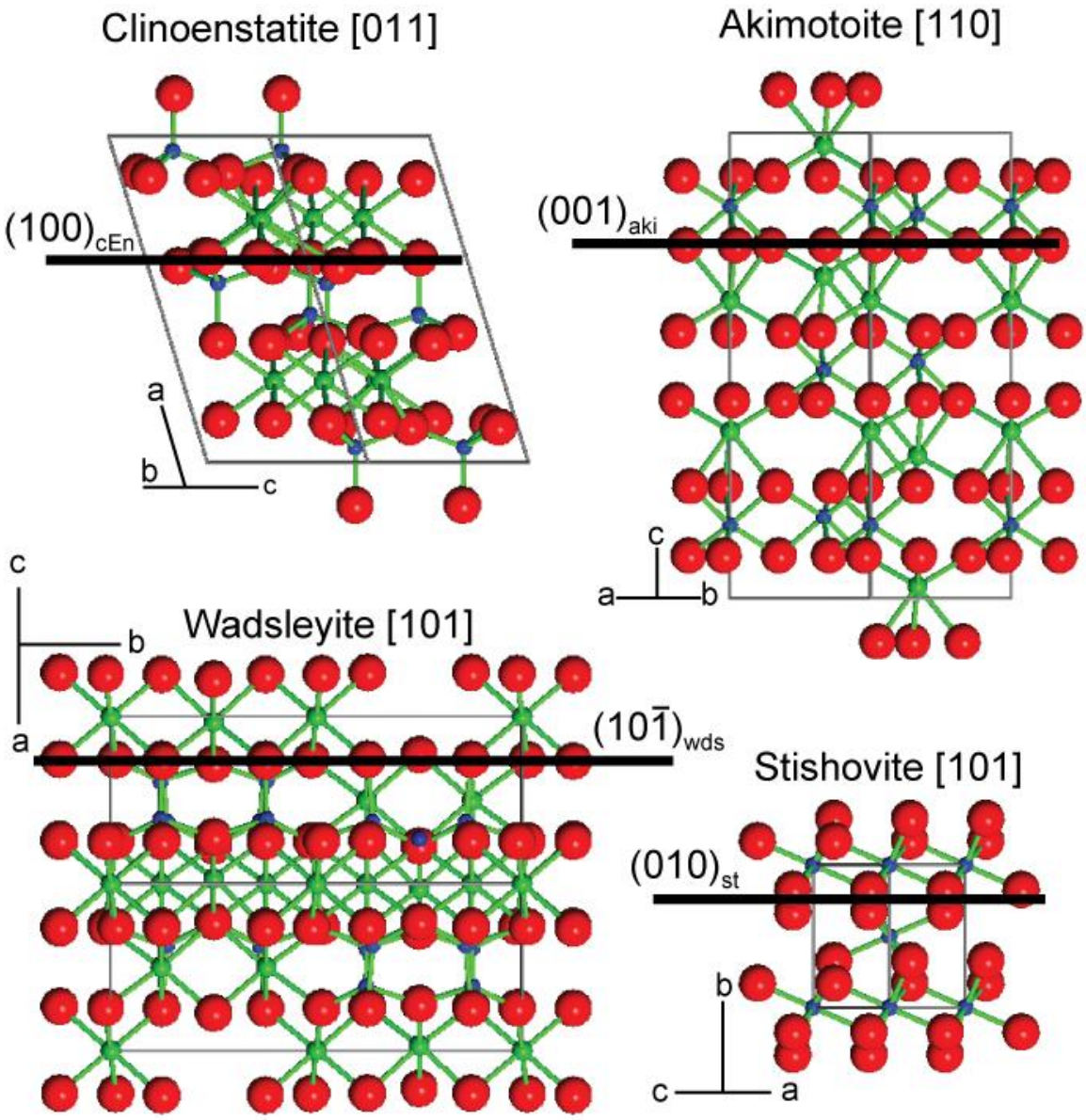

Figure 4.4. Ball and stick crystal models illustrating the preservation of close-packed oxygen (red spheres) layers during topotaxial transformation of clinoenstatite (cEn) to akimotoite (aki), wadsleyite (wds), and stishovite (st). Models viewed down zone axes $[011]_{cEn}$, $[110]_{aki}$, $[101]_{wds}$, and $[101]_{st}$, which are the same as the diffraction patterns in Figure 4.3. Parallel planes of close packed oxygen layers are $(100)_{cEn}$, $(001)_{aki}$, $(10\bar{1})_{wds}$, and $(010)_{st}$. Preservation of cation layers in cations Mg (green spheres) and Si (blue spheres) also occur in these orientations.

4.3.3 Direct Transformation of Enstatite to Bridgmanite

$(Mg,Fe)SiO_3$ polymorphs bridgmanite, akimotoite and majorite are all stable relative to HCEN starting material above 20 GPa and 800°C (Figure 3.13). Each of our recovered experimental samples transformed at 21 GPa and 1300°C to 1400°C contains a high-contrast phase in reflected light microscopy and SEM BSE images (Figure 4.5a). This phase occurs (1) as lamellae within the pyroxene core and (2) as part of a polycrystalline mixture with akimotoite at the outer edge of grain boundary reaction rims. Raman spectra of the phase contains characteristic broad peaks at 732 cm^{-1} and 897 cm^{-1}, which is consistent with published spectra of $MgSiO_3$ perovskite (Bolfan-Cassanova et al., 2003); however, lower modes typical for bridgmanite were not present (Figure 4.5b). Additionally, electron diffraction patterns collected during TEM analysis (Figure 4.5c) show that the high-contrast lamellae is amorphous, and EDS data confirms that the phase is compositionally identical to the untransformed enstatite core. Based on its beam sensitivity, chemical composition, and Raman data, we conclude that the bright high-pressure phase is vitrified bridgmanite.

When viewed using transmitted light microscopy, the lamellae are oriented parallel to $(100)_{cEn}$ twin boundaries. The lamellae can occur in isolation from other high-pressure phases, but they are most commonly located at the ends of 5 to 10 μm wide, linear-trending bands of akimotoite (Figure 4.5a) or at the fringes of nodular-shaped majorite and akimotoite growth that are approximately 30 to 50 μm in size (Figure 3.11). To further analyze high-resolution structure and composition of these lamellae, we extracted a FIB section of a lamellae within Sample BB1110 (21 GPa, 1400°C).

Brightfield TEM images show that the interface between the lamellae and the cEn host is sub-parallel to $(100)_{cEn}$ twin boundaries (Figure 4.5c).

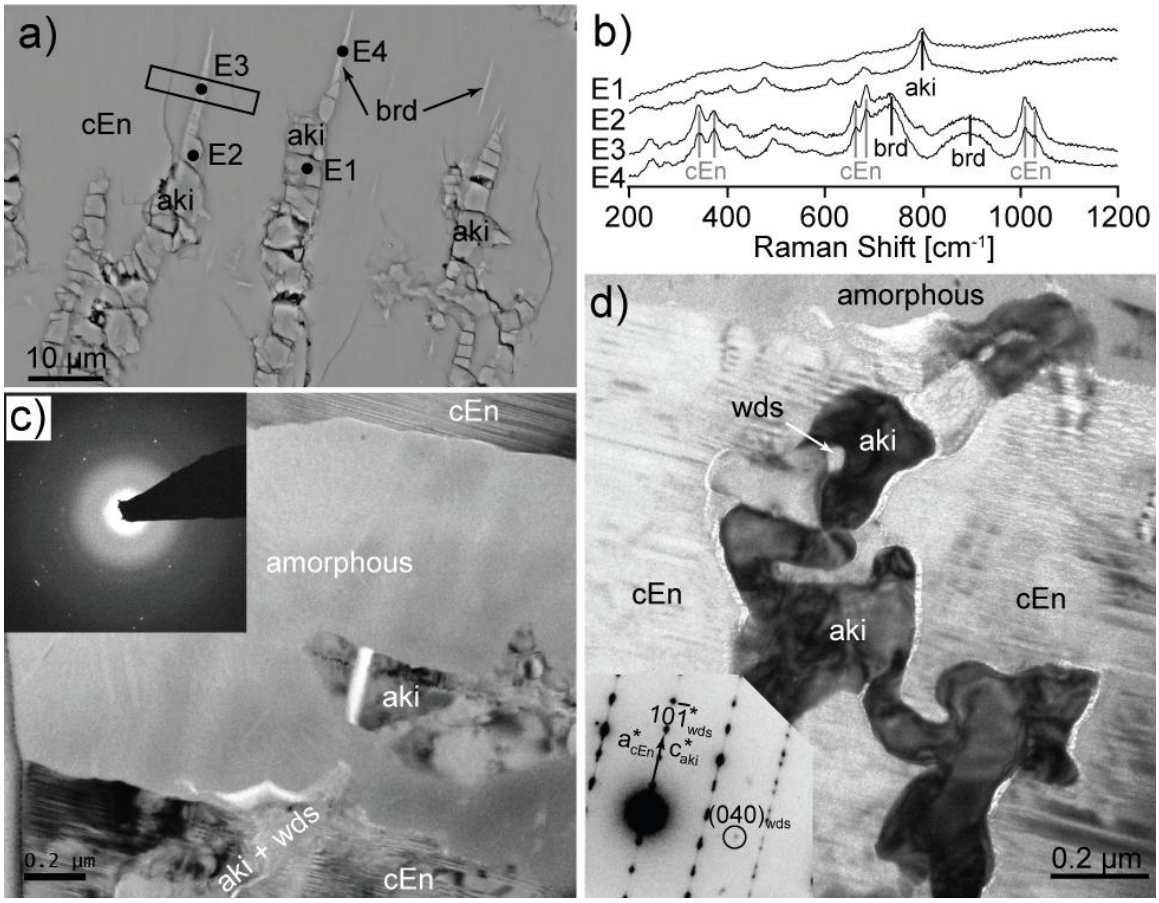

Figure 4.5. (a) FESEM BSE micrograph of amorphous bridgmanite (brd) lamellae extending from akimotoite (aki) inclusions in the clinoenstiate (cEn) core of sample BB1110 (21 GPa, 1400°C). Area of FIB section for TEM analysis outlined in black. (b) Raman spectra for sample points E1-E4 show characteristic 799 cm^{-1} peak for akimotoite and broad amorphous bridgmanite peaks at peaks at 732 cm^{-1} and 897 cm^{-1}. (c) Transmission electron micrograph of amorphous bridgmanite lamellae that is sub-parallel to (100) twin planes in cEn. Selected area electron diffraction pattern (inset to c) shows amorphous phase with diffuse rings of diffraction intensity associated with reflections from randomly oriented crystalline material. High pressure phases occur within the lamellae and at the interface between lamellae and host cEn. (d) Aki and wadsleyite (wds) grains at the margin of interface between the amorphous lamellae and cEn.

4.3.4 Lamellae as Nucleation Sites for High-Pressure Crystallites

In addition to topotaxial growth of high-pressure phases along $(100)_{cEn}$, TEM data from the sample transformed at 21 GPa and 1300°C to 1400°C shows that lamellae can also provide nucleation sites for non-lamellar growth of high-pressure crystallites 10 nm to 1 μm in size. Crystallites occur (1) along the grain boundaries of bridmanite (Figure 4.5c,d) or akimotoite lamellae (Figure 4.6a,b), (2) within the interior of akimotoite lamellae (Figure 4.6b), and (3) within the interior of amorphous bridgmanite lamellae (Figure 4.5c,d). Crystallites range in habit from anheadral to euhedral, and euhedral to subhedral grains appear to share a similar crystallographic orientation. While the crystallites were too small and beam sensitive to perform a detailed survey of their compositions and crystallographic orientations, *d*-spacings within several selected area electron diffraction patterns were consistent with akimotoite that shared no clear topotaxial relationship with neighboring crystals. Crystallites do not occur within the interior of the host enstatite grains, nor do they occur along enstatite-enstatite twin boundaries. This suggests that akimotoite crystallites via a secondary transformation mechanisms that first requres the presence of bridgmanite or akmotoite lamellae, such as incoherent nucleation on lamellae boundaries.

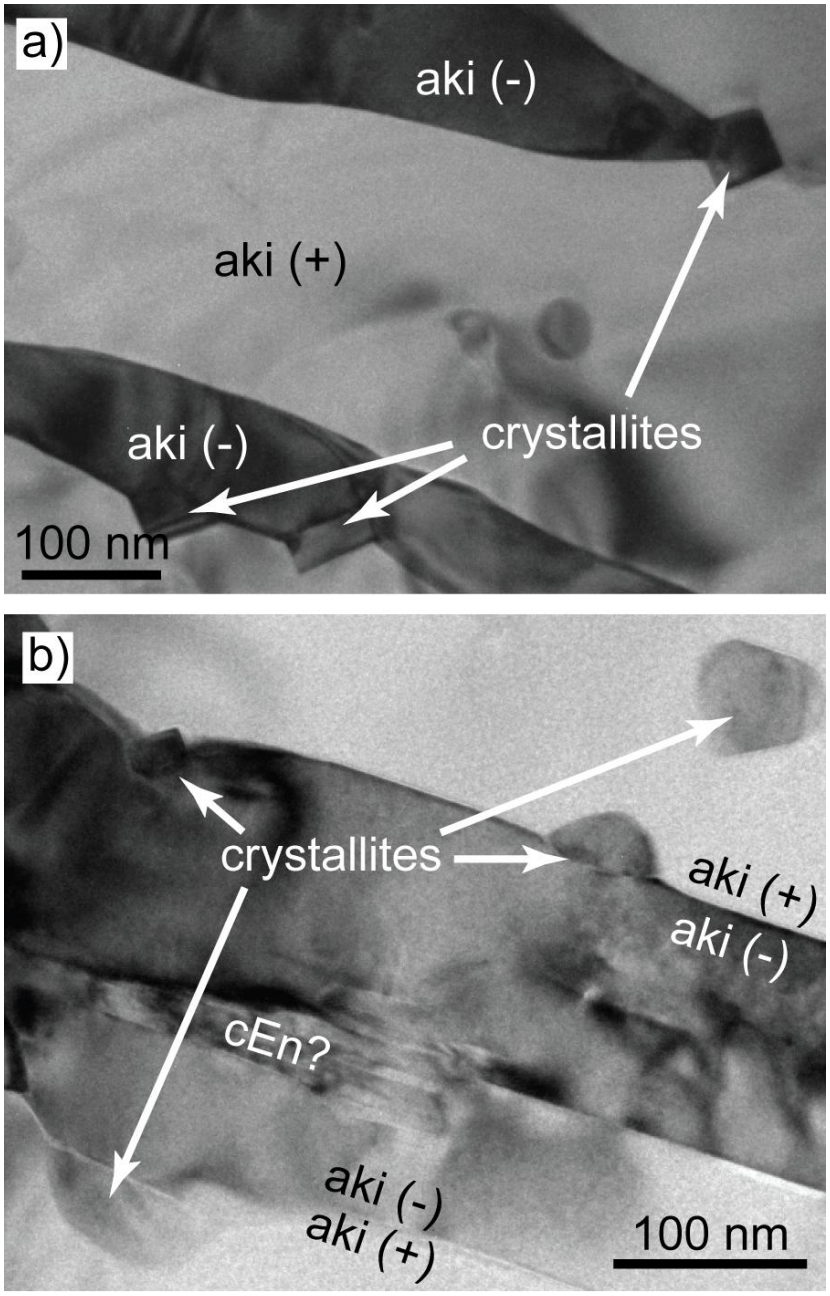

Figure 4.6. Transmission electron micrograph of high-pressure crystallites within sample BB1110 (21 GPa, 1400°C). Crystallites occur both along akimotote-akimotoite twin boundaries and within the interior of an akimotoite lamellae.

4.4 Discussion

4.4.1 Pyroxene Transformation Sequence

Magnesium-rich pyroxene undergoes a series of polymorphic reactions with increased pressure and temperature. The stabilility of these pyroxene phases relative to one another is dependent upon pressure-temperature path, composition, and kinetic factors. Raman spectroscopy shows that our San Carlos enstatite starting material is OEN (*Pbca*). During compression at room temperature, OEN (*Pbca*) transforms to HCEN2 ($P2_1/c$) between 12 to 16 GPa (Lin 2004; Zhang et al., 2013). This reaction is a first order phase transformation, and HCEN2 reverts to OEN upon quench (Lin 2004; Zhang et al., 2014). Because our experiments were compressed at room temperature to at least 18.5 GPa, it is likely that the samples were transformed to HCEN2 during compression. However, Raman spectroscopy and TEM analyses show that the pyroxene cores of our recovered experimental samples are LCEN ($P2_1/c$). The high-pressure and -temperature HCEN (*C2/c*) structure transforms to the LCEN ($P2_1/c$) structure upon quench (Angel et al., 1992; Ulmer and Stalder, 2001); therefore, the presence of LCEN ($P2_1/c$) cores within recovered experimental samples is indirect evidence that our samples transformed to HCEN (*C2/c*) during heating and then transformed to LCEN ($P2_1/c$) upon pressure quench. Therefore, we infer a recation sequence of OEN-HCEN2-HCEN-LCEN for the pyroxene cores in our experimental samples.

4.4.2 Mechanism for the Inheritance of Crystallographic Preferred Orientation

Topotaxial growth of akimotoite lamellae occurred within the sample transformed at 21 GPa and 1400°C. Our experiments were performed at near hydrostatic conditions;

therefore, the only likely differential stresses within our samples are from potential defects present within natural San Carlos enstatite starting material. While the crystallographic relationship $(100)_{cEn} \parallel (001)_{aki}$ and $[001]_{cEn} \parallel [010]_{aki}$ preserves close packed oxygen layering of clinoenstatite in akimotoite (Figure 4.4), the sample contains no evidence of stacking faults or disorder along $(100)_{cEn}$. Therefore, it is unlikely that it resulted from a martensitic-like shear transformation mechanism. Electron diffraction data show twinning within both cEn and akimotoite, indicating that akimotoite nucleated on both orientations of preexisting cEn twins. We conclude that the most likely transformation mechanism that produced topotaxial akimotoite lamellae was coherent heterogeneous nucleation along HCEN twin boundaries followed by coherent growth of akimotoite.

Tomioka (2007) proposed a diffusionless shear mechanism for the cEn-akimotoite transformation that involves shearing of the oxygen sublattice of HCEN through the formation of (100) stacking faults. This mechanism was based on the topotaxial relationship $(100)_{cEn} \parallel (001)_{aki}$ and $[001]_{cEn} \parallel [010]_{aki}$ observed within the Tenham meteorite (Tomioka and Fujino 1997). The orientation observed in the current study, with $(100)_{cEn} \parallel (001)_{aki}$ and $[011]_{cEn} \parallel [110]_{aki}$ (Figure 4.6), is that same as that was proposed by *Tomioka* (2007). Although a diffusionless mechanism may be favorable within a subducting slab where temperatures are low and differential stress is high, in this study the topotaxial relationship was produced at low to moderate differential stress and high temperature. Further, the sample also contains topotaxial growth of wadsleyite and stishovite, which requires long range diffusion of cations. This indicates that the high-

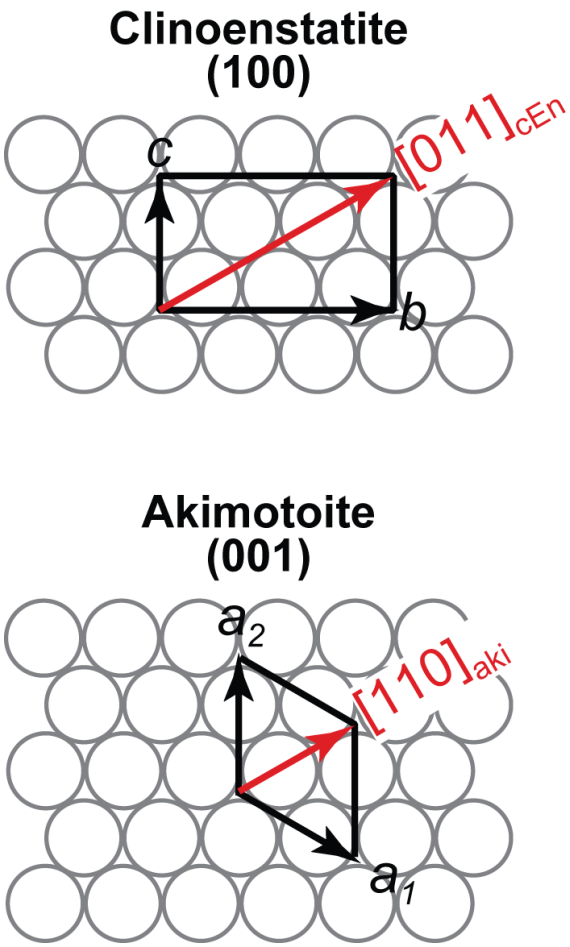

Figure 4.7. Relationship between crytallographic orientations of clinoenstatite and akimotoite as proposed by Tomioka (2007) (black) and as observed in experimental samples from the current study (red). The hexagonal array of circles represents the close-packed oxygen layers of clinoenstatite and akimotoite.

pressure phases with a topotaxial relationship to enstatite can be formed without large differential stresses or shearing.

Minerals within the mantle may inherit CPO from lower pressure phases such as olivine or pyroxene (Dobson et al., 2013). This is especially important for akimotoite because it is the most seismically anisotropic mineral within the MTZ (Zhou et al., 2013), and there is evidence for seismically detectable akimotoite CPO within the Tonga slab (Shiraishi et al., 2008). Nucleation of akimotoite on $(100)_{cEn}$ twin planes in clinoenstatite,

and topotaxial replacement indicates that it is possible for akimotoite to inherit a CPO from enstatite in a previously deformed rock. Further, the presence of topotaxial wadsleyite and stishovite within our sample suggests that these phases may also inherit CPO from enstatite. Therefore, we caution against interpreting future observations of seismic anisotropy as evidence for localized strain of akimotoite and other high-pressure phases within the lowermost MTZ, as CPO of high-pressure phases may have been inherited from previously deformed clinoenstatite within subduction zones in the upper mantle.

4.4.3 Effects of Polysynthetic Twinning on Transformation

The reaction sequence of OEN (*Pbca*) to HCEN2 ($P2_1/c$) to HCEN (*C2/c*) that occurrs during the compression and heating of our experimental samples is simlar to what is expected within the interior of cold subducting lithosphere. At low slab temperatures, kinetic factors inhibit diffusion-controlled reactions of enstatite to garnet (Nishi et al., 2008; van Mierlo et al., 2013; King et al., 2015) and enstatite to wadsleyite or ringwoodite plus stishovite (Chapter 3; Hogrefe et al., 1994). This will allow the $(Mg,Fe)SiO_3$ component of the slab to remain metastable as a pyroxene phase until pressures are sufficiently high for polymorphic transitions to akimotoite, majorite, or bridgmanite (Chapter 3).

Metatsable enstatite within the cold interior of slabs is likely to be completely transformed to HCEN (*C2/c*) phase prior to the nucelation and growth of akimotoite, majorite, or bridgmanite. During isothermal experiments at 400°C using Fe and Al bearing OEN (*Pbca*), OEN remained stable until it was transformed to HCEN2 ($P2_1/c$) at

13 GPa (Zhang et al., 2014). While the stability of the HCEN2 ($P2_1/c$) phase relative to HCEN ($C2/c$) remains unclear at higher pressures and temperatures, $P2_1/c$ to $C2/c$ reaction is a displacive first-order phase transition (Ulmer and Stalder 2001) that requires much less activation energy than a reconstructive transformation of $P2_1/c$ to high-pressure polymorphs akimotoite, majorite, or bridgmanite.

Planar defects such as twin boundaries are metastable structures that provide surfaces for enhanced heterogeneous nucleation of high-pressure phases. For example, heterogeneous nucleation of ringwoodite has been reported on stacking faults in olivine during transformation experiments using large olivine crystals (Kerschhofer et al., 1996, 1998 Dupas-Bruzek et al., 1998) and within shocked meteorites (Chen et al., 2004; Greshake et al., 2013). In this study, experimental samples transformed at 21 GPa contain coherently intergrown akimotoite lamellae along $(100)_{cEn}$ (Figure 4.3) and amorphous bridgmanite lamellae sub-parallel to $(100)_{cEn}$ (Figure 4.5). The presence of positive and negative twins of topotaxial akimotoite within our samples confirms that the enstatite was twinned during the ortho- to clinopyroxene transition prior to the transformation to high-pressure phases. Enstatite within the mantle should also contain abundant twin boundaries, which would greatly increase the density of nucleation sites for high-pressure phases such as akimotoite.

Experiments transformed at 21 GPa and 1300°C to 1400°C contained high-pressure crystallites that only occurred along well-developed akimotoite and amorphous bridgmanite lamellae. This suggests that the crystallites form via secondary transformation mechanisms that first requres the presence of bridgmanite or akmotoite lamellae. Moreover, bridgmanite lamellae within the interior of samples transformed at

21 GPa and 1300°C to 1400°C can occur either (1) in isolation from other high-pressure phases, or they can be associated with larger growth features containing more abundant akimotoite and majorite (Figure 4.5). While the nucleation mechanism for the amorphous bridgmanite lamellae is unclear, it is apparent that they provide nucleation sites for akimotoite and possibly majorite.

Given the large (>1 mm) grain sizes within the mantle and the ubiquity and abundance of polysynthetic twins within recovered pyroxene cores in our experimental samples, nucleation and growth of high-pressure phases along twin boundaries is likely to be common within mantle enstatite. Intracrystalline nucleation of akimotoite or other phases on HCEN twin boundaries would therefore increase the overall rate of transformation by reducing growth distances. It is likely that the rate of enstatite transformation in subducting slabs will be largely controlled by the density of twin boundaries in clinoenstatite.

4.4.4 Implications for the Cause of Deep-Focus Earthquakes

Intracrystalline growth of high-pressure phases has been shown to occur within enstatite (Chapter 3) and olivine (Kerschhofer et al., 1996, 1998). Additionally, crystals formed via intracrystalline coherent mechanisms can provide new grain boundary sites for incoherent nucleation and interface controlled growth (Sharp and Rubie, 1995; Kerschhofer et al., 1998). Within this study, secondary growth of high-pressure phases occurred along the interface between clinoenstatite and both coherent akimotoite lamellae and amorphous bridgmanite lamellae. In the mantle, increased enstatite reactivity caused by heterogeneous nucleation on twin boundaries would reduce the depth to which

metastable enstatite could survive within the cold interior of a subducting slab, thus limiting the depth to which transformational faulting of enstatite could contribute to nucleation of deep-focus earthquakes.

The $(100)_{cEn}$ twin boundaries could also impact on the grain size and rheology of subducting slabs, as both (1) mechanically weak planar defects in enstatite and (2) nucleation sites for intracrystalline transformation and grain size reduction. In experiments on polysynthetically twinned crystals, shear deformation is focused along planes parallel with twin boundaries when a wide range of maximum compressive stress orientations are applied to the sample (Fujiwara et al., 1990). Additionally, our experiments contain two separate reactions that produce lamellae along the $(100)_{cEn}$ twin plane. The reduction of grain size due to secondary growth of high-pressure phases along these lamellae could substantially weaken pyroxene-rich portions of the mantle. Therefore, shear instability along the $(100)_{cEn}$ twin boundaries coupled with reduced grain sizes from intracrystalline transformation will produce regions of pre-existing weakness within enstatite rich rock in subducting slabs. It is possible that these zones of weakness could trigger cascading failure of shear thermal instabilities, which is one of several hypothesis for the initiation of deep focus earthquakes (Karato et al., 2001; Chen and Wan 2015).

4.5 Conclusions

Solid-state transformation experiments using single crystals of natural San Carlos enstatite show that the ortho- to clinopyroxene transition produces abundant polysynthetic twinning along $(100)_{cEn}$. The pressure and temperature conditions of the

ortho- to clinopyroxene transition vary depending on composition and pressure-temperature path, and further studies are required to refine the stability fields for the various polymorphs of Mg-rich pyroxene. Regardless of the conditions under which the ortho- to clinopyroxene transformation occurs, the reaction is expected to produce polysynthetic twinning along $(100)_{cEn}$ for all $(Mg,Fe)SiO_3$ clinopyroxene within the upper mantle. Our experiments show that $(100)_{cEn}$ twin boundaries can serve as nucleation sites for both coherent and incoherent growth of multiple high-pressure phases. The abundance and ubiquity of polysynthetic twining within our samples suggests that nucleation sites along the $(100)_{cEn}$ twin boundaries will outnumber potential grain boundary nucleation sites, and therefore, intracrystalline growth of high-pressure phases may be the dominant mechanism for transformation for Mg-rich pyroxenes within the mantle. If active within the mantle, intracrystalline transformation mechanisms would enhance transformation rates of metastable enstatite within subducting lithosphere, thereby decreasing the likelihood that transformational faulting of metastable enstatite causes the deepest earthquakes.

The presence of the $(100)_{cEn}$ twins is also likely to have a significant impact on the physical properties of enstatite-rich portions of the mantle. Our experimental sample transformed at 21 GPa and 1400°C contained topotaxial growth of akimotoite, wadsleyite and stishovite parallel to the $(100)_{cEn}$ twins. It has been shown that minerals within the mantle can inherit CPOs from lower pressure phases (Dobson et al., 2013). Topotaxial replacement, either by heterogeneous nucleation on twin boundaries, as observed here, or by a shear mechanism, as proposed by *Tomioka* (2007), would transfer CPO in enstatite bearing subducting slabs into akimotoite and potentially other high-pressure phases.

Observed seismic anisotropy within subducting slabs in the lowermost transition zone may, therefore, represent inherited CPOs rather than CPOs formed by deformation in the MTZ.

Polysynthetic twinning in clinoenstatite can influence the rheology of subducting slabs in two ways. First, the twin boundaries themselves are planar defects that may weaken the crystal and allow for shear instability along $(100)_{cEn}$ (Fujiwara et al., 1990). Second, our experiments show that lamellae of akimotoite or bridgmanite can grow parallel to $(100)_{cEn}$, and these lamellae can serve as nucleation sites for secondary growth of nano-scale high-pressure phases. If active within the MTZ, these transformation mechanisms will result in a grain size reduction that is concentrated along $(100)_{cEn}$ planes. When considered together, shear instability from polysynthetic twin boundaries and grain size reduction along $(100)_{cEn}$ may provide weak zones necessary to result in a cascading shear failure similar to what has been proposed for the cause of deep focus earthquakes (Karato et al., 2001; Chen and Wen 2015). Further experimental studies are necessary to determine whether polysynthetic twins and grain size reduction along $(100)_{cEn}$ can provide enough instability to produce seismogenic failure in pyroxene-rich portions of subducting slabs.

CHAPTER 5

CONCLUDING REMARKS AND FUTURE DIRECTIONS

5.1 Summary

Much of what we know about the Earth is described by models that are continually refined through observational, experimental, and theoretical research. The strength of these models is dependent upon an accurate understanding of the underlying small-scale phenomena that drive the modeled larger-scale process. Within this dissertation, I show that observational seismology and experimental mineral physics can provide important constraints on models for a range of large-scale geophysical phenomena within the crust and mantle.

5.2 Conclusions from Observational Seismology

Within Chapter 2, I use the temporal and spatial distribution of small-magnitude earthquakes ($M < 2.0$) to constrain models of the tectonophysics of the diffuse North American-Pacific plate boundary. For the period of study, diffuse seismic activity occurred across the Great Basin (GB) with the exception of a rigid crustal block between longitudes -114.5°E and -113° E. Widespread seismicity and active deformation within the interior of the GB (Chamoli et al., 2014; Hammond et al., 2014) dispels the model of the GB behaving as a rigid microplate and suggests that Basin and Range extension continues within the interior of the GB.

An improved detection threshold for small-magnitude earthquakes within the GB reveals a complex range of fault behavior within the region. Earthquake clusters, swarms and mainshock-aftershock sequences occur throughout the GB, which suggests that

swarms and clusters are a general mechanism of diffuse deformation throughout the interior of the GB. In several cases, earthquake clusters appear to be temporally associated despite being located along separate range-bounding faults. By using a variety of geophysical data to eliminate potential causes for these earthquake sequences, I suggest that pore fluid pressure variation due to external geophysical phenomena (i.e., local transient deformation events or subsurface fluid migration) is the most likely cause of temporally correlated increases in seismicity rates within the study region.

To further constrain potential triggers for localized temporal seismicity rate increases, future studies should perform detailed analysis of geodetic data (InSAR, geodesy, borehole strainmeters, etc.) within the area of a specific swarm or cluster. Additionally, swarms and clusters in this study area provide an excellent opportunity to use a waveform matching algorithm to search for evidence of non-volcanic tremor or low-frequency earthquakes (e.g., Peng and Gomberg 2010) to determine whether this type of fault behavior is limited to plate boundaries or if it occurs elsewhere within intracontinental environments. Further, the EarthScope USArray Transportable Array provides an unprecedented opportunity to more accurately characterize the distribution of small-magnitude earthquakes across the continental U.S. Using the methodology described in Chapter 2 would greatly increase the earthquake detection threshold for many regions with low seismicity and historically poor seismometer coverage. Future studies should examine whether earthquake swarms and clusters are present within these regions of historically lower seismicity rates. If present in all seismotectonic environments, closer examination of the mechanisms that cause small-magnitude

earthquake swarms could improve process models of fault slip (e.g. Peng and Gomberg 2010)

5.3 Conclusions from Experimental Mineral Physics

Within Chapters 3 and 4, I use results from a series of high pressure and temperature experiments to constrain models for the dynamics and rheology of subducting oceanic lithosphere within the mantle transition zone (MTZ). For these experiments, I explore the mechanisms and kinetics of high-pressure phase transitions within subducting slabs using single crystals of natural Al- and Fe-bearing enstatite $(Mg,Fe)SiO_3$.

In Chapter 3, I report that natural enstatite crystals are far more reactive than end-member $MgSiO_3$ (Hogrefe et al., 1994). This suggests that metastable natural enstatite within the cold interior of subducting slabs will transform to high-pressure phases at much shallower depths than previously thought. Therefore, transformational faulting caused by rapid transformation of enstatite to akimotoite is unlikely be responsible for the deepest recorded earthquakes. Furthermore, increased reactivity of natural enstatite will have significant effects on thermo-kinetic and geodynamic models of the behavior of subducting slabs within the MTZ. Future kinetic studies are necessary to empirically determine transformation rates for the enstatite-akimotoite reactions that are expected to dominate within the interior of subducting slabs. Kinetic rate data can then be applied to future thermo-kinetic models of slab behavior to better constrain the impact of metastable enstatite on models of buoyancy and the stagnation of slabs at the base of mantle transition zone.

Within Chapter 4, I examine the role of polysynthetic twinning on the nucleation and growth of high-pressure phases within natural enstatite. The abundance and ubiquity of polysynthetic twining within experimentally transformed clinoenstatite indicates that nucleation sites along the $(100)_{cEn}$ twin boundaries may be the preferred mechanism for the transformation of coarsely crystalline enstatite to within cold subducting slabs. This intracrystalline transformation mechanism should also be included in future models examining the transformation kinetics and dynamic behavior of subducting slabs. Topotaxial growth of akimotoite, wadsleyite, and stishovite along polysynthetic twin boundaries provides a mechanism for high-pressure phases to inherit a crystallographic preferred orientation (CPO) from enstatite in previously deformed mantle lithosphere. Thus, seismic anisotropy within subducting slabs in the lowermost transition zone may be inherited from a preexisting pyroxene CPO and not reflect the current state of stress within the slab. Finally, planar defects and grain size reduction along $(100)_{cEn}$, may provide the pre-existing weak zones necessary to result in a cascading shear failure similar to what has been proposed for the cause of deep focus earthquakes (Karato et al., 2001; Chen and Wen, 2015). Further experimental studies are necessary to determine whether polysynthetic twins and grain size reduction along $(100)_{cEn}$ can provide enough instability to produce seismogenic failure in pyroxene-rich mantle lithologies.

The mechanisms and kinetics of high-pressure phase transformations in enstatite are not well understood. The results presented within this dissertation represent a preliminary study of transformation mechanisms and resulting microtextures within these first six (6) experiments performed on singe crystals of natural enstatite. Additional experimentation is necessary to obtain empirically-determined transformation rates for

both intracrystalline and grain boundary nucleation mechanisms in enstatite. While numerous transformation rate studies have been performed on olivine, none have been performed on enstatite to date. Future studies should measure intracrystalline and grain boundary growth rates as a function of time (e.g. Rubie and Ross, 1994; Deidrich et al., 2009; Du Frane, et al., 2012) to obtain mechanism specific growth rates that can be applied to future thermo-kinetic models of subduction.

REFERENCES

Agrusta, R., J. van Hunen, and S. Goes (2014). The effect of metastable pyroxene on the slab dynamics, *Geophys. Res. Lett.* **41,** 8800–8808, doi: 10.1002/2014GL062159.

Akaogi, M., and S. I. Akimoto (1977). Pyroxene-garnet solid-solution equilibria in the systems $Mg_4Si_4O_{12}$-$Mg_3Al_2Si_3O_{12}$ and $Fe_4Si_4O_{12}$-$Fe_3Al_2Si_3O_{12}$ at high pressures and temperatures, *Phys. Earth Planet. In.* **15,** no. 1, 90-106, doi: 10.1016/0031-9201(77)90013-9.

Angel, R. J., A. Chopelas, and N. L. Ross (1992). Stability of high-density clinoenstatite at upper-mantle pressures, *Nature* **358,** 322-324.

Arabasz, W. J., S. J. Nava, M. K. McCarter, K. L. Pankow, J. C. Pechmann. J. Ake and A. McGarr (2005). Coal-mining seismicity and ground-shaking hazard: a case study in the Trail Mountain area, Emery County, Utah, *Bull. Seismol. Soc. Am.* **95**, no. 1, 18-30.

Astiz, L., J. A. Eakins, V. G. Martynov, T. A. Cox, J. Tytell, J. C. Reyes, R. L. Newman, G. H. Karasu, T. Mulder, M. White, G. A. Davis, R. W. Busby, K. Hafner, J. C. Meyer, and F. L. Vernon (2014). The Array Network Facility Seismic Bulletin: Products and an unbiased view of United States Seismicity, *Seismol. Res. Lett.* **85,** no. 3, 576-593, doi: 10.1785/0220130141.

Bell, J. W., S. J. Caskey, A. R. Ramelli, and L. Guerrieri (2004). Pattern and rates of faulting in the central Nevada seismic belt, and paleoseismic evidence for prior beltlike behavior, *Bull. Seismo. Soc. Am.* **94,** 1229-1254.

Bennett, R. A., B. P. Wernicke, N. A. Niemi, A. M. Friedrich, and J. L. Davis (2003). Contemporary strain a Basin and Range province from GPS data, *Tectonics* **22,** no. 2, 1008, doi: 10.1029/2001TC001355.

Billings, S. D., M. S. Sambridge, and L. N. Kennett (1994). Errors in hypocenter location: Picking, model, and magnitude dependence, *Bull. Seismo. Soc. Am.* **84,** 1978-1990.

Bina, C. R., S. Stein, F. C. Marton, E. M. Van Ark (2001). Implications of slab mineralogy for subduction dynamics, *Phys. Earth Planet. In.* **127,** 51–66.

Bell, D. R., G.R. Rossman (1992). Water in earth's mantle: the role of nominally anhydrous minerals, *Science* **255,** no. 5050, 1391-1397.

Boese, C. M., K. M. Jacobs, E. G. C. Smith, T. A. Stern, and J. Townend (2014). Background and delayed-triggered swarms in the central Southern Alps, South Island, New Zealand, *Geochem. Geophys. Geosyst.* **15,** 945–964, doi: 10.1002/ 2013GC005171.

Bolfan-Casanova, N., H. Keppler, and D. C. Rubie (2003). Water partitioning at 660 km depth and evidence for very low water solubility in magnesium silicate perovskite, *Geophys. Res. Lett.* **30,** no. 17, 1905, doi: 10.1029/2003GL017182.

Bon, R. L. and S. Wakefield (2008). Large Mines in Utah 2008, *Utah Geological Survey Open File Report 515*.

Bratt, S., and T. C. Bache (1988). Locating events with a sparse network of regional arrays, *Bull. Seismo. Soc. Am.* **78,** 780-798.

Bratt, S., and W. Nagy (1991). The LocSAT program, *Science Applications International Corporation, San Diego*.

Braunmiller, J., J. L. Nábělek, and A. M. Tréhu (2014). A seasonally modulated earthquake swarm near Maupin, Oregon, *Geophys. J. Int.* **197,** 1736-1743 doi: 10.1093/gji/ggu081.

Brodsky, E. E., and L. J. Lajoie (2013). Anthropogenic Seismicity Rates and Operational Parameters at the Salton Sea Geothermal Field, *Science* **341,** 543-546, doi: 10.1126/ science.1239213.

Buseck, P. R., and S. Iijima (1975). High resolution microscopy of enstatite. II: Geological application, *Am. Mineral.* **60,** 771-784.

Carter, M. J., M. E. Zimmerman, and C. Teyssier (2015). The fate of fluid inclusions during high-temperature experimental deformation of olivine aggregates, *J. Geophys. Res. Solid Earth* **120,** doi:10.1002/2014JB011782.

Catchings, R. D., and W. D. Mooney (1991). Basin and Range crustal and upper mantle structure, northwest to central Nevada, *J. Geophys. Res.* **96,** 6247-6267.

Chamoli, A., A. R. Lowry, and T. N. Jeppson (2014). Implications of transient deformation in the northern Basin and Range, western United States, *J. Geophys. Res. Solid Earth*, **119,** 4393–4413, doi: 10.1002/2013JB010605.

Chen M., A,El Goresy and P. Gillet (2004). Ringwoodite lamellae in olivine: Clues to olivine-ringwoodite phase transition mechanisms in shocked meteorites and subducting slabs. *Proc. Natl. Acad. Sci. U.S.* **101,** 15033–15037.

Chen, Y., and L. Wen (2015). Global large deep-focus earthquakes: Source process and cascading failure of shear instability as a unified physical mechanism *Earth Planet. Sci. Lett.* **423,** 134-144, doi:10.1016/j.epsl.2015.04.031.

Collier, J. D., G. R. Helffrich, and B. J. Wood (2001). Seismic discontinuities and subduction zones, *Phys. Earth Planet. In.* **127,** 35-49.

Connolly, J. A. D. (2009). The geodynamic equation of state: What and how, *Geochem. Geophys. Geosyst.* **10,** Q10014, doi: 10.1029/2009GC002540.

Davis, D. A. and R. H. Hess (2009). Nevada active mines and energy producers, *Nevada Bureau of Mines and Geology Special Publications Educational Series, E-49.*

Davis, J. L., B. P. Wernicke, S. Bisnath, N. A. Niemi, and P. Elósegui (2006). Subcontinental-scale crustal velocity changes along the Pacific-North American plate boundary, *Nature* **441,** 1131–1134, doi: 10.1038/nature04781.

Diedrich, T., T. G. Sharp, K. Leinenweber, and J. R. Holloway (2009). The effect of small amounts of H_2O on olivine to ringwoodite transformation growth rates and implications for subduction of metastable olivine, *Chem. Geol.* **262,** no. 1-2, 87-99.

Dobson, D. P, N. Miyajima, F. Nestola, M. Alvaro, N. Casati, C. Liebske, I. G. Wood, and A. M. Walker (2013). Strong inheritance of texture between perovskite and post-perovskite in the D" layer, *Nat. Geosci.* **6,** 575-578, doi: 10.1038/NGEO1844.

Doser, D. I., and R. B. Smith (1989). An assessment of source parameters of earthquakes in the cordillera of the western United States, *Bull. Seism. Soc. Am.* **79,** 1383-1409.

Du Frane, W. L., T. G. Sharp, J. L. Mosenfelder, and K. Leinenweber (2012). Ringwoodite growth rates from olivine with ~75 ppmw H_2O: Metastable olivine must be nearly anhydrous to exist in the mantle transition zone, *Phys. Earth Planet. In.* **219,** 1-10, doi:10.1016/j.pepi.2013.04.001.

Dupas-Bruzek, C., T. G. Sharp, D. C. Rubie, and W. B. Durham (1998). Mechanisms of transformation and deformation in $Mg_{1.8}Fe_{0.2}SiO_4$ olivine and wadsleyite under non-hydrostatic stress, *Phys. Earth Planet. In.* **108,** 33–48.

Eaton, D. A., and J. L. Rubinstein (2015). Preface to the focus section on injection-induced seismicity, *Seismol. Res. Lett.* **84,** 1058-1059, doi: 10.1785/0220150093.

Ellsworth, W. L. (2013). Injection-induced earthquakes, *Science*, **341,** doi: 10.1126/ science.1225942.

Fischer, T., J. Horáleka, P. Hrubcováa, V. Vavryčuka, K. Bräuerc, and H. Kämpf (2014). Intra-continental earthquake swarms in West-Bohemia and Vogtland: A review, *Tectonophys,* **611,** 1-27, doi: 10.1016/j.tecto.2013.11.00.

Frey, F. A. and M. Prinz (1978). Ultramafic inclusions from San-Carlos, Arizona: petrologic and geochemical data bearing on their petrogenesis, *Earth Planet. Sci. Lett.* **38,** no. 1, 129-176.

Friedrich, A. M., B. P. Wernicke, N. A. Niemi, R. A. Bennett, and J. L. Davis (2003). Comparison of geodetic and geologic data from the Wasatch region, Utah, and implications for the spectral character of Earth deformation at periods of 10 to 10 million years, *J. Geophys. Res.* **108,** doi: 10.1029/2001JB000682.

Frohlich, C. (2006). Deep Earthquakes. *Cambridge University Press*, *New York*, 573 pp.

Frohlich, C., C. Hayward, B. Stump, and E. Potter (2011). The Dallas–Fort Worth earthquake sequence: October 2008 through May 2009, *Bull. Seism. Soc. Am.* **101,** 327-340.

Fujiwara, T., A. Nakamura, M. Hosomi, S. R. Nishitani, Y. Shirai, and M. Yamaguchi, (1990). Deformation of polysynthetically twinned crystals of TiAl with a nearly stoichiometric composition, *Phil. Mag. A* **61,** no. 4, 591-606, doi: 10.1080/ 01418619008231937

Gilbert, H., and A. Sheehan (2004). Images of crustal variations in the intermountain west, *J. Geophys. Res.* **109,** B03306.

Gilbert, H., (2012). Crustal structure and signatures of recent tectonism as influenced by ancient terranes in the western United States, *Geosphere* **8,** 141–157.

Grant, K., J. Ingrin, J. P. Lorand, and P. Dumas (2007). Water partitioning between mantle minerals from peridotite xenoliths, *Contrib. Mineral Petrol.* **154,** 15-34.

Green, H. W. and P. C. Burnley (1989). A new self-organizing mechanism for deep-focus earthquakes, *Nature* **341,** no. 6244, 733-737.

Greshake, A., J. Fritz, U. Böttger, and D. Goran (2013). Shear-induced ringwoodite formation in the Martian shergottite Dar al Gani 670, *Earth Planet. Sci. Lett.* **375,** 383-394, doi: 10.1016/j.epsl.2013.06.002

Guglielmi, Y., F. Cappa, J.-P. Avouac, P. Henry, and D. Elsworth (2015). Seismicity triggered by fluid injection-induced aseismic slip, *Science* **348,** doi: 10.1126/ science.aab0476.

Gulia, L., (2010). Detection of quarry and mine blast contamination in European regional catalogues, *Nat. Hazards* **53,** 229-249, doi: 10.1007/s11069-009-9426-8.

Gutenberg, B., and C. F. Richter (1944). Frequency of earthquakes in California, *Bull. Seismol. Soc. Am.* **34,** 184-188.

Hainzl, S., T. Kraft, J. Wassermann, H. Igel, and E. Schmedes (2006). Evidence for rainfall-triggered earthquake activity, *Geophys. Res. Lett.* **33,** L19303, doi: 10.1029/2006GL027642.

Hammond, W. C., G. Blewitt, and C. Kreemer (2014). Steady contemporary deformation of the central Basin and Range province, western United States, *J. Geophys. Res. Solid Earth* **119,** 5235-5253, doi: 10.1002/2014JB011145.

Hammond, W. C., and W. Thatcher (2004). Contemporary tectonic deformation of the Basin and Range province, western United States: 10 years of observation with the Global Positioning System, *J. Geophys. Res.*, **109,** B08403 doi: 10.1029/2003JB002746.

Hanks, T. C., and H. Kanamori, (1979). A moment-magnitude scale, *J. Geophys. Res.* **84,** 2348–2350.

Hattori, T., T. Tsuchiya, T. Nagai, and T. Yamanaka (2001). Sequential high-pressure transformations of $FeGeO_3$ high-P clinopyroxene (*C*2/*c*) at temperatures up to 365°C, *Phys. Chem. Miner.* **28,** 377-387.

Hogrefe, A., D. C. Rubie, T. G. Sharp, and F. Seifert (1994). Metastability of enstatite in deep subducting lithosphere, *Nature* **372,** no. 6504, 351-353.

Holbrook, W. S. (1990). The crustal structure of the northwestern Basin and Range province, Nevada, from wide-angle seismic data, *J. Geophys. Res.* **95,** 21843-21869.

Holbrook, W. S., R. D. Catchings, and C. M. Jarchow (1991).Origin of deep crustal reflections - Implications of coincident seismic refraction and reflection data in Nevada, *Geology* **19,** 175-179.

Holland, A. A. (2012). Earthquakes triggered by hydraulic fracturing in south-central Oklahoma, *Bull. Seismol. Soc. Am.* **103,** no. 3, 1784–1792, doi: 10.1785/0120120109.

Holtkamp, S. G., and M. R. Brudzinski, (2011). Earthquake swarms in circum-Pacific subduction zones, *Earth Planet. Sci. Lett.* **305,** 215–225.

Holtkamp, S. G., M. E. Pritchard, and R. B. Lohman (2011). Earthquake swarms in South America, *Geophys. J. Int.* **187,** 128-146, doi: 10.1111/j.1365-246X.2011.05137.x.

Hugh-Jones, D., T. Sharp, R. Angel, and A. Woodland (1996). The transition of orthoferrosilite to high-pressure *C*2/*c* clinoferrosilite at ambient temperature, *Eur. J. Mineral.* **8,** 1337-1345.

Houston, H. (2007). Deep earthquakes, in H. Kanamori and G. Schubert eds., *Treatise on Seismology,* p. 321-350.

Hill D. P. (1977). A model for earthquake swarms, *J. Geophys. Res.* **82,** 1347-1352.

Irifune, T., and A. E. Ringwood (1987). Phase transformations in a harzburgite composition to 26 GPa: implications for dynamical behavior of the subducting slab, *Earth Planet. Sci. Lett.* **86,** 365-376.

Irifune, T., and A. E. Ringwood (1993). Phase transformations in subducted oceanic crust and buoyancy relationships at depths of 600–800 km in the mantle, *Earth Planet. Sci. Lett.* **117,** 101-110.

Kanamori, H. (1983). Magnitude scale and quantification of earthquakes, *Tectonophys.* **93,** 185–199.

Karato, S., M. R. Riedel, and D. A. Yuen (2001). Rheological structure and deformation of subducted slabs in the mantle transition zone: implications for mantle circulation 180 and deep earthquakes, *Phys. Earth Planet. In.* **127,** no. 1-4, 83-108.

Kennett, B. L. N., and E. R. Engdahl (1991). Traveltimes for global earthquake location and phase identification, *Geophys. J. Int.* **105,** 429–465.

Kerschhofer, L., T. G. Sharp and D. C. Rubie (1996). Intracrystalline transformation of olivine to wadsleyite and ringwoodite under subduction zone conditions, *Science* **274,** 5284, 79-81.

Kerschhofer, L., C. Dupas, M. Liu, T. G. Sharp, W. B. Durham and D. C. Rubie (1998). Polymorphic transformations between olivine, wadsleyite and ringwoodite: mechanisms of intracrystalline nucleation and the role of elastic strain, *Mineral. Mag.* **62,** no. 5, 617-638.

Kerschhofer, L., D. C. Rubie, T. G. Sharp, J. D. C. McConnell, and C. Dupas-Bruzek (2000). Kinetics of intracrystalline olivine-ringwoodite transformation, *Phys. Earth Planet. In.* **121,** no. 1-2, 59-76.

King, S. D., D. J. Frost, and D. C. Rubie (2015). Why cold slabs stagnate in the transition zone, *Geology* **43,** no. 3, 231-234, doi: 10.1130/G36320.1.

Kirby, S. H., S. Stein, E. A. Okal and D. C. Rubie (1996). Metastable mantle phase transformations and deep earthquakes in subducting oceanic lithosphere, *Rev. Geophys.* **34,** no. 2, 261-306.

Kreemer, C., G., Blewitt and W. C. Hammond (2010). Evidence for an active shear zone in southern Nevada linking the Wasatch fault to the Eastern California shear zone, *Geology* **38,** 475-478.

Kubo, T., E. Ohtani, T. Kato, T. Shinmei, and K. Fujino (1998). Effects of water on the alpha-beta transformation kinetics in San Carlos Olivine, *Science* **281,** no. 5373, 85-87.

Kurz, J. H., T. Jahr, and G. Jentzsch (2004). Earthquake swarm examples and a look at the generation mechanism of the Vogtland/Western Bohemia earthquake swarms, *Phys. Earth Planet. In.* **142,** 75–88.

Lay, T., H. Kanamori, C. J. Ammon, K. D., Koper, A. R. Hutko, L. Ye, H. Yue, and T. M. Rushing (2012). Depth-varying rupture properties of subduction zone megathrust faults, *J. Geophys. Res.* **117,** B04311, doi: 10.1029/2011JB009133.

Lay, T., and T. C. Wallace (1995). Modern Global Seismology, *Academic Press*, New York, 521 pp.

Leinenweber, K. D., J. A. Tyburczy, T. G. Sharp, E. Soignard, T. Diedrich, W. B. Petuskey, Y. Wang, and J. L. Mosenfelder (2012). Cell assemblies for reproducible multi-anvil experiments (the COMPRESS assemblies), *Am. Mineral.* **97,** 353-368.

Lengliné, O. J. E. Elkhoury, G. Daniel, J. Schmittbuhl, R. Toussaint, J.-P. Ampuero, and M. Bouchon (2012). Interplay of seismic and aseismic deformations during earthquake swarms: An experimental approach, *Earth Planet. Sci. Lett.* **331-332,** 215-223, doi: 10.1016/j.epsl.2012.03.022.

Li, Z.-X. A., C.-T. A. Lee, A. H. Peslier, A. Lenardic, and S. J. Mackwell (2008). Water contents in mantle xenoliths from the Colorado Plateau and vicinity: Implications for the mantle rheology and hydration-induced thinning of continental lithosphere, *J. Geophys. Res.* **113,** B09210, doi: 10.1029/2007JB005540.

Lin, C.-C. (2004). Pressure-induced polymorphism in enstatite ($MgSiO_3$) at room temperature: clinoenstatite and orthoenstatite. *J. Phys. Chem. Solid.* **65,** 913-921.

Liu, M., L. Kerschhofer, J. L. Mosenfelder, and D.C. Rubie (1998). The effect of strain energy on growth rates during the olivine-spinel transformation and implications for olivine metastability in subducting slabs, *J. Geophys. Res. Solid Earth*, **103,** no. B10, 23897-23909.

Lockridge, J. S., M. J. Fouch, and J R. Arrowsmith (2012). Seismicity within Arizona during the Deployment of the EarthScope USArray Transportable Array, *Bull. Seismol. Soc. Am.* **102,** no. 4, 1850–1863, doi: 10.1785/0120110297.

Lohman, R. B., and J. J. McGuire (2007). Earthquake swarms driven by aseismic creep in the Salton Trough, California, *J. Geophys. Res.* **112,** B04405, doi: 10.1029/ 2006JB004596.

Lowry, A. R., and M. Pérez-Gussinyé (2011). The role of crustal quartz in controlling Cordilleran deformation, *Nature* **471,** no. 7338, 353-357.

Llenos, A. L., J. J., McGuire, Y. Ogata (2009). Modeling seismic swarms triggered by aseismic transients, *Earth Planet. Sci. Lett.* **281,** 59-69.

Ma, S., and D. W. Eaton (2009). Anatomy of a small earthquake swarm in southern Ontario, Canada, *Seismol. Res. Lett.* **80,** 214-223.

McGuire, J. J., M. S. Boettcher and T. H. Jordan (2005). Foreshock sequences and short-term earthquake predictability on East Pacific Rise transform faults, *Nature* **434,** 457–461.

Megis, T., and J. Wassermann (2014). Microseismicity observed at a non-pressure-stimulated geothermal power plant, *Geothermics* **52,** 36-49.

Mignan, A., and J. Woessner (2012). Estimating the magnitude of completeness for earthquake catalogs, *Community Online Resource for Statistical Seismicity Analysis*, doi: 10.5078/corssa-00180805.

Milke, R., R. Dohmen, H. W. Becker, and R. Wirth (2007). Growth kinetics of enstatite reaction rims studied on nano-scale, Part I: Methodology, microscopic observations and the role of water, *Contrib. Mineral. Petrol.* **154,** 519–533, doi: 10.1007/s00410-007-0207-7.

Morris, S. J. S. (2002). Coupling of interface kinetics and transformation-induced strain during pressure-induced solid-solid phase changes, *J. Mech. Phys. Solid.* **50,** 1363-1395.

Mosenfelder, J. L., J. A. D. Connolly, D.C. Rubie, and M. Liu (2000). Strength of $(Mg,Fe)_2SiO_4$ wadsleyite determined by relaxation of transformation stress, *Phys. Earth Planet. Inter.* **120,** no. 1-2, 63-78.

Mosenfelder, J. L., F. C. Marton, C. R. Ross, L. Kerschhofer, and D. C. Rubie (2001). Experimental constraints on the depth of olivine metastability in subducting lithosphere, *Phys. Earth Planet. In.* **127,** no. 1-4, 165-180.

Nadeau, R. M., W. Foxall and T. V. McEvilly (1995). Clustering and periodic recurrence of microearthquakes on the San Andreas fault at Parkfield, California, *Science*, **267,** 503-507.

Nitkiewicz, A. M. and S. M. Sterner (1988). An improved bond air mill for the preparation of spherical single-crystals, *Am. Mineral.* **73,** no. 5-6, 662-666.

Nishi, M., T. Kato, T. Kubo, and T. Kikegawa (2008). Survival of pyropic garnet in subducting plates, *Phys. Earth Planet. In.* **170,** no. 3, 274–280, doi: 10.1016/ j.pepi.2008.03.013.

Nishi, M., T. Kubo, H. Ohfuji, T. Kato, Y. Nishihara, and T. Irifune (2013). Slow Si-Al interdiffusion in garnet and stagnation of subducting slabs, *Earth Planet. Sci. Lett.* **361,** 44-49, doi: 10.1016/j.epsl.2012.11.022.

Ozawa, S., H. Suito, and M. Tobita, (2007). Occurrence of quasi-periodic slow-slip off the east coast of the Boso peninsula, Central Japan, *Earth Planets Space*, **59,** 1241–1245.

Parotidis, M., E. Rothert, and S. Shapiro (2003). Pore-pressure diffusion: A possible triggering mechanism for the earthquake swarms 2000 in Vogtland/NW-Bohemia, central Europe, *Geophys. Res. Lett.* **30,** 2075, doi: 10.1029/2003GL018110.

Pavlis, G. L., F. Vernon, D. Harvey, and D. Quinlan (2004). The generalized earthquake-location (GENLOC) package: An earthquake-location library, *Comput. Geosci.* **30,** 1079–1091.

Peng, Z., and J. Gomberg (2010). In integrated perspective of the continuum between earthquakes and slow-slip phenomena, *Nature Geosci.* **3,** 599-607, doi: 10.1038/ ngeo940.

Perrillat, J. P., I. Daniel, N. Bolfan-Casanova, M. Chollet, G. Morard, and M. Mezouar (2013). Mechanism and kinetics of the α–β transition in San Carlos olivine $Mg_{1.8}Fe_{0.2}SiO_4$, *J. Geophys. Res. Solid Earth* **118,** 110–119, doi: 10.1002/ jgrb.50061.

Persh, S. E. and H. Houston (2004). Strongly depth-dependent aftershock production in deep earthquakes, *Bull. Seismol. Soc. Am.* **94,** no. 5, 1808–1816.

Porter, R. C., M. J. Fouch, and N. C. Schmerr (2014). Dynamic lithosphere within the Great Basin, *Geochem. Geophys. Geosyst.* **15,** doi: 10.1002/2013GC005151.

Reynard, B., J. D. Bass, and J. Brenizer (2010). High-temperature elastic softening of orthopyroxene and seismic properties of the lithospheric upper mantle, *Geophy. J. Int.* **181,** 557–566.

Richter, C. F. (1958). Elementary Seismology, First Ed., *W.H. Freeman and Company, San Francisco, U.S.A.*, 768 pp.

Ringwood, A. E. (1982). Phase transformations and differentiation in subducted lithosphere: implications for mantle dynamics, basalt petrogenesis, and crustal evolution, *J. Geol.* **90,** no. 6, 611-643.

Ringwood, A. E. (1991). Phase transformations and their bearing on the constitution and dynamics of the mantle, *Geochim. Cosmochim. Acta* **55,** 2083-2110.

Rubie, D. C. and C. R. Ross (1994). Kinetics of the olivine-spinel transformation in subducting lithosphere: experimental constraints and implications for deep slab processes. *Phys. Earth Planet. In.* **86,** no. 1-3, 223-241.

Rubinstein, J. L., and A. Babaie Mahani (2015). Myths and facts on wastewater injection, hydraulic fracturing, enhanced oil recovery, and induced seismicity, *Seismol. Res. Lett.* **86,** no. 4, doi: 10.1785/0120150067.

Segall, P., E. K. Desmarais, D. Shelly, A. Miklius, and P. Cervelli (2006). Earthquakes triggered by silent slip events on Kīlauea volcano, Hawaii, *Nature* **442,** 71–74.

Segall, P. (2010). Earthquake and volcano deformation, *Princeton University Press*, 432 p.

Sharp, T. G. and D. C. Rubie (1995). Catalysis of the olivine to spinel transformation by high clinoenstatite. *Science* **269,** 1095-1098.

Shelly, D. R., D. P. Hill, F. Massin, J. Farrell, R. B., Smith, and T. Taira (2013). A fluid-driven earthquake swarm on the margin of the Yellowstone caldera, *J. Geophys. Res. Solid Earth* **118,** 4872–4886, doi: 10.1002/jgrb.50362.

Shinmei, T., N. Tomioka, K. Fujino, K. Kuroda, and T. Irifune (1999). In situ X-ray diffraction study of enstatite up to 12 GPa and 1473 K and equations of state, *Am. Mineral.* **84,** 1588-1594.

Shiraishi, R. E. Ohtani, K. Kanagawa, A. Shimojuku, and D. Zhao (2008). Crystallographic preferred orientation of akimotoite and seismic anisotropy of Tonga slab, *Nature* **455**, 657-660, doi: 10.1038/nature07301.

Simpson, D. W., W. S. Leith, and C. H. Scholz (1986). Two types of reservoir-induced seismicity, *Bull. Seismol. Soc. Am.* **78,** 2025–2040.

Smith, K. D., D. von Seggern, G. Blewitt, L. Preston, J. G. Anderson, B. P. Wernicke, and J. L. Davis (2004). Evidence for deep magma injection beneath Lake Tahoe, Nevada-California, *Science* **305,** 1277, doi: 10.1126/science.1101304.

Spencer, J. E., and S. J. Reynolds (1989). Middle Tertiary tectonics of Arizona and adjacent areas, in J. P. Jenney, and S. J. Reynolds, eds., *Geologic evolution of Arizona: Arizona Geological Society Digest 17*, p. 539-573.

Špičák, A. (2000). Earthquake swarms and accompanying phenomena in intraplate regions: a review, *Stud. Geophys. Geod.* **44,** 89-106.

Stixrude, L., and C. Lithgow-Bertelloni, (2011). Thermodynamics of mantle minerals - II. Phase equilibria, *Geophys. J. Int.* **184,** 1180- 1213.

Stump, B. W., M. A. H. Hedlin, D. C. Pearson, and V. Hsu (2002). Characterization of mining explosions at regional distances: Implications with the International Monitoring System, *Rev. Geophys.* **40,** 4, doi: 10.1029/1998RG000048.

Sung, C. M. and R. G. Burns (1976). Kinetics of olivine→spinel transition: implications to deep-focus earthquake genesis, *Earth Planet. Sci. Lett.* **32,** no. 2, 165-170.

Tetzlaff, M. and H. Schmeling (2009). Time-dependent interaction between subduction dynamics and phase transition kinetics, *Geophys. J. Int.* **178,** no. 2, 826-844.

Tomioka, N. and K. Fujino (1997). Natural $(Mg,Fe)SiO_3$ –ilmenite and –perovskite in the Tenham meteorite, *Science* **277,** 1084-1086. doi: 10.1126/science.277.5329.1084.

Tomioka, N., and K. Fujino (1999). Akimotoite, $(Mg,Fe)SiO_3$, a new silicate mineral of the ilmenite group in the Tenham chondrite, *Am. Mineral.* **84,** 267-271.

Tomioka, N. (2007). A model for the shear mechanism in the enstatite-akimotoite phase transition, *J. Miner. Petrol. Sci.* **102,** 226-234, doi: 10.2465/jmps.060227.

Ulmer, P. and R. Stadler (2001). The $Mg(Fe)SiO_3$ orthoenstatite-clinoenstatite transitions at high pressures and temperatures determined by Raman-spectroscopy on quenched samples, *Am. Mineral.* **86,** 1267–1274.

Utsu, T., Y. Ogata, and R. Matsu'ura (1995). The centenary of the Omori formula for a decay law of aftershock activity, *J. Phys. Earth* **43,** 1–33.

van Mierlo, W. L., F. Langenhorst, D. J. Frost, and D. C. Rubie (2013). Stagnation of subducting slabs in the transition zone due to slow diffusion in majoritic garnet, *Nature Geosci.* **6,** 400-403, doi: 10.1038/ngeo1772.

Vidale, J. E., and P. M. Shearer (2006). A survey of 71 earthquake bursts across southern California: Exploring the role of pore fluid pressure fluctuations and aseismic slip as drivers, *J. Geophys. Res.* **111,** no. B05312. doi: 10.1029/2005JB004034.

Watson, D. F., and G. M. Philip (1985). A refinement of inverse distance weighted interpolation, *Geo. Process.* **2,** 315–327.

Wernicke, B., J. L. Davis, N. A. Niemi, P. Luffi, and S. Bisnath (2008). Active megadetachment beneath the western United States, *J. Geophys. Res*. **113,** doi: 10.1029/2007JB005375.

Wernicke, B. and J. L. Davis (2010). Detecting large-scale intracontinental slow-slip event (SSEs) using geodograms, *Seismo. Res. Lett.* **81,** no. 5, 694-698, doi: 10.1785/gssrl.81.5.694

Wiemer S., and M. Baer (2000). Mapping and removing quarry blast events from seismicity catalogs, *Bull. Seism. Soc. Am.* **90,** no. 2, 525-530

Wiemer S., and M. Wyss (2000). Minimum magnitude of completeness in earthquake catalogs: examples from Alaska, the Western United States, and Japan, *Bull. Seismol. Soc. Am.* **90,** no. 4, 859–869.

Yamashita T. (1999). Pore creation due to fault slip in a fluid-permeated fault zone and its effect on seismicity: generation mechanism of earthquake swarm, *Pure Appl. Geophys.* **155,** 625-647.

Zhang, J. S., P. Dera, and J. D. Bass (2012). A new high-pressure phase transition in natural Fe-bearing orthoenstatite, *Am. Mineral.* **97,** 1070–1074, doi: 10.2138/am.2012.4072.

Zhang, J. S., B. Reynard, G. Montagnac, R. C. Wang, and J. D. Bass (2013). Pressure-induced *Pbca-P*2_1*/c* phase transition of natural orthoenstatite: Compositional effect and its geophysical implications. *Am. Mineral.* **98,** 986–992. doi: 10.2138/am.2013.4345

Zhang, J. S., B. Reynard, G. Montagnac, and J. D. Bass (2014). Pressure-induced *Pbca-P*2_1*/c* phase transition of natural orthoenstatite: The effect of high temperature and its geophysical implications, *Phys. Earth Planet. In.* **228,** 150-159, doi: 10.1016/j.pepi.2013.09.008.

Zhou, C., S. Gréaux, N. Nishiyama, T. Irifune, and Y. Higo, (2014). Sound velocities measurement on $MgSiO_3$ akimotoite at high pressures and high temperatures with simultaneous in situ X-ray diffraction and ultrasonic study, *Phys. Earth Planet. In.* **228,** 97-105, doi: 10.1016/j.pepi.2013.06.005.

Zuniga, F. R., and M. Wyss (1995). Inadvertent changes in magnitude reported in earthquake catalogs: Their evaluation through *b*-value estimates, *Bull. Seismol. Soc. Am.* **85,** 1858-1866.

APPENDIX A

GREAT BASIN SEISMICITY FROM 2004 TO 2013

[Consult attached .kmz file using Google Earth for PC, Mac, or Linux. Data tables in .csv format can be viewed using any text editor on any operating system.]

The file referenced below is a comprehensive earthquake catalog for the Great Basin from 2004 to 2013. This catalog contains (1) the small-magnitude event catalog generated as part of this dissertation (ASU), (2) events from the catalog generated by the EarthScope Array Network Facility (ANF), and (3) events from the Advanced National Seismic System (ANSS) catalog. See Section 2.2 of this dissertation for additional information on citations and data sources for ANF and ANSS data. The full catalog can be downloaded as Google Earth KMZ file or as a comma-delimited .csv file from:

http://activetectonics.asu.edu/e-quakes/GB_EQs_2004-2012.kmz

http://activetectonics.asu.edu/e-quakes/GB_EQs_2004-2012.csv

Description of column headings for earthquake data are as follows: yr=year; mo=month; day=day; hr=hour; min=minute; sec=second; lat=latitude; lon=longitude; dep=depth; mag=magnitude; magt=magnitude type; auth=source catalog; nsta=number of stations used for earthquake location; gap=maximum azimuthial gap between seismic stations used to locate event.

APPENDIX B

GREAT BASIN EARTHQUAKE SWARMS FROM 2004 TO 2013

This appendix contains additional data for the 10 earthquake swarms within the Great Basin from 2004 to 2013. Within some clusters in Table 2.6, earthquakes occurred within the same 4 km radius spatial area as earthquake swarms but were not temporally associated with the peak period of seismicity that defined an earthquake swarm. Therefore, data within Table 2.6 displays event counts and peak activity for all spatially-associated events located within a 4 km radius (i.e. earthquake clusters), and some of these event clusters include periods of swarm-like seismic activity.

Table A1 includes only event data for spatially and temporally associated earthquake swarm events.

Figure A1 contains plots of (left) swarm events vs. time since the onset of swarm-like seismic activity and (right) cumulative seismic moment release vs. time for each swarm. Letters in the top left of each plot correlate each plot with a specific earthquake swarm, as identified in the "Swarm ID" column of Table A1.

Table B1. Earthquake Swarms within the Great Basin from 2004 to 2013

Swarm ID	Latitude	Longitude	Region	Total Events	Start Date (mm/dd/yyyy)	Duration (Days)	Max Event Magnitude	Cumulative Moment (dyne-cm)	Swarm Magnitude
A	40.56	-111.27	ISB	6	12/30/2011	283	0.9	1.31×10^{18}	1.4
B	39.32	-111.55	ISB	12	04/26/2004	1	2.3	8.96×10^{19}	2.6
C	40.80	-111.78	ISB	24	11/12/2004	1	2.2	8.48×10^{19}	2.6
D	39.93	-111.82	ISB	66	06/01/2011	69	3.3	2.02×10^{21}	3.5
E	39.97	-111.89	ISB	23	08/05/2008	26	2.1	4.30×10^{19}	2.4
F	39.04	-114.85	Central GB	21	05/10/2007	93	2.5	1.17×10^{20}	2.7
G	40.53	-115.99	Central GB	19	07/12/2007	6	2.3	1.67×10^{20}	2.8
K	40.52	-116.26	Central GB	19	08/06/2007	1	2.1	3.32×10^{19}	2.3
I	38.65	-118.40	CNSB/WLFS	13	01/01/2012	1	1.3	2.70×10^{18}	1.6
J	41.21	-118.49	Northwest GB	10	12/26/2006	33	2.1	3.73×10^{19}	2.4

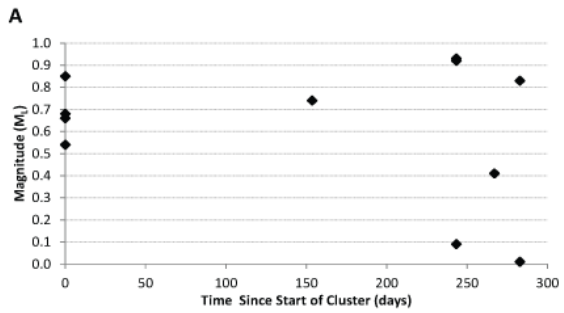
A
Magnitude (M_L)
Time Since Start of Cluster (days)

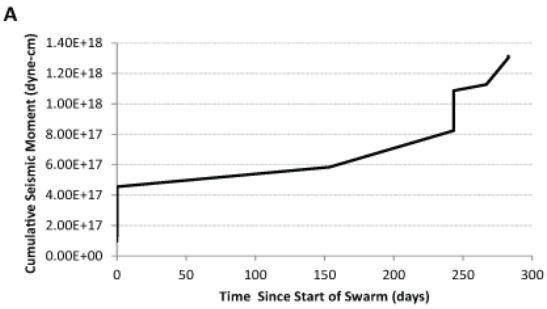
A
Cumulative Seismic Moment (dyne-cm)
Time Since Start of Swarm (days)

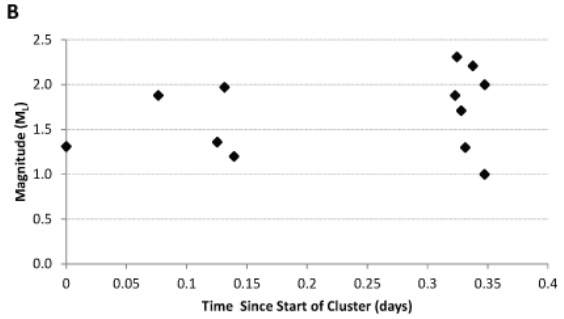
B
Magnitude (M_L)
Time Since Start of Cluster (days)

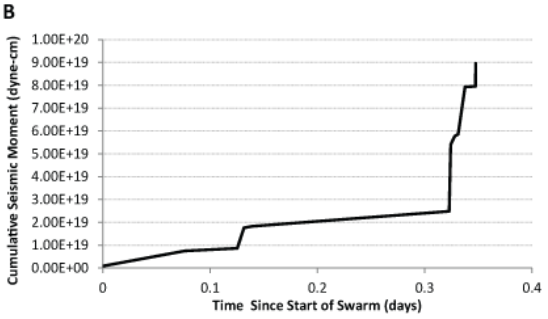
B
Cumulative Seismic Moment (dyne-cm)
Time Since Start of Swarm (days)

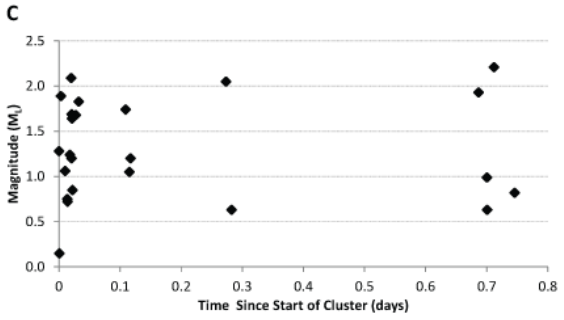
C
Magnitude (M_L)
Time Since Start of Cluster (days)

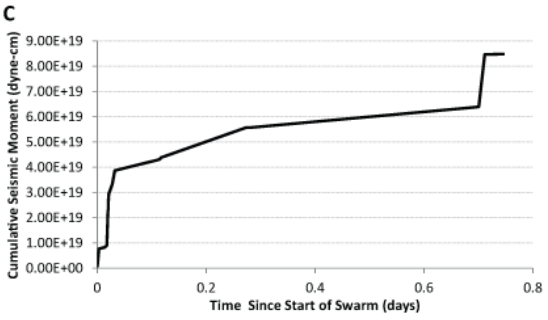
C
Cumulative Seismic Moment (dyne-cm)
Time Since Start of Swarm (days)

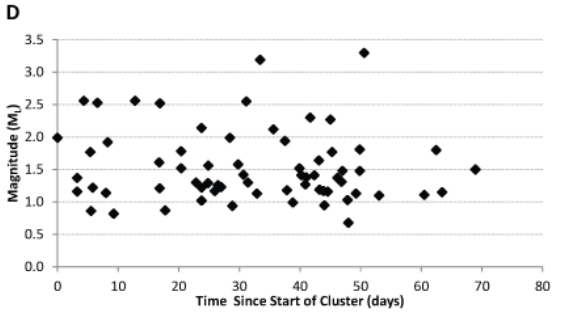
D
Magnitude (M_L)
Time Since Start of Cluster (days)

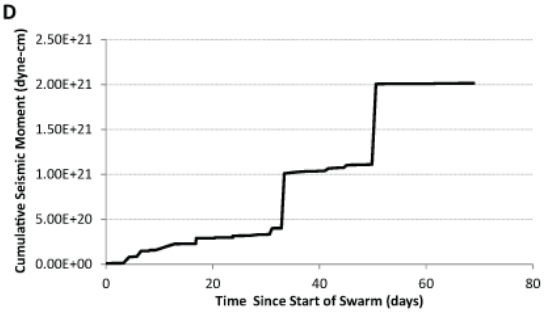
D
Cumulative Seismic Moment (dyne-cm)
Time Since Start of Swarm (days)

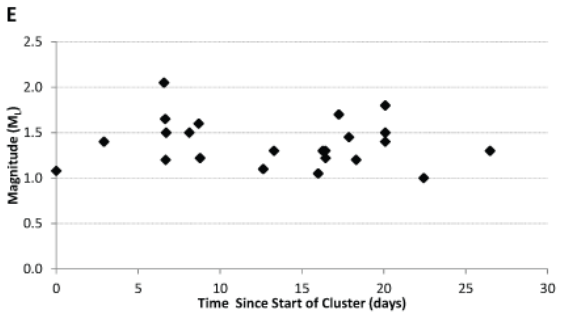
E
Magnitude (M_L)
Time Since Start of Cluster (days)

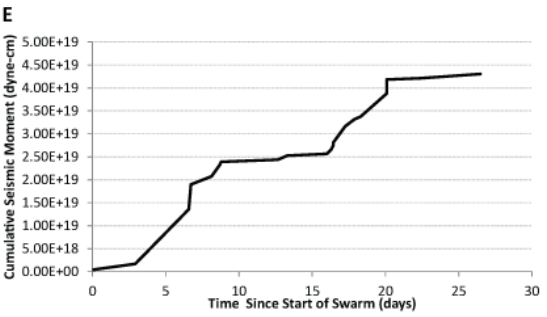
E
Cumulative Seismic Moment (dyne-cm)
Time Since Start of Swarm (days)

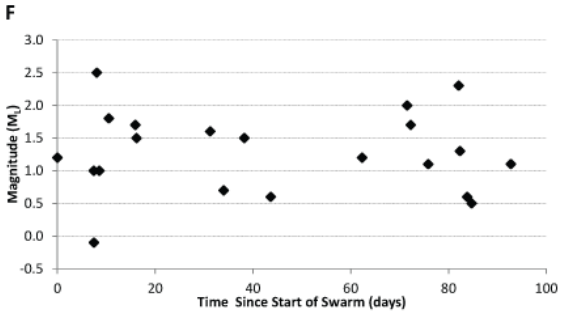
F
Magnitude (M_L)
Time Since Start of Swarm (days)

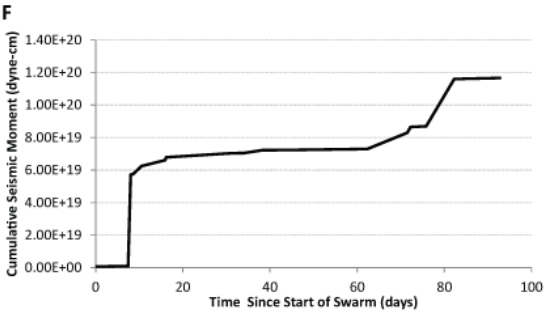
F
Cumulative Seismic Moment (dyne-cm)
Time Since Start of Swarm (days)

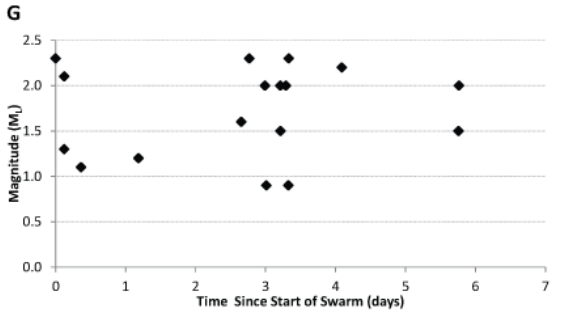
G
Magnitude (M_L)
Time Since Start of Swarm (days)

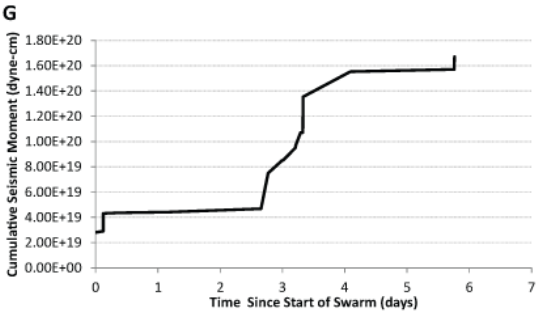
G
Cumulative Seismic Moment (dyne-cm)
Time Since Start of Swarm (days)

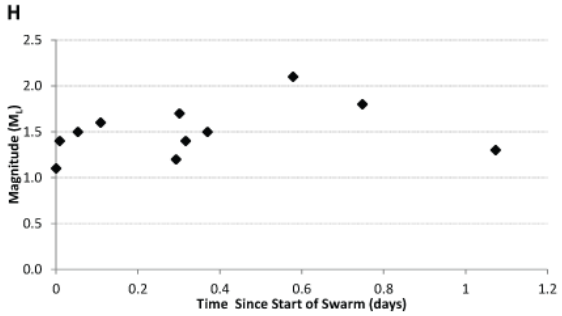
H
Magnitude (M_L)
Time Since Start of Swarm (days)

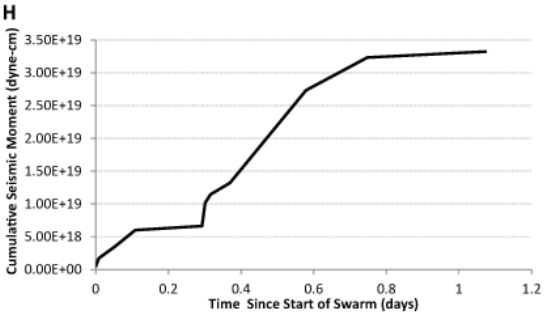
H
Cumulative Seismic Moment (dyne-cm)
Time Since Start of Swarm (days)

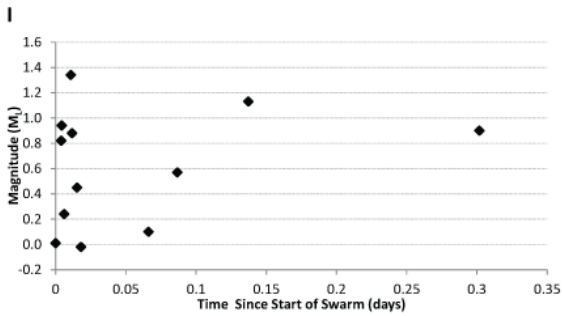
I
Magnitude (M_L)
Time Since Start of Swarm (days)

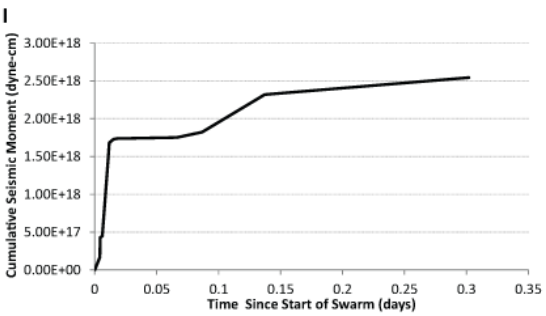
I
Cumulative Seismic Moment (dyne-cm)
Time Since Start of Swarm (days)

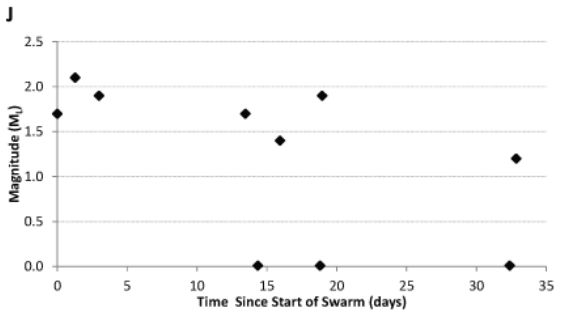
J
Magnitude (M_L)
Time Since Start of Swarm (days)

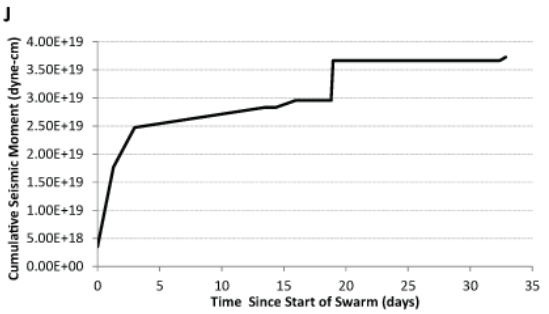
J
Cumulative Seismic Moment (dyne-cm)
Time Since Start of Swarm (days)